TECHNICAL UNIVERSITY OF CATALONIA (UPC)
DEPARTMENT OF GEOTECHNICAL ENGINEERING AND GEO-SCIENCES
(ETCG)

Processes affecting the efficiency of limestone, aragonite and dolostone in passive treatments for AMD

Thesis presented by

Francesco G. Offeddu

Work conducted in the Institute of Environmental Assessment and Water Research (IDAEA-CSIC) under the supervision of

Supervisors:

Dr. Jordi Cama Dr. Josep M. Soler

Institute of Environmental Assessment and Water Research
(IDAEA-CSIC)

Barcelona, October 2015

This thesis has been funded by projects CTM2007-66724-C02-01/ TECNO and CGL2010-20984-C02-01 from the Spanish Government. FGO was supported by a JAE-Predoc grant under the Program “Junta para la Ampliación de Estudios”.

Is Knowledge knowable?

If not, how do we know?

W. Allen

Abstract

Waters resulting from mine activity, known as acid mine drainage (AMD), usually contain elevated concentrations of sulfate, iron and other contaminant metals, which can persist in the environment during several centuries after mine closure. The main purposes of AMD treatments are retention of metals (precipitation of the contaminant metals) and neutralization of acidity. One of the possible and most common passive treatment systems is the anoxic limestone drainage (ALD), or systems derived from it (e.g., reducing and alkalinity producing systems), characterized by low maintenance and cost. The efficiency of the ALD systems is however limited because secondary mineral precipitation causes the passivation (armoring) of the limestone grains and clogging of the pores, reducing limestone reactivity and acid neutralization. In addition, the presence of aqueous sulfate leads to gypsum precipitation, which essentially contributes to passivation and affects greatly the efficiency of the treatment systems.

This PhD study aims at enhancing our knowledge on the loss of reactivity of calcite, aragonite and dolomite due to grain coating or clogging of porosity. To this end, three types of experiments were conducted: (1) column, (2) batch and (3) in-situ AFM experiments.

(1) Experiments using columns packed with calcite, aragonite or dolomite grains (size 1-2 mm) were carried out to study the behavior of passive treatment systems designed to remediate contaminated water from AMD. Synthetic acidic solutions (mainly pH 2, H_2SO_4) were injected in the columns: sulfate with Fe(III) or sulfate with aluminum. Fluid flow was constant during the experiments with Darcy velocities ranging from $6x10^{-4}$ to $1x10^{-3}$ L m^{-2} s^{-1}. The columns worked efficiently removing aqueous iron and aluminum as long as calcite dissolved and buffered the solution pH (increasing pH and promoting the precipitation of Fe(III)-oxyhydroxides or Al-oxyhydroxides). However, Ca released from dissolving calcite, along with the sulfate in solution, led to formation of gypsum coatings on the calcite grain surfaces which eventually prevented calcite dissolution. This passivation process limited the efficiency of the columns. Larger input sulfate concentrations or higher pH led to shorter

passivation times. Characterization of the pore structure and composition by X-ray microtomography (mCT) and X-ray microdiffraction (mXRD) showed the precipitation of gypsum coatings on the calcite grains and secondary oxyhydroxides between the grains. This secondary mineral precipitation favored the formation of preferential flow paths, isolating regions of non-reacted limestone. An improved experimental design (mixing limestone grains and glass beads) minimized the formation of these preferential flow paths. Experimental results have been modeled with the CrunchFlow reactive transport code. Fitting of the results required a decrease in the reactive surface area of calcite, which is consistent with the passivation process.

(2) Batch experiments at 25 °C, atmospheric pressure and pH 2 (H_2SO_4 solution equilibrated with respect to $CaSO_4 \cdot 2H_2O$) were performed to study the coupled reactions of dissolution of Ca and Mg carbonate minerals (calcite, aragonite and dolomite) and precipitation of gypsum. Three types of solid sample (powder (100-300 μm), grains (1-2 mm) and fragments (1.5 x 1.2 x 0.5 cm)) acted as carbonate substrates on which gypsum grew. Throughout the experiments three stages were distinguished: gypsum precipitation induction time, dissolution of the carbonate substrate, together with gypsum precipitation, and achievement of equilibrium with respect to the dissolving carbonate mineral.

The induction time was similar during dissolution of calcite and aragonite since both minerals dissolved at the same rate. During dissolution of the carbonate minerals the pH raised from 2 to about 7, decreasing both the carbonate mineral dissolution rate and the gypsum precipitation rate to become zero as equilibrium with respect to $CaCO_3$ was approached. The gypsum precipitation rates were similar when calcite and aragonite dissolved, regardless the morphology of substrate.

(3) In-situ atomic force microscopy (AFM) experiments were performed to study the overall process of dissolution of common carbonate minerals (calcite and dolomite) and precipitation of gypsum in Na_2SO_4 and $CaSO_4$ solutions with pH values ranging from 2 to 6 at room temperature (23 ± 1 °C). The dissolution of the carbonate minerals took place at the (104) cleavage surfaces in sulfate-rich

solutions undersaturated with respect to gypsum, by the formation of characteristic rhombohedral-shaped etch pits.

Rounding of the etch pit corners was observed as solutions approached close-to-equilibrium conditions with respect to calcite. The calculated dissolution rates of calcite at pH 4.8 and 5.6 agreed with the values reported in the literature. When using solutions previously equilibrated with respect to gypsum, gypsum precipitation coupled with calcite dissolution showed short gypsum nucleation induction times. The gypsum precipitate quickly coated the calcite surface, forming arrow-like forms parallel to the crystallographic orientations of the calcite etch pits. Gypsum precipitation coupled with dolomite dissolution was slower than that of calcite, indicating the dissolution rate to be the rate-controlling step. The resulting gypsum coating partially covered the dolomite surface during the experimental duration of a few hours.

Resum

Les aigües que procedeixen de l'activitat minera, conegudes com aigües àcides de mina (en anglès acid mine drainage, AMD) contenen normalment altes concentracions de sulfat, ferro i altres metalls contaminants associats. Aquests contaminants poden perdurar en el medi ambient fins a segles després del cessament de l'activitat minera. Els principals objectius dels tractaments AMD són la retenció de metalls (precipitació dels metalls contaminants) i la neutralització de l'acidesa de les aigües. Un dels possibles sistemes de tractament passiu, i dels més utilitzats, és el drenatge anòxic amb calcària (en anglès, anoxic limestone drainage, ALD), o sistemes derivats (per exemple, la reducció i els sistemes de producció d'alcalinitat), que es caracteritzen pel poc manteniment requerit i el baix cost. No obstant, l'eficiència dels sistemes d'ALD està limitada per la precipitació de minerals secundaris que causa la passivació (recobriment) dels grans de calcària i l'obstrucció dels porus entre ells, reduint així la reactivitat de la calcària i, per tant, el poder tampó. La presència de sulfat aquós indueix la precipitació de guix, que contribueix en gran mesura a la passivació de la calcària i afecta l'eficiència dels sistemes de tractament.

Aquesta Tesi té com a objectiu principal millorar els nostres coneixements sobre el funcionament de minerals carbonats utilitzats en ALD i la pèrdua de la reactivitat de la calcita, aragonita i dolomita a causa del recobriment dels grans o l'obstrucció dels porus entre grans. Amb aquesta finalitat, es s'han dut a terme tres tipus d'experiments: (1) experiments de columna, (2) de tipus batch i (3) experiments in situ amb AFM.

(1) Els experiments de columnes emplenades amb grans de calcita, aragonita o dolomita (de diàmetre 1-2 mm) es van realitzar per estudiar el comportament dels sistemes de tractament passiu emprats en el drenatge àcid de mines (AMD). Es van injectar solucions àcides sintètiques (principalment a pH2, H_2SO_4) rica en ferro (Fe (III)) o alumini. Durant els experiments, el flux de la solució d'entrada es va mantenir constant a la velocitat de Darcy de $6x10^{-4}$ a $1x10^{-3}$ L m^{-2} s^{-1}. Les columnes han eliminat eficientment el ferro i l'alumini aquosos mentre que la dissolució dels carbonats ha tamponat el pH de la solució (augment del pH i inducció de la precipitació d'oxihidróxids de Fe (III) - o d'Al). No obstant,

el Ca alliberat en solució pels minerals carbonats, juntament amb el sulfat aquós, va induir la precipitació de guix, que és la principal causa de recobriment (passivació) a les superfícies dels grans. Aquest recobriment ha impedit conseqüentment la dissolució de calcita limitant l'eficiència de les columnes. Concentracions més altes del sulfat d'entrada i pH més àcids van originar temps de passivació més ràpids. La caracterització de l'estructura dels porus i de la composició química dels sòlids mitjanament la per micro-tomografia de raigs X (MCT) i micro-difracció de raigs X (mXRD), va mostrar que el recobriment dels grans de carbonats és degut a la precipitació de guix i que els oxihidróxids secundaris tendeixen a precipitar entre els grans. La precipitació de minerals secundaris va afavorir la formació de fluxos preferents, aïllant regions on no es produeixen reaccions entre la solució circulant i els grans. L'efecte de la formació del flux preferent s'ha reduït utilitzant un disseny diferent a les columnes (barrejant els grans de carbonats amb esferes de vidre inerts). Els resultats experimentals s'han modelitzat amb el codi de transport reactiu CrunchFlow. Per tal que les dades experimentals i les del model coincidissin s'ha ajustat al valor de l'àrea reactiva de la calcita en el model, consistentment amb el procés de passivació en els experiments.

(2) Es van dur a terme experiments de tipus batch a 25 ° C, pressió atmosfèrica i pH 2 (solució de H_2SO_4 equilibrada respecte al $CaSO_4 \cdot 2H_2O$) per estudiar les reaccions de dissolució de la calcita i aragonita acoblades a la precipitació de guix. Es van utilitzar tres tipus de mostra sòlida (pols (100-300 μm), grans (1-2 mm) i fragments (1.5 x 1.2 x 0.5 cm)) que van actuar com a substrats de mineral carbonat en què va créixer el guix. Al llarg dels experiments s'han distingit tres fases: temps d'inducció de la precipitació del guix, dissolució del substrat de mineral carbonat, juntament amb la precipitació de guix, i l'assoliment de l'equilibri de la solució respecte el mineral carbonat.

El temps d'inducció va ser similar durant la dissolució de calcita i aragonita, ja que tots dos minerals dissolen amb la mateixa velocitat de dissolució. Durant la dissolució de minerals carbonats, el pH va pujar de 2 a aproximadament 7, alentint tant la velocitat de dissolució dels carbonats com la taxa de precipitació de guix per arribar a zero un cop assolit l'equilibri amb $CaCO_3$ (calcita o aragonita) va ser aconseguit. La velocitat de precipitació del guix va ser similar

independentment del substrat (calcita o aragonita), tot i la morfologia del mateix substrat.

3) Es van realitzar experiments in-situ amb el microscopi de força atòmica (AFM) per estudiar el procés global de la dissolució de calcita i dolomita i la precipitació de guix en solucions Na_2SO_4 i $CaSO_4$ amb valors de pH entre 2 i 6 i temperatura ambient (23 ± 1 ° C). La dissolució dels minerals carbonats va tenir lloc a les superfícies de clivatge (104) usant solucions riques en sulfat i subsaturades respecte al guix. Es va observar la formació de forats de dissolució (etch pits) amb les típiques formes romboèdriques.

També s'observa l'arrodoniment de les vores dels etch pits quan les solucions s'acostaven a a les vores l'equilibri respecte de la calcita. Les velocitats de dissolució de la calcita calculades a pH 4.8 i 5.6 va coincidir amb els valors de la literatura. En solucions prèviament equilibrades amb el guix, la precipitació de guix acoblada a la dissolució de calcita s'aconseguí amb temps d'inducció més curts. El guix precipitat va recobrir ràpidament la superfície de la calcita, amb morfologia de fletxa i eixos paral·lels a les orientacions cristal·logràfiques dels etch pits de la calcita. La precipitació de guix, juntament amb la dissolució de dolomita, va ser més lenta que la de calcita, la qual cosa indica que la velocitat de dissolució va ser el procés que controla la velocitat. El revestiment de guix ha cobert parcialment la superfície de la calcita durant l'experiment.

Resumen

Las aguas que proceden de la actividad minera, conocidas como aguas ácidas de mina (*acid mine drainage*, AMD) normalmente contienen altas concentraciones de sulfato, hierro y otros metales contaminantes asociados. Estos contaminantes pueden perdurar en el medio ambiente durante décadas o incluso durante siglos después de la interrupción de la actividad minera. Los principales objetivos de los tratamientos de AMD son la retención de metales (precipitación de los metales contaminantes) y la neutralización de la acidez de las aguas. Uno de los sistemas de tratamiento pasivo más comunes, es el drenaje anóxico a través de caliza (en inglés *anoxic limestone drainage,* ALD), o sistemas derivados, tales como la reducción o los sistemas de producción de alcalinidad. El ALD está caracterizado por necesitar escaso mantenimiento y por su bajo coste. Sin embargo, la eficiencia de los sistemas ALD está limitada por la precipitación de minerales secundarios que causa el recubrimiento de los granos de caliza (*pasivación)* y la colmatación de los poros, reduciendo así la reactividad de la caliza y por lo tanto su poder tampón. Además la precipitación de yeso se ve inducida por la presencia de sulfato acuoso, la cual contribuye en gran medida a la pasivación de la caliza y afecta directamente a la eficiencia de los sistemas de tratamiento.

Esta Tesis tiene como objetivo principal mejorar el conocimiento sobre los procesos que afectan a los minerales carbonatos durante el ALD y sobre la pérdida de la reactividad de la calcita, el aragonito y la dolomita debido al recubrimiento de sus granos o a la colmatación de sus poros. Con este fin, se llevaron a cabo tres tipos de experimentos: (1) experimentos de columns, (2) de tipo batch y (3) experimentos *in situ* con AFM.

(1) Los experimentos de columnas compuestas por granos de calcita, aragonita o dolomita (de diametro 1-2 mm) se han usado para estudiar el comportamiento de los sistemas de tratamiento pasivo que se emplean en el drenaje ácido de minas (AMD). Se inyectaron soluciones ácidas sintéticas (H_2SO_4, principalmente a pH 2) ricas en hierro Fe (III) o aluminio. Durante los experimentos, el flujo se mantuvo constante, con valores comprendidos entre $6x10^{-4}$ y $1x10^{-3}$ L m^{-2} s^{-1}. Se ha observado que las columnas han retenido eficientemente el hierro y el

aluminio acuosos mientras que la disolución de los carbonatos ha tamponado el pH de la solución (aumento del pH e inducción de la precipitación de oxihidróxidos de Fe (III) - o de Al). Sin embargo el Ca liberado por los carbonatos en la solución, junto con el sulfato acuoso, han inducido la precipitación de yeso, causa principal del recubrimiento (pasivación) de la superficie de los granos. En consecuencia dicho recubrimiento ha impedido la disolución de calcita, limitando así, la eficiencia de las columnas. También se ha observado que concentraciones mayores del sulfato de entrada y pH más ácidos, produjeron en general tiempos de pasivación más rápidos. La caracterización de la estructura de los poros y de la composición química, realizada mediante micro-tomografía de rayos X (mCT) y micro-difracción de rayos X (mXRD), mostró que el recubrimiento de los granos de carbonatos se debe a la precipitación de yeso y que los oxihidróxidos secundarios tienden a precipitar entre los granos. La precipitación de minerales secundarios favoreció la formación de flujos preferenciales, aislando así regiones donde no se producen reacciones entre la solución circulante y los granos. Además, el efecto de la formación de flujo preferencial se ha visto reducido mediante un diseño de las columnas diferente (mezclado de los granos de carbonatos con esferas de vidrio inertes). Los resultados experimentales se han modelado con el código de transporte reactivo CrunchFlow. Para que los datos experimentales y los del modelo pudieran coincidir se ha ajustado el valor de del área reactiva de la calcita en el modelo, de forma consistente con el proceso de pasivación en los experimentos.

(2) Los experimentos de tipo batch a 25 °C, a presión atmosférica y a pH 2 (solución de H_2SO_4 equilibrada respecto al $CaSO_4 \cdot 2H_2O$) se realizaron para estudiar las reacciones de disolución de calcita y de aragonita, con precipitación de yeso sobre la superficie de los carbonatos (sustratos). Se ensayaron tres tipos de muestra sólida de sustrato, (polvo, 100-300 μm, granos, 1-2 mm, y fragmentos, 1.5 x 1.2 x 0.5 cm). A lo largo de los experimentos se han distinguido tres fases. La primera fase es el tiempo necesario para el inicio de la precipitación del yeso (tiempo de inducción). La segunda hace referencia al hecho ya nombrado de la disolución de sustratos (carbonatos) y la simultánea

precipitación de yeso. En la tercera y última fase, el equilibrio entre la solución y el mineral carbonatado es alcanzado.

Se ha observado que el tiempo de inducción fue similar durante la disolución de calcita y aragonito, ya que ambos minerales se han disuelto con la misma velocidad de disolución. Durante la disolución de carbonatos, el pH subió de 2 a 7 aproximadamente, ralentizando así, la cinética de disolución de los carbonatos y la velocidad de precipitación de yeso hasta llegar a cero una vez alcanzado el equilibrio con $CaCO_3$. Además resultó que independientemente del sustrato de calcita o aragonito, la velocidad de precipitación del yeso fue similar, a pesar de la morfología del sustrato.

(3) Se realizaron experimentos *in situ* con microscopio de fuerza atómica (AFM) para estudiar el proceso global acoplado de la disolución de calcita o dolomita con la precipitación de yeso. Los experimentos se han realizado con soluciones de Na_2SO_4 y $CaSO_4$ y pH entre 2 y 6 a temperatura ambiente (23 ± 1 ° C). La disolución de los minerales carbonatados tuvo lugar en las superficies de exfoliación (104) usando soluciones ricas en sulfato y sub-saturadas con respecto al yeso. También se han observado distintas formas de disolución (denominadas *etch pits*), con estructura típica romboédrica.

Además se observó el redondeo de los bordes de los etch pits conforme se aproximaban a condiciones cercanas al equilibrio con respecto a la calcita. Las velocidades de disolución de la calcita a pH 4.8 y 5.6 resultaron de acuerdo con los valores de la literatura. También la precipitación de yeso acoplada con la disolución de calcita mostró un tiempo de inducción de nucleación más corto, en el caso de uso de soluciones previamente equilibradas con yeso. El yeso precipitado recubrió rápidamente la superficie de la calcita, con morfología de flecha y ejes paralelos a las orientaciones cristalográficas de los etch pits de la calcita. En cambio, la precipitación del yeso en el caso de la disolución de dolomita fue más lento, lo que indica que la velocidad de disolución controla la velocidad de las reacciones. Por último se ha verificado que el recubrimiento de yeso en el caso de la de dolomita ha ocurrido parcialmente en la superficie.

Agradecimientos

Muchas cosas han pasado en el mundo desde que empecé el doctorado: entramos en la crisis global; Obama dos veces presidente; un par de tripletes del Barça; cambiaron un papa alemán con otro argentino; unas cuantas pandemias y tsunamis llenaron los periódicos junto con crisis en Ucrania, en oriente medio y con unas cuantas primaveras árabes …..mientras tanto yo, estoicamente, he estado lidiando con mi personalísima primavera geoquímica. Durante las batallas, muchas personas me han acompañado, suportado, ayudado, animado. Y son tantas, que recopilar una lista completa es imposible. Ya se que me dejaré algún que otro personaje y pido perdón si algunos leyendo esta lista no encuentran su propio nombre. No os ofendáis, no es por vosotros: demencia senil precoz, la llaman los médicos.

Primero quiero darle las gracias a mi familia, que desde lejos y sin tener bien bien claro lo que estuve haciendo, ha estado siempre presente apoyándome incondicionalmente.

Gracias a mis directores por haberme guiado en este laberíntico mundo, Jordi Cama y Pep Soler.

Gracias a Ion Tisseanu, Teddy Craciunescu, Cosmin y Adrian por su gran ayuda durante mi estancia en su departamento de Bucarest y por haberme hecho conocer el Caru cu Bere. Gracias a Jiwhar Ganor y a su grupo: Peter gran ayudante en laboratorio y *Cicero* incomparable y Chen, Itay, Shira, Yigal y Yoav por haber hecho mi estancia en Israel una experiencia inolvidable. Gracias a Christine y Andrew Putnis por pasar largas hora conmigo al microscopio y por recibirme tan bien en Münster.

Gracias a todos los compañeros, que durante estos años se han convertido en buenos amigos, en algunos casos en familia. Compartir la satisfacción cuando las cosas salían bien, la amargura cuando salían fatal, hasta el normal día día es algo imposible de olvidar. Ana, Vanesa, Clara, Manuela, el Che boludo Sebas que se ha dejado querer desde el minuto uno, mi querida Valhondina cuarta hermana con quien he compartido prácticamente todo, Vic compañero de aventuras y del grupo indie-electrónico que nunca montaremos, la Russian que nos ha enseñado el Russiano (idioma que ella solo habla), Maria y Gaby con quien durante años he compartido despacho de 18 m2 (con

todo lo que conlleva) y que son las mejores, Yoar, Linda….. y Ale, claro. Y gracias también a los que me estoy dejando, seguro habéis hecho algo bueno.

Last but not least, gracias particularmente a Jordi F. Cama, gran director, gran persona e inigualable guía. Gracias a él he podido llegar hasta aquí y he aprendido mucho, desde la geoquímica hasta los albatros. La verdad es que sin él hubiera sido toda otra película.

Table of contents

List of figures

List of tables

Part I:

Introduction and efficiency of carbonate minerals in Anoxic Limestone Drainage

Chapter 1

Introduction

1.1 Background and objectives

Acid mine drainage (AMD) is defined as the outflow of acidic water from metal or coal mines both in activity or abandoned. It poses an additional risk to the environment by the fact that it frequently contains elevated concentrations of metals (iron, aluminum, manganese, and possibly other heavy metals) and metalloids (of which arsenic is generally of greatest concern) (Blowes et al., 2003; Brown and Calas, 2011). These contaminants can persist in environment during several centuries after interruption of mining activity (Younger, 1997). The main AMD generating mineral is pyrite (FeS_2), according to the following reactions:

$$FeS_2 + 3.5\ O_2 + H_2O \rightarrow Fe^{2+} + 2\ SO_4^{2-} + 2\ H^+ \quad (1.1)$$

$$Fe^{2+} + 0.25\ O_2 + H^+ \rightarrow Fe^{3+} + 0.5\ H_2O \quad (1.2)$$

$$Fe^{3+} + 3H_2O \rightarrow Fe(OH)_3 + 3\ H^+ \quad (1.3)$$

$$8\ Fe^{3+} + SO_4^{2-} + 14\ H_2O \rightarrow Fe_8O_8(OH)_6(SO_4) + 22\ H^+ \quad (1.4)$$

SO_4^{2-}, Fe(II) and protons are released to solution. Fe(II) is oxidized to Fe(III) according to Eq. (1.2). Fe(III) may precipitate as schwertmannite (Bigham et al., 1996), releasing more protons, or as a Fe(III)-hydroxide (ferrihydrite), also releasing protons. But, at pH lower than 3.5, Fe(III) remains mainly in solution and acts as another oxidizing agent for pyrite according to

$$FeS_2 + 14\ Fe^{3+} + 8\ H_2O \rightarrow 15\ Fe^{2+} + 2\ SO_4^{2-} + 16\ H^+ \quad (1.5)$$

Since AMD can be highly acidic, it has the capacity to dissolve rocks formed by clays and other aluminosilicates. This process releases major rock constituents (e.g., silica, aluminum, iron, sodium, potassium, magnesium, calcium), together with heavy metals, into the environment (Evangelou et al., 1995; Blowes et al., 2003). The main purposes of AMD treatments are retention of metals (precipitation of the contaminant metals) and neutralization of acidity. One of the possible and most common passive treatment systems is the anoxic limestone drainage (ALD), or systems derived from it (e.g., reducing and alkalinity producing systems), characterized by low maintenance needs and low cost (Turner and McCoy, 1990; Heidin et al, 1994; Gazea et al., 1996; Cravotta III and Trahan, 1999; Cravotta III, 2003, 2008; Watten et al., 2005; Watten et al., 2007). ALD uses ditches of buried limestone gravel. Acid water flows through the gravel and limestone dissolves, raising pH and alkalinity, yielding metal retention as Me-oxyhydroxide precipitates. The efficiency of the ALD systems is however limited because secondary mineral precipitation causes the passivation (armoring) of the limestone grains and clogging of the pores, reducing limestone reactivity and acid neutralization (Pearson, A.J. McDonnell, 1975; Santoro et al, 1987; Hammarstrom et al., 2003; Watzlaf, et al. 2004; Santomartino and Webb, 2007; Caraballo et al., 2009a; Caraballo et al., 2009b). In addition, the presence of aqueous sulfate leads to gypsum precipitation (Booth et al., 1997; Huminicki and Rimstidt, 2009; Soler et al., 2008), which essentially contributes to passivation and affects greatly the efficiency of the treatment systems. Soler et al. (2008) reproduced at the laboratory scale the behavior of ALD systems using column reactors filled with limestone grains. Injecting acid solutions (pH 2, HCl and H_2SO_4) with initial concentrations of Fe(III) ranging from 9.27×10^{-3} to 3.61×10^{-2} mol L^{-1}, it was observed that (1) gypsum coating was responsible for calcite passivation, (2) passivation time in the column was dependent on the initial aqueous sulfate concentration and (3) change in porosity and permeability was due to precipitation of both gypsum and Me-oxyhydroxides. Moreover, once the columns were passivated, X-ray microtomography was used a posteriori to examine the precipitates responsible for the porosity changes.

To enhance our knowledge on the loss of calcite reactivity due to grain coating or clogging of porosity initially discussed by Soler et al. (2008), in the **first part of this PhD study** three main innovations are presented. The first innovation is that new column experiments were performed using calcite, aragonite or dolomite sand and

synthetic acid solutions not only containing Fe(III)-SO_4^{2-}-H^+ as in Soler et al. (2008), but also containing Al-SO_4^{2-}-H^+ as major components at pH 2 and pH 3. This strategy allows investigation of the efficiencies of each carbonate mineral for AMD treatments. Concentrations of Fe(III) and Al ranged from 3.49×10^{-3} to 2.60×10^{-2} mol L^{-1} and from 3.60×10^{-3} to 3.61×10^{-2} mol L^{-1}, respectively, which fall in the range found in AMD (Nordstrom et al., 2000; Blowes et al., 2003).

The second innovation is that in the present study, in order to clarify how the secondary phases precipitate and influence the porosity change, several X-ray microtomography (mCT) measurements were carried out. mCT images were collected at different times during the experiment (before the experiment start and several times till the end of the experiment) with the goal of (i) allowing an accurate characterization of the passivation mechanism, which consists of calcite dissolution, consequent surface coating by gypsum precipitates and precipitation of metal oxyhydroxides, and (ii) quantifying porosity changes during the experiments, the contribution of metal oxyhydroxides in the decrease in porosity, and the role of gypsum in the calcite passivation mechanism.

Reactive transport modeling is a suitable tool for interpreting mathematically the coupled physical and chemical processes occurring in the passive treatment systems. The third innovation is that in this study, the reactive transport code CrunchFlow (Steefel et al., 2015) was used to simulate the processes occurring in the calcite column experiments. As the calcite passivation mechanism (gypsum coating on calcite surface) is not implemented in the code, the following was considered. Assuming that the gypsum coating reduces the calcite reactive surface area, a decrease in calcite area was forced at different times to fit the model results to the experimental data. The resulting simulations allow quantification of the phenomena responsible for the changes in passive treatment efficiency.

Gypsum precipitation on calcite surface has a key role on the efficiency of ALD treatment of acid mine drainage. **The second part** of this Thesis is then focussed on learning about the overall process of calcium carbonate mineral (calcite and dolomite) dissolution and gypsum precipitation in acid sulfate solutions.

Given the role of gypsum precipitation on the course of natural and anthropogenic systems tied to the reactivity of carbonate minerals, a number of experimental studies in the literature focused on (1) the coupled reactions of calcite dissolution and gypsum precipitation and (2) the mechanisms controlling gypsum precipitation (Booth et al.

1997; Wilkins et al.; 2001; Huminicki and Rimstidt; 2009; Reznik et al., 2011; Rosenberg et al., 2012; Atanassova et al., 2013; Ruiz-Agudo et al., 2015). The experimental methodologies and techniques used in these studies provided macroscopic results based on the variation in released and captured cations into and from aqueous solutions and high-resolution microscopic measurements of the mineral surfaces using atomic force microscopy (AFM), under experimental conditions in which pH ranged from 1 to 7 and temperature was below 100 °C. Conclusive remarks from the previously cited studies with regards the coupled reactions can be summarized as:

(1) Epitaxial growth of gypsum takes place over carbonate mineral substrates and the gypsum nucleation induction time is shorter during calcite dissolution. Gypsum precipitation results from a two-step process. First, calcite or dolomite dissolves, observed in the regular formation of rhombohedral etch pits and step retreat, releasing Ca^{2+} or Ca^{2+} and Mg^{2+} to solution. Secondly, the solution at the mineral–solution interface becomes supersaturated with respect to gypsum, which then precipitates. Surface coating becomes uniform all over the calcite surface, yielding calcite passivation (reduction of calcite reactivity). Arrow-shaped gypsum crystals evolve along the etch pit crystallographic directions ([441] and [481]) (Booth et al., 1997; Wilkins et al., 2001).

(2) Gypsum may precipitate from a thin fluid layer while the bulk fluid remains undersaturated. Salinity and temperature enhance the replacement mechanism (CaCO3 substrate is pseudomorphically replaced by the product ($CaSO_4 \cdot 2H_2O$); Ruiz-Agudo et al., 2015).

From the studies that dealt with the mechanisms of gypsum precipitation (nucleation and growth) it was concluded that:

(1) Background electrolytes (Na^+ and K^+) influence gypsum growth rate by retarding the precipitation kinetics as background electrolytes are adsorbed onto the forming mineral (Zhang and Nancollas, 1992; Reznik et al., 2009).

(2) The gypsum precipitation rate in the absence of a Ca-carbonate substrate is expressed as (Reznik et al., 2011; Rosenberg et al., 2012):

$$\frac{Rate}{S_{BET}} = k_1 \cdot \left(\Omega^{0.5} - 1\right)^{10} + k_2 \cdot \left(\Omega^{0.5} - 1\right)^{2} \qquad (1.6)$$

where SBET is the BET surface area of gypsum (m^2 g^{-1}), $\Omega = 10^{SI}$, where SI is the saturation index with respect to gypsum, and k_1 and k_2 are rate coefficients (mol m^{-2} s^{-1}) that depend on pH.

Within this line of work, **this second part of the PhD study** deals with the coupled reactions of dissolution of carbonate minerals and gypsum precipitation and attempts to discern differences and similarities of the overall mechanism when calcite, aragonite or dolomite dissolve. In addition, the gypsum precipitation rates on the Ca-carbonate substrate are quantified allowing a comparison with the precipitation rate calculated from the rate law proposed by Reznik et al. (2011) and Rosenberg et al. (2012). To this end, batch experiments at constant temperature (25 ± 1°C) and atmospheric pressure were carried out in acidic solutions at pH 2 (H_2SO_4) and equilibrated with respect to gypsum ($CaSO_4 \cdot 2H_2O$) in which Ca-carbonate samples of different size (powder, grains and fragments) acted as substrate.

To learn about the overall process of calcium carbonate mineral (calcite and dolomite) dissolution and gypsum precipitation in acid sulfate solutions at the micro-nanoscale, **in-situ atomic force microscopy (AFM) experiments** were carried out. This approach allows for a visualization of the processes occurring at the reacting carbonate surface.

In the literature, many studies have dealt with carbonate mineral reactivity (Hillner et al., 1992; Shindo and Ohashi, 1998; Arvidson et al., 2006; Astilleros et al., 2010; Laresen et al., 2010; Ruiz-Agudo et al., 2010; Pina et al., 2010; Ruiz-Agudo and Putnis, 2012; Urosevic et al, 2012). In particular, the study of calcite dissolution and gypsum precipitation by Booth et al. (1997) is relevant for our experimental AFM study as the authors provided SEM and AFM observations (in situ and ex situ) of the overall process of gypsum coating on calcite (causing passivation or armoring) at pH 1 and 2 in mixed HCl and Li_2SO_4 solutions. They reported on i) the reduction of calcite reactivity due to the gypsum coating, ii) the shape of gypsum crystals (rows parallel to the flux) and iii) the relation between anions and cations of the lattices of both calcite and gypsum. It was suggested that the likely match between cations favors the epitaxial overgrowth of the gypsum (010) face on top of the calcite cleavage plane.

In this study, to enhance the current knowledge about the complementary processes of calcite/dolomite dissolution and gypsum precipitation, two types of solutions were used: (1) acid sulfate solution (Na_2SO_4) undersaturated with respect to gypsum and (2) acid sulfate solution ($CaSO_4$) equilibrated with respect to gypsum. The experimental pH

ranged from approximately 2 to 6 and the in-situ AFM experiments were run at ambient temperature (23 ± 1°C) and pressure.

1.2 Thesis outline

This thesis consists of three parts with six chapters based on manuscripts that are already published, under review or in preparation.

Part - I Introduction and efficiency of carbonates in ALD's - *Chapters 1, 2 and 3*

- *Chapter 1* presents the objectives and motivation of this study.

- *Chapter 2* presents the effect of pH, initial metal and sulfate concentration, residence time and flow rate in column experiments with calcite sand run at constant flow.

- *Chapter 3* dolomite and aragonite are studied as alternative minerals in ALD with the same conditions of the calcite experiments. Mineral and porosity changes have been also studied by x-ray micro tomography (mCT) and x-ray microdiffraction (mRD) measurements.

Part II - Processes regulating gypsum coating on carbonate mineral's surface - *Chapters 4 and 5*

- *Chapter 4* describes a set of batch experiments employing Iceland spar, dolomite and aragonite in contact with acid solution equilibrated with respect to gypsum centred on the kinetics of coupled dissolution/precipitation mechanism.

- *Chapter 5* presents in-situ AFM observations in the study of nucleation and gypsum growth in calcite and dolomite surfaces under acidic conditions simulating natural sulfate concentrations and pH in natural AMD.

Part III – Conclusions - *Chapter 6*

- *Chapter 6* summarizes the main contributions of this thesis and perspectives.

Chapter 2†

Efficiency of limestone in passive treatments for AMD: column experiments and 1D modeling

2.1 Introduction

This chapter focuses on the performance of column experiments filled with calcite that were conducted under atmospheric pressure and 25 ºC conditions. Input solutions (H_2SO_4) had different concentrations of Fe(III), Al and sulfate. To clarify how the secondary phases precipitate and influence the porosity change, several X-ray microtomography (mCT) measurements were carried out. mCT images were collected at different times during the experiment (before the experiment start and several times till the end of the experiment). In addition, the experimental data were reproduced by means of 1D reactive transport calculations to evaluate mineral reaction rates in the system (fitted in the model through the reactive surface area term) and to quantify the porosity variation. The CrunchFlow (Steefel et al., 2015) numerical code was used to conduct the simulations.

† the present chapter is based on the paper: *Processes affecting the efficiency of limestone in passive treatments for AMD: Column experiments* by Francesco G. Offeddu, Jordi Cama,, Josep M. Soler , Gabriela Dávila, Alastair McDowell, Teddy Craciunescu, Ion Tiseanu in Journal of Environmental Chemical EngineeringVolume 3, Issue 1, pages 304–316.

2.2 Materials and methods

2.2.1 Sample preparation and characterization

Limestone sand was obtained from the Roca Quarry in the Garraf area (Barcelona). This sand was used by Soler et al. (2008) and XRD profiles showed only calcite peaks. The grain size used in the experiments was 1-2 mm. To remove calcite microparticles in the column, grains were pre-washed with de-ionized water several times until clear output water was collected. Thereafter grains were dried at 50 ºC for 24 h. The specific surface area of the non-reacted sample was 0.447 m^2 g^{-1} measured by the BET method using 5-point N_2 adsorption isotherms on a Micromeritics ASAP 2000 surface area analyzer.

2.2.2 Column experiments

Cylindrical columns were made from transparent polymethyl methacrylate with inner diameters ranging from 1.2 to 2.6 cm and lengths ranging from 1.1 to 6 cm (Tables 2.1 and 2.2). Diameters were sufficiently large so they were about an order of magnitude larger than the limestone grain size. Lengths were sufficiently small so passivation (gypsum coating of the limestone grains) could be achieved in a reasonably short time. All columns included a bed of glass beads (2 mm in diameter) of 3 mm of thickness at the top and bottom to homogenize the influent and effluent solutions (Fig. 2.1a). Columns were hand filled with the pre-washed calcite grains. In a few columns, calcite grains were mixed with glass beads (33 wt% of grains and 67 wt% of beads) to improve solution circulation (Fig. 2.1b). Column porosity was calculated from the known calcite mass, volume of the column and calcite density (2.71 g cm^{-3}) and also from the acquired mCT images of the columns using the gray-scale segmentation method.

Table 2.1 *Experimental conditions in the aluminum-column experiments*

column	weight limestone (g)	Al (M)	SO_4 (M)	column length (cm)	column diameter (cm)	porosity (%)	t_{pass}/t	time (h)	mg Al / g calcite
17	19.8	3.61E-02	5.92E-02	2.5	2.6	45	67	210	20
16	18.8	1.80E-02	3.19E-02	2.4	2.6	46	180	547	27
11	19.7	9.27E-03	1.89E-02	2.7	2.6	49	44	162	4
10	18.5	7.20E-03	1.58E-02	2.6	2.6	51	323	1183	24
4	17.0	7.20E-03	1.13E-02	2.6	2.6	55	291	1147	25
2	14.5	3.60E-03	5.89E-03	2.1	2.6	52	623	1893	24
9	19.0	3.60E-03	1.04E-02	2.6	2.6	49	396	1411	14
C	1.8	1.80E-02	3.19E-02	1.1	1.2	46	101	142	15
A	1.6	9.27E-03	1.89E-02	1.2	1.2	57	152	291	18
M	1.6	7.20E-03	1.58E-02	1.1	1.2	51	178	280	13
N	1.8	7.20E-03	1.58E-02	1.2	1.2	50	168	280	12
6 CAL	15.0	1.80E-02	3.19E-02	6	2.6	40	73	501	31
7 CAL	14.0	3.60E-03	1.04E-02	6	2.6	40	460	3330	44
8 CAL	14.1	3.60E-03	1.04E-02	6	2.6	40	418	3018	40
9 CAL	14.0	3.60E-03	1.04E-02	6	2.6	40	444	3211	42

All column experiments run at $1x10^{-3}$ L m^{-2} s^{-1}; initial pH is 2 except in columns 4 and 2 where it is 3; all column experiments were passivated. t/τ denotes passivation time normalized with respect to residence time; mg Al/g limestone denotes amount of aluminum retained by limestone.

Table 2.2 *Experimental conditions in the iron-column experiments.*

column	weight limestone (g)	Fe (M)	SO_4 (M)	column length (cm)	column diameter (cm)	porosity (%)	flow rate ($L/m^2/s$)	t_{pass}/τ	time (h)	mg Fe / g calcite	passivated
3	16.40	2.60E-02	4.39E-02	2.8	2.6	59	1.0E-03	141	593	101	YES
8	18.47	1.34E-02	2.51E-02	2.5	2.6	47	1.0E-03	117	331	26	YES
7	19.86	6.72E-03	1.51E-02	2.5	2.6	45	1.0E-03	263	743	27	YES
2 CAL	13.23	8.70E-03	1.80E-02	1.6	2.6	43	1.0E-03	301	518	36	YES
3 CAL	14.65	8.70E-03	1.80E-02	1.7	2.6	40	1.0E-03	972	1676	107	YES
4 CAL	14.63	3.49E-03	1.02E-02	1.8	2.6	44	1.0E-03	2241	4438	113	YES
5 CAL	14.21	3.49E-03	1.02E-02	1.7	2.6	42	1.0E-03	2651	4774	125	CLOG.
1A	1.71	3.49E-03	1.02E-02	1.2	1.2	54	1.0E-03	1273	2201	105	CLOG.
2A	1.56	3.49E-03	1.02E-02	1.2	1.2	58	1.0E-03	744	1385	72	YES
7A	1.67	3.49E-03	1.02E-02	1.1	1.2	50	6.0E-04	1827	1185	33	CLOG.
H	1.86	1.74E-02	3.11E-02	1.2	1.2	49	1.0E-03	188	300	66	YES
D	1.76	1.34E-02	2.51E-02	1.2	1.2	52	1.0E-03	239	402	72	YES
E	1.60	1.34E-02	2.51E-02	1.1	1.2	53	1.0E-03	231	359	71	YES
1 CAL	1.46	8.70E-03	1.80E-02	1.2	1.2	60	1.0E-03	1021	1990	278	CLOG.
F	2.21	1.74E-02	3.11E-02	1.3	1.2	45	6.0E-04	132	360	38	YES
B	1.68	1.34E-02	2.51E-02	1.1	1.2	50	6.0E-04	434	1127	121	CLOG.
B bis	1.61	1.34E-02	2.51E-02	1.2	1.2	56	6.0E-04	355	1129	126	YES
LCAL1 mix	15.00	1.74E-02	3.11E-02	6	2.6	42	1.0E-03	199	1269	158	YES
LCAL2 mix	15.00	1.74E-02	3.11E-02	6	2.6	41	1.0E-03	205	1270	158	YES

Initial pH = 2; t/τ denotes passivation time normalized with respect to residence time; "mix" indicates column filled with calcite and glass beads (30 and 70 wt %, respectively); mg Fe/g limestone denotes amount of iron retained by limestone.

The initial porosity, based on density calculations and mCT measurements, ranged from 40 to 60 % (Tables 2.1 and 2.2). Input solutions were injected from the column bottom upwards by a Gilson peristaltic pump under constant flow rate, yielding fluxes of $6x10^{-4}$ and $1x10^{-3}$ L m^{-2} s^{-1}. Residence time ranged from 1.6 to 3.4 h. The experiments run for mCT measurements (see below) were temporarily stopped at different times in order to acquire the mCT images before the experiment (d0) and after 4, 8 and 12 days (d4, d8 and d12). After each image acquisition the experiments were restarted again.

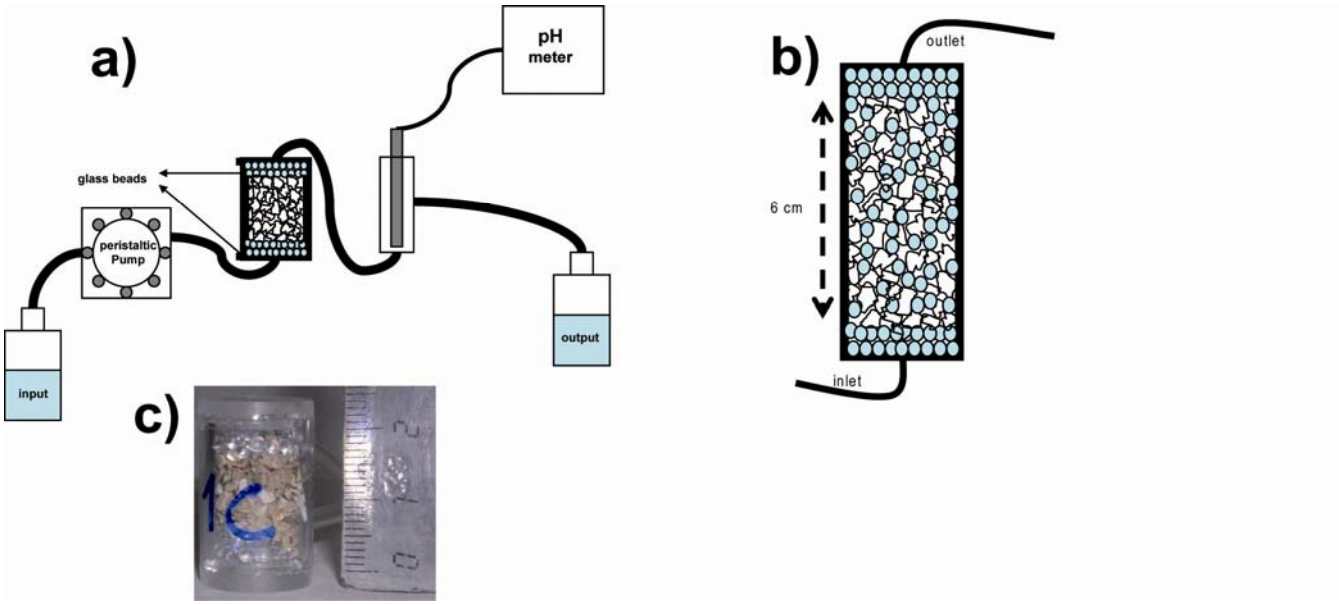

Figure 2.1 *(a) Scheme of the experimental setup. (b) Scheme of a mixed long column (diameter 2.6 cm, length 6 cm). In addition to the layers of glass beads at the bottom and top, glass beads were mixed with the calcite grains (67 wt% and 33 wt%, respectively). (c) Photograph of an assembled column (1.2 cm x 1.2 cm).*

After the experiments, epoxy resin was injected in some columns. Once it hardened, the column was cut into slices for further mineralogical inspection by scanning electron microscopy (SEM) and micro X-ray diffraction (mXRD). Most experiments were replicated three times.

2.2.3 Solutions

Input solutions were made from adequate amounts of $Fe_2(SO_4)_3{\cdot}5H_2O$ and $Al_2(SO_4)_3{\cdot}16H_2O$ reagents (pro analysis grade) and Millipore MQ water (18 MΩ cm). The solutions (H_2SO_4) had initial concentrations of Fe(III) ranging from $3.49x10^{-3}$ to $2.60x10^{-2}$ mol L^{-1} and of Al ranging from $3.60x10^{-3}$ to $3.61x10^{-2}$ mol L^{-1}. Sulfate

concentrations ranged from $1.02x10^{-2}$ to $4.39x10^{-2}$ mol L^{-1} for iron columns and from $1.04x10^{-2}$ to $5.92x10^{-2}$ mol L^{-1} for aluminum columns. In most of the experiments solution pH was 2 and only in two aluminum experiments the pH was 3. pH was adjusted by adding concentrated H_2SO_4 to the iron sulfate or aluminum sulfate solutions (Tables 2.1 and 2.2).

2.2.4 Analytical methods

Input and output concentrations of Fe, Al, S, Mg, Ca, Na and Si were measured by Inductively Coupled Plasma - Atomic Emission Spectrometry (ICP-AES), using a Thermo-Jarrel Ash spectrometer equipped with a CID detector. The detection limits for Fe, S, Mg, Ca, Al and Si were 1.8×10^{-7}, 3.5×10^{-6}, 10^{-5}, 5×10^{-6}, 7.5×10^{-7} and 7×10^{-7} mol L^{-1}, respectively. The error associated with ICP-AES measurement was estimated to be around 3%, based on measurement of different standard solutions in the calibration process. The solution pH was measured during the experiments with a Thermo Electron Orion 720 A+ pH meter at room temperature (22 ± 2 ºC) with an error of ± 0.02 pH units. The electrode was regularly calibrated with buffer solutions at pH 2 and 7. The output solution pH was continuously measured by placing the electrode in a sealed tube in which the output solution circulated (Fig. 2.1a). The saturation indexes for calcite and gypsum were calculated at 25 °C using the PHREEQC code (Parkhurst and Appelo, 2013) and MINTEQ database (Allison et al., 1991).

Two sets of X-ray microtomography (mCT) images were taken using two different X-ray sources. The reason was time availability for the instruments. The first set was taken at the 8.3.2 beamline of the Advanced Light Source (ALS, Berkeley, California). Images were taken at X-ray energy of 40keV using a superbend magnet source and a multilayer monochromator. The columns were mounted on a rotary stage and images were collected every 0.25º through a full 180º rotation. Transmitted X-ray light was converted to visible light using a $CdWO_4$ single crystal scintillator, magnified by a Cannon 2X lens, and imaged on a Cooke PCO 4000 CCD camera with a final pixel size of 4.4 µm. Three exposures of 200 ms each were averaged together for a total of 600 ms exposure per image. Nine dark images (with X-ray shutter closed) and 25 open beam images (with sample removed from beam) were taken at the end of the data collection

and used for background subtraction and normalization. Raw images were reconstructed using the Octopus commercial software package (Dierick et al., 2004).

A second set of mCT images was taken at the National Institute for Lasers, Plasma and Radiation Physics (NILPRP, Bucharest-Magurele, Romania). The mCT equipment worked with Cone beam CT rapid scan (180° + ½ fan angle), Oblique View Cone Beam. X-ray energy was 225 kVp and a maximum power of 10/15 W, using a tungsten filament source. The columns were mounted on a rotary stage, and images were collected every 0.5º. The linear detector, using 1,024 scintillator - photo diode assemblies, yielded 16-bit output digital files that were reconstructed using the VGstudio Max 2.0 software package (Volume Graphics: http://www.volumegraphics.com). All mCT images were taken before and during the experiments at regular time intervals. The segmentation method (separation of gray-scale range values) was applied to quantify porosity using the ImageJ software (Schneider et al., 2012). This method permits separation and measurement of the pore space between calcite grains and precipitates over the whole image pack.

Quantification of precipitated gypsum and oxyhydroxides was carried out manually using the Amira 5.2 3D visualization software (http://www.amira.com). Since acquirement of mCT images is based on the different density of the materials, and the density of Al-hydroxides is very low, it was impossible to obtain mCT images of the Al-compounds in the aluminum columns. Hence, only the mCT images in some of the iron columns were used to characterize the mineral variation with time at different time intervals. Time to capture the mCT images was ~ 2 h. In the mCT images each mineral (calcite, Fe-oxyhydroxides, gypsum, glass beads) has a different gray color according to its density and composition (X-ray absorption coefficient). The pore space is black.

In order to identify the mineral phases in the columns, X-ray microdiffraction (mXRD) measurements of several thin sections from the passivated columns were performed at the 12.3.2 beamline, ALS (Berkeley, California). The instrument uses Kirkpatrick-Baez optics to focus the monochromatic X-ray beam delivered by the synchrotron superconducting magnet source down to a size of about 15x2 μm^2 at the sample position. The sample was mounted on a precision XY stage and illuminated with a 8 keV (λ = 1.55 Å) monochromatic X-ray radiation at an incidence angle of 10º. Iron X-

ray fluorescence signal was also collected using a Si-drift Vortex detector. mXRD patterns were obtained using a MAR133 X-ray CCD detector. The CCD was set to an angle of 2θ = 40º at a distance of 119 mm from the sample. The exposure time per point for the diffraction patterns was 200 s. The signal collection time per point for fluorescence was 0.2 s.

Scanning Electron Microscopy (SEM) images were taken on C-coated samples using a Hitachi H-4100FE instrument under a 15–20 kV potential.

2.2.5 Reactive transport modeling

One-dimensional simulations of the column experiments were performed using the CrunchFlow reactive transport code (Steefel et al., 2015). Crunchflow solves numerically the adversion-dispersion-reactions equations

$$\frac{\partial(\phi C_i)}{\partial t} = \nabla \cdot (\mathbf{D} \nabla C_i) - \nabla(\mathbf{q} C_i) + R_i \qquad (i = 1, 2, 3, \ldots, n) \qquad (2.1)$$

where ϕ is porosity, C_i is the concentration of component i (mol m^{-3}), q is the Darcy velocity (m^3 m^{-2} s^{-1}), R_i is the total reaction rate affecting component *i* (mol m^{-3} rock s^{-1}) and D is the combined dispersion-diffusion coefficient (m^2 s^{-1}). The total reaction rate for component *i* is given by

$$R_i = -\sum_m \upsilon_{im} \cdot R_m \qquad (2.2)$$

where R_m is the rate of precipitation ($R_m > 0$) or dissolution ($R_m < 0$) of mineral *m* per unit volume of rock, and v_{im} is the number of moles of *i* per mole of mineral *m*. Since mineral reactions are described using kinetic rate laws, initial mineral surface areas and several reaction rate parameters have to be supplied by the user as input. In the simulations, the reaction rate laws that have been used are of the form (Caraballo et. al, 2011)

$$R_m = A_m \sum_{terms} k_m a_{H^+}^n (\Omega_m - 1) \tag{2.3}$$

where A_m is the reactive surface area of the mineral (m^2 m^{-3}), k_m is the rate constant (mol m^{-2} s^{-1}) and $a_{H^+}^n$ is a term describing the dependence of the rate on pH. The term in brackets stands for the effect of solution saturation state.

$$\Omega_m = IAP_m / K_m \tag{2.4}$$

where IAP_m is the ionic activity product of the solution with respect to the mineral and K_m is the equilibrium constant for the dissolution reaction (ionic activity product at equilibrium). If $\Omega_m < 1$, the solution is undersaturated and the reaction is of dissolution; if $\Omega_m > 1$, the solution is supersaturated and the reaction is of precipitation; at equilibrium $\Omega_m = 1$ and $R_m = 0$.

Changes in mineral surface area A_m (m^2/m^3bulk) due to reaction are calculated according to

$$A_m = A_m^{initial} \left(\phi_m / \phi_m^{initial} \right)^{2/3} \left(\phi / \phi^{initial} \right)^{2/3} \quad \text{(dissolution)} \tag{2.5}$$

$$A_m = A_m^{inital} \left(\phi / \phi^{initial} \right)^{2/3} \quad \text{(precipitation)} \tag{2.6}$$

where ϕ_m is mineral volume fraction. The inclusion of a 2/3 dependence on porosity is chiefly to ensure that as the porosity goes to 0, so too does the mineral surface area available for reaction. This formulation is used primarily for primary minerals (that is, minerals with initial volume fractions > 0). For secondary minerals which precipitate, the value of the initial bulk surface area specified is used as long as precipitation occurs—if this phase later dissolves, the above formulation is used, but with an arbitrary "initial volume fraction" of 0.01.

2.3 Results and Discussion

Tables 2.1 and 2.2 show the experimental conditions of the aluminum and iron column experiments, respectively. The experiments lasted from 142 to 4774 h depending on their geochemical evolution.

2.3.1 Aluminum columns

Figure 2.2a shows variation of the output concentrations of Ca, SO_4 and Al and output pH in a representative Al column experiment (experiment 16 in Table 2.1). Initial pH was 2 and initial Al and sulfate concentrations were 2.22×10^{-2} mol L^{-1} and 3.75×10^{-2} mol L^{-1}, respectively. As the solution reacted with calcite, the output pH increased to pH between 6 and 7.5 (for ~ 260 h) and dissolved Al was completely depleted. The concentration of Ca raised to ~ 1.6×10^{-2} mol L^{-1} and the output concentration of sulfate decreased to ~ 1.6×10^{-2} mol L^{-1}. Therefore, at this stage (Fig. 2.2a) the calcite-filled column was acting as expected, removing Al from solution, decreasing sulfate concentration and neutralizing acidity. PHREEQC calculations showed that the output solution was undersaturated with respect to calcite, but supersaturated with respect to Al-hydroxide (gibbsite ($Al(OH)_3$) and gypsum ($CaSO_4 \cdot 2H_2O$). Both gypsum and gibssite were identified by mXRD and SEM, indicating that both phases precipitate under these conditions (Fig. 2.3a, c, and e). After 260 h (stage II), the output pH and the output Ca concentration gradually decreased to approach a nearly constant value of ~ 4 and ~ 8.0×10^{-3} mol L^{-1}, respectively, until the end of the experiment (Fig. 2.2a).

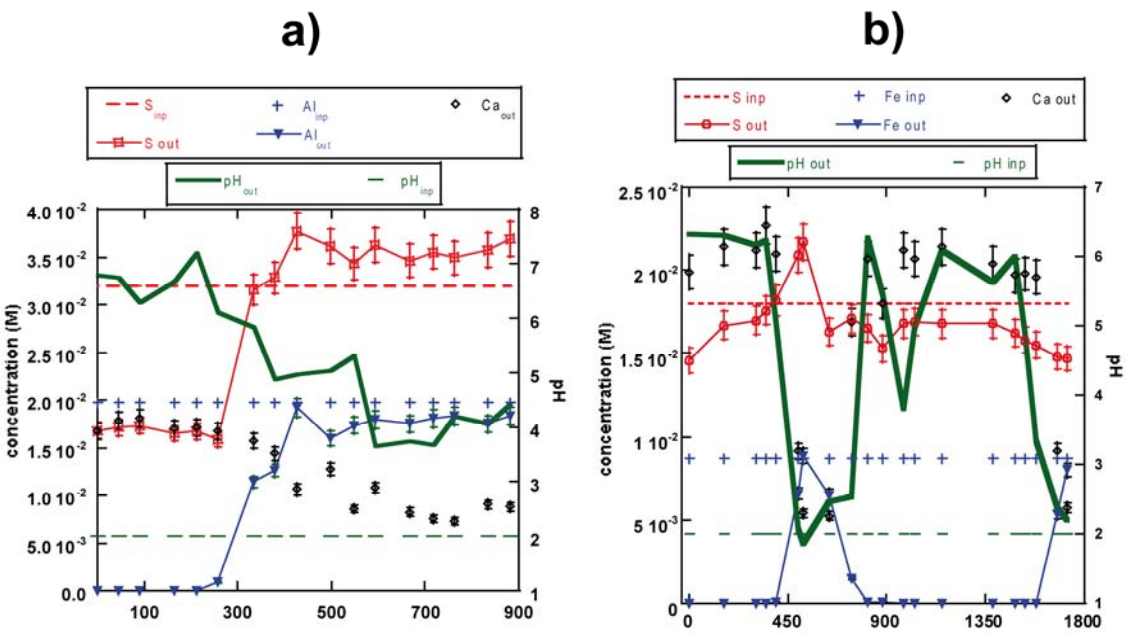

Figure 2.2 *(a) Variation of output pH and output concentrations of Al, Ca and SO4 with time in experiment 16 (Table 2.1). (b) Variation of output pH and output concentrations of Fe, Ca and SO4 with time in experiment 3 CAL.*

Output concentration of SO_4 and Al increased up to the input concentrations. Therefore, this behavior suggests that calcite dissolution diminished likely due to gypsum precipitation on the calcite grain surfaces (*armoring* or *coating* effect), limiting, but not totally avoiding, the buffer capacity of calcite.

2.3.2 Iron columns

The variation in the Fe concentration in the Fe(III) columns was similar to that of the Al column experiments. Figure 2.2b depicts the variation of the output concentration of Ca, Fe, SO_4 and pH. Dissolution of calcite increased the output pH (~ 6) and the Ca release (up to 2.27 x 10^{-2} mol L^{-1}). Precipitation of gypsum and Fe-oxyhydroxide (goethite) was clearly observed and identified (Fig. 2.3b, d and f).

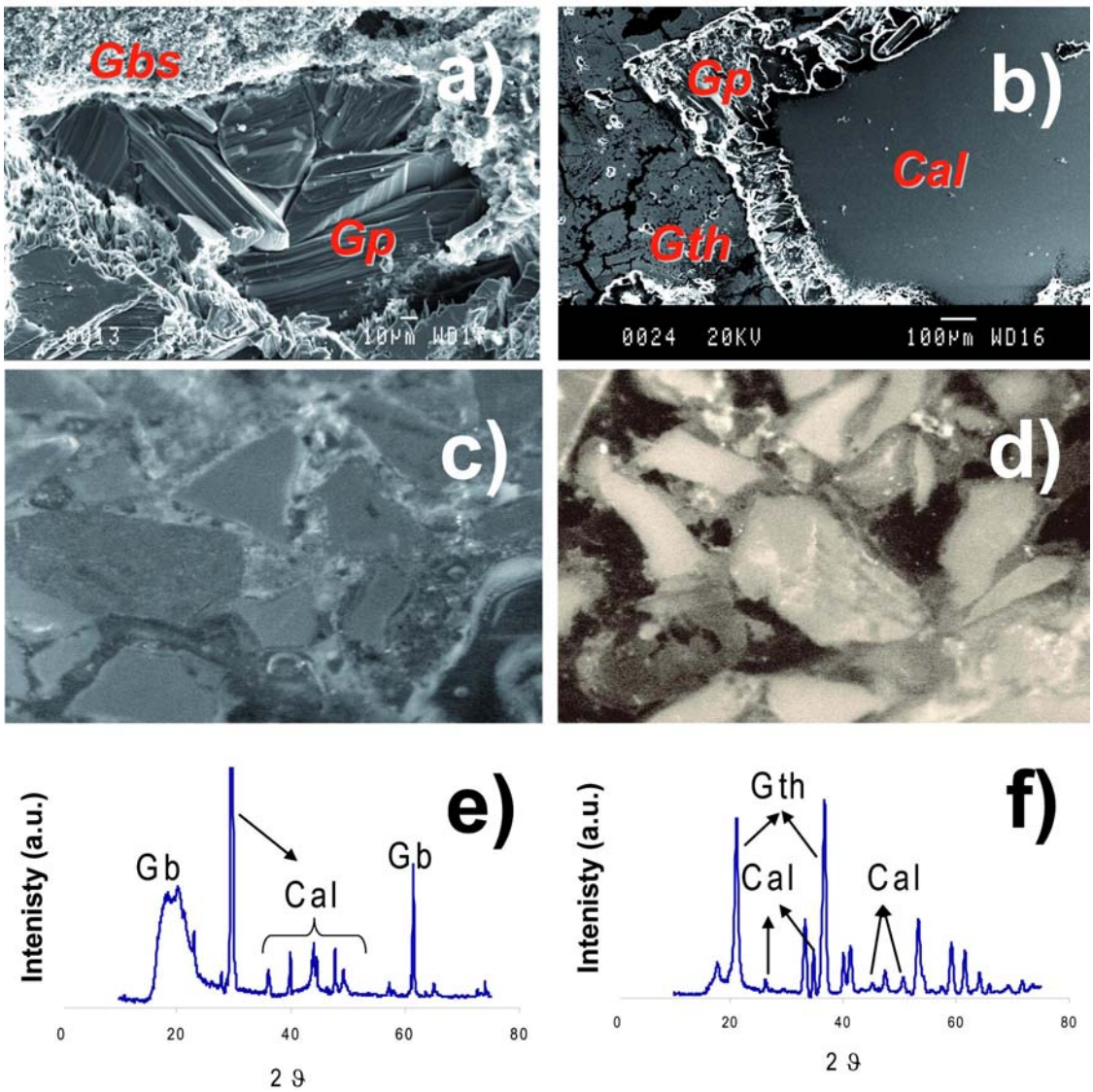

Figure 2.3 *(a) SEM image showing gypsum crystals that coat a calcite grain (not visible under the precipitates) in experiment 16 (Table2. 1). The surrounding material is Al-hydroxide precipitate (gibbsite) which was identified by X-ray microdiffraction (a and e). (b) SEM image that shows a calcite grain on the right, a gypsum coating and Fe-oxyhydroxide (goethite) in a representative passivated column (1 CAL, 8.7x10^{-3} mol L^{-1} Fe(III), 1.8x10^{-2} mol L^{-1} SO_4^{2-} and pH 2). (c) and (d) Optical micrographs of the samples. (e) and (f) mXRD profiles indicating the presence of gibbsite, goethite and calcite.*

After 350 h, the output pH sharply dropped to ~ 2, the concentration of total Fe increased to the initial level, and Ca decreased to 5.4 x 10^{-3} mol L^{-1}. SO_4 concentration was higher than the initial one. This variation suggests that calcite was losing reactivity and the precipitated gypsum was dissolving. However, after ca. 750 h, the output pH and Ca increased back up to 6 and 2.1 x 10^{-2} mol L^{-1}, respectively, the total SO_4 decreased to ~ 1.6 x10^{-2} mol L^{-1}, and iron was depleted. This behavior indicated that calcite dissolution resumed to yield gypsum and goethite precipitation. Finally, after

~1550 h a second, perhaps definitive calcite passivation occurred before the end of the experiment.

2.3.3 Passivation and clogging processes

The dissolution of calcite in the experiments released Ca from the limestone grains, which combined with the SO_4 in solution and caused precipitation of gypsum on the calcite surfaces. Gypsum coating of the grains eventually prevented access of solutes to the grain surfaces and calcite dissolution (passivation). As a result of passivation, output pH dropped to values close to the input value, metal retention stopped and SO_4 concentrations increased to levels close to the input value (or even higher if gypsum dissolved). The time required to reach passivation (passivation time, t_{pass}), depended on the input concentration of SO_4, which correlated with metal concentration (Fe and Al were added as sulfate salts). It was considered that columns were passivated when pH remained at values near that of the input solution for 5 consecutive days.

Figures 2.4a and 2.4c show plots of t_{pass} normalized to residence time τ (column length divided by initial linear velocity) vs. initial SO_4 concentration. The tendency observed in both Fe and Al columns is that t_{pass} increased when decreasing the input sulfate (and metal) concentrations (Fig. 2.4a, c). This trend was already observed by Soler et al. (2008) in Fe column experiments using two different limestone grain sizes (1-2 and 2-5 mm). In the Al column experiments, t_{pass} also tends to be higher in the experiments run at pH 3 than in those at pH 2.

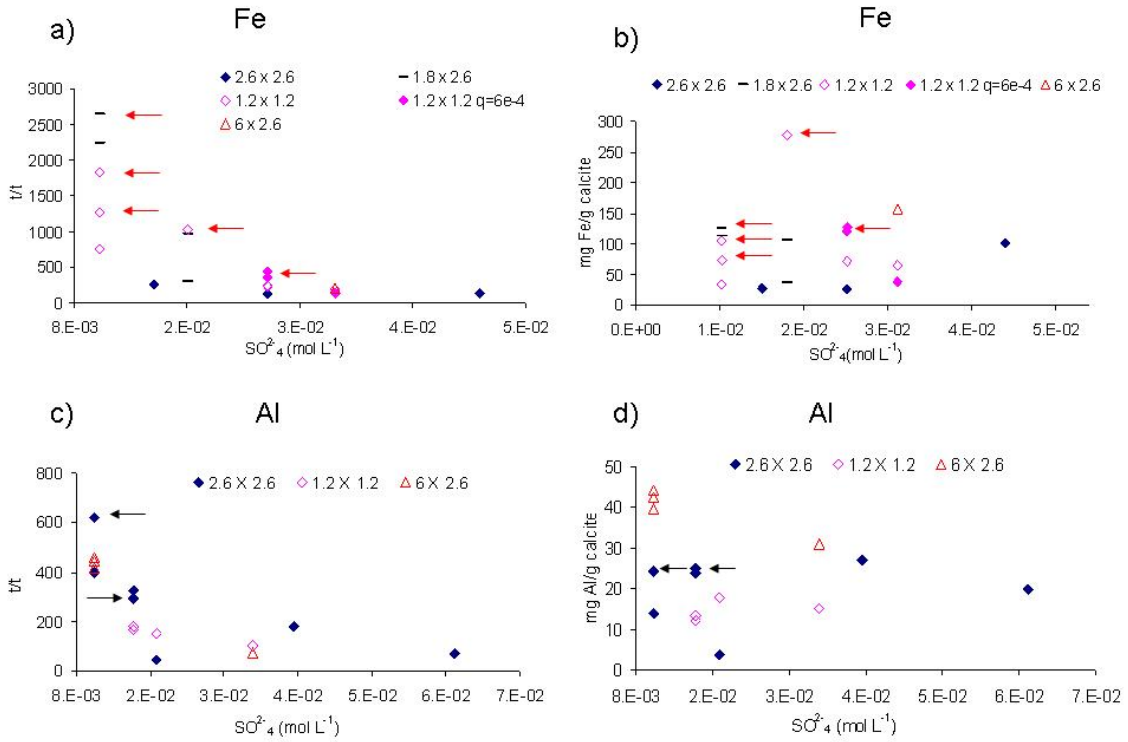

Figure 2.4 *Plots of passivation time normalized to residence time (τ) vs. input concentration of SO_4 are shown in (a, column experiments with $Fe_2(SO_4)_3$ input solutions) and (c, column experiments with $Al_2(SO_4)_3$ input solution). Plots of metal retention vs. input SO_4 concentration are shown in (b) and (d). The red arrows in (a) and (b) indicate columns that underwent clogging. Black arrows in (c) and (d) represent experiment runs with input solution at pH 3. Different symbols represent different column sizes (length and diameter). Flow rate in all experiments is $1.0x10^{-3}$ L m^{-2} s^{-1}.*

Calcite dissolution also caused an increase in pH from 2 to ~ 6-7 (proton consumption), resulting in supersaturation of the solutions with respect to Fe- or Al-oxyhydroxides. Clogging of the pore space was observed in some experiments (flow stopped due to the decrease in permeability). Time required to clog the columns was larger than passivation times (arrows in Figs. 2.4a, b), indicating that when efficiency was better (i.e. the columns lasted longer), clogging took place before any passivation could be observed. Clogging was caused by the precipitation of metal-oxyhydroxides between the grains.

To check reproducibility of results most experiments were repeated at least 3 times. Reproducibility was little, as significant variability in t_{pass}/τ was observed (Tables 2.1 and 2.2). For example, results from Fe experiments with initial SO_4 concentration of ~$1.0x10^{-2}$ mol L^{-1} show that time to reach clogging ranged from ~700 to ~2600 t/τ (Fig.

2.4a). Another factor to take into consideration was the occurrence of temporary calcite passivation events and subsequent reactivations. Soler et al. (2008) reported them to occur only in columns with Fe(III)-Cl-H^+ solutions and not in Fe(III)-SO_4-H^+ solutions. The authors argued that in the sulfate solutions the strong attachment of gypsum onto calcite surfaces could prevent the reactivations. However, temporary passivation and reactivation has now been observed in sulfate solutions. Removal of fine grained precipitates from calcite surfaces could be the mechanism causing these reactivations.

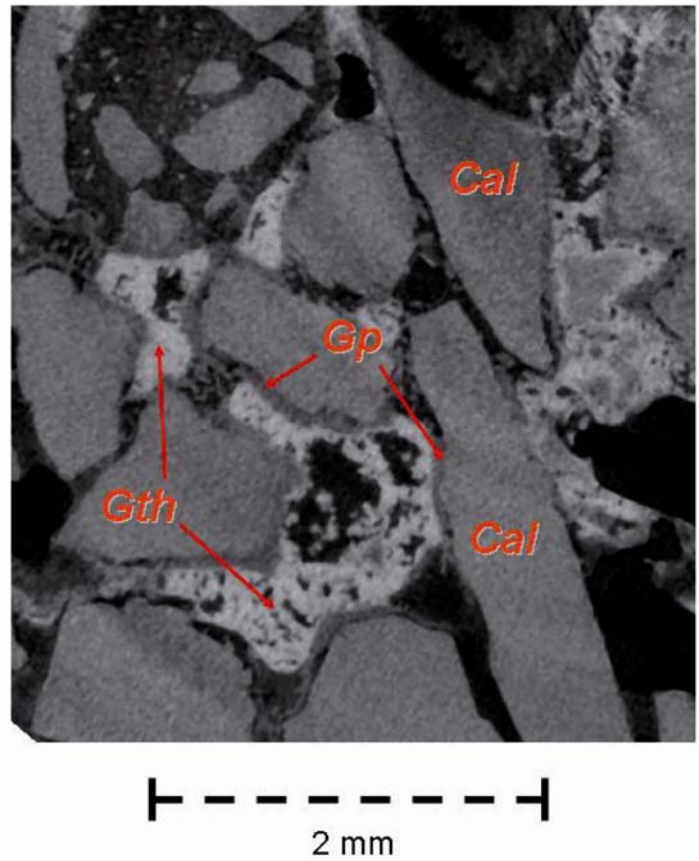

Figure 2.5 *mCT image of Column H after passivation that shows calcite grains (Cal) coated by gypsum (Gp, dark gray layer surrounding calcite surfaces). Precipitation of goethite (Gth, whitish phases) happens between grains and becomes the main responsible for decrease in porosity. Dark areas are pores.*

Figures 2.4b and 2.4d show the amount of metal retained (calculated as the product between input metal concentration in mg L^{-1}, flow rate in L h^{-1} and t_{pass} in h), normalized to the initial mass of calcite, vs. sulfate concentration of the input solution. The figures show no clear trend. Results plotting on the left correspond to experiments with small input sulfate concentrations which gave large t_{pass} values. Results plotting on the right correspond to experiments with larger input concentration which gave lower

t_{pass} values (Figs. 2.4a and 2.4c). This opposite distribution of input concentrations and t_{pass} can explain the lack of a trend in metal retention versus input concentration.

mCT examinations of column experiment H allowed detailed identification of the mineralogical and porosity changes (Fig. 2.5). mCT examinations were performed at different times (Fig. 2.6, Table 2.2): before injection (d0) and after 4, 8 and 12 days. The four mCT images in Fig. 2.6 show the same section close to the column inlet. Slight variations in the position of the grains with time were due to sample compaction during the experiment. Initially only calcite grains were present (light gray), separated from each other by pore space (dark areas).

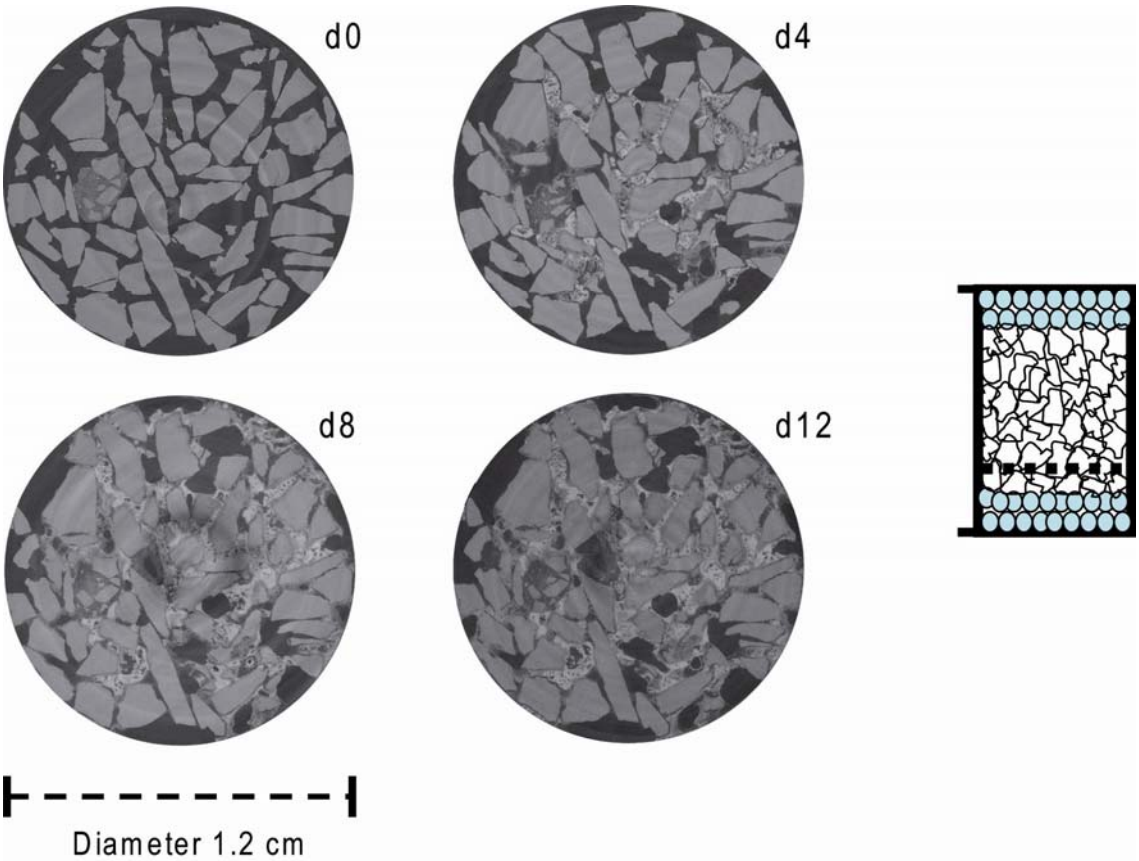

Figure 2.6 *Four mCT images of the same section (see arrow) of Column H (Table 2.2) during the experiment: d0, before reaction; d4, d8 and d12, after 4, 8 and 12 days (passivation at ≈ 300 h). As the grains were not cemented, relative positions change slightly in the 4 images.*

After ~ 90 h (d4) some of the calcite grains were coated by a thin gypsum layer (dark gray) and a whitish phase (goethite) was filling the pore space. Both gypsum and goethite were identified by mXRD. At d(8) and d(12) the gypsum coatings grew and goethite content increased. After 12 days the column was passivated and the experiment was finished. Other mCT sections along the passivated column showed that in some

portions of the column calcite grains did not react with the solution (Fig. 2.7). At the inlet (bottom) of the column a noticeable presence of goethite filling the pore space and gypsum coatings on grain surfaces is observed. In the lower middle image (LM) approximately 75 % of the grains reacted, leaving some non-reacted grains visible on the left side. In the upper middle section (UM) the fraction of reacted grains diminished and at the top only ~50% reacted: A clear separation between reacted and non-reacted regions is readily observed. Formation of preferential paths in the columns was observed in most of the experiments and was more evident in the upper parts of the columns (closer to the outlet).

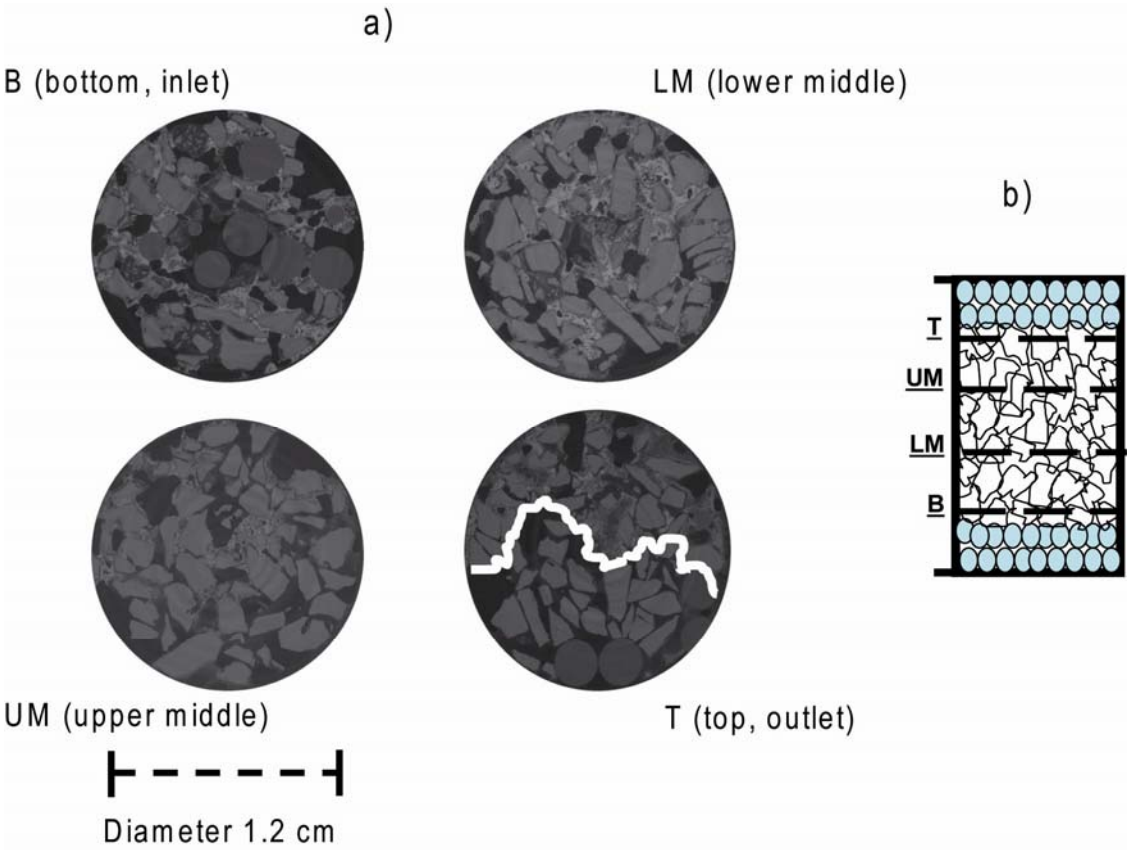

Figure 2.7 *(a) mCT images of four sections from Column H after passivation (≈ 300 h) that show the distribution of precipitates along the column. The solid line in the top section separates a reacted from a non-reacted zone. Glass beads are visible at the bottom and top sections of the column. (b) Scheme showing the location of the sections along the column.*

2.3.4 Porosity variation

The mCT images showed that precipitation of Me-oxyhydroxides and gypsum caused a decrease in porosity. Once the injected solution reacted with the calcite grains, a

reaction front advanced upwards. Figure 2.8 shows the porosity variation with time along column H.

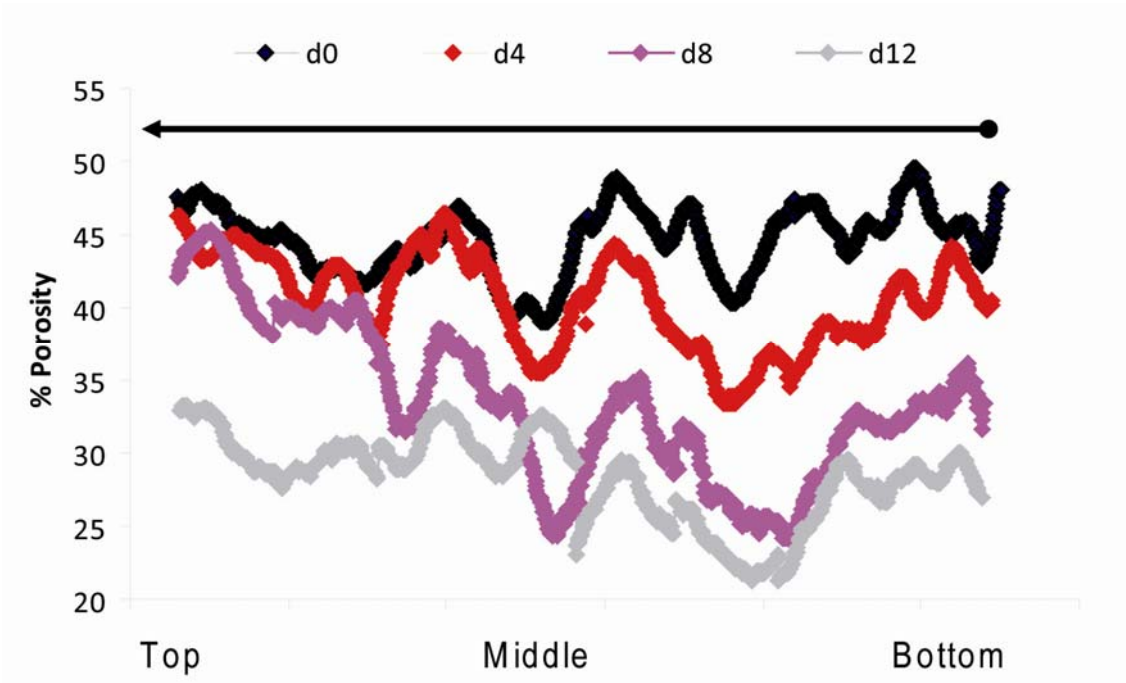

Figure 2.8 *Porosity variation with time along column H. The arrow indicates the flux direction. d0, d4, d8 and d12 stand for measurements at 0, 4, 8 and 12 days, respectively. Porosity decreases from an initial value of 48 ± 2 % to 31 ± 2 %.*

The black and grey lines represent initial and final porosity, respectively. The two lines in between correspond to the porosity along the column at 4 and 8 days. The lines represent the pore-space area per section area (%) with an error of 2% (the sum of calcite, porosity and precipitates areas ranged from 98% to 102 %). It is inferred that the initial porosity fluctuates along the column within a difference of ± 5% with respect to the mean porosity value (45%) because grain distribution varies along the column. After 4 days of constant injection, a porosity decrease occurs only in the low middle part of the column. After 8 days, a porosity decrease is more evident in the low middle part, although a slight decrease is already observable in the upper part. Thereafter, until full passivation (12 days; grey line), porosity decreases all along the column, being still more evident in the lower middle part (25 %) than in the upper middle part (10 %). The final average porosity along the column is 31 %.

Formation of preferential flow paths, especially in the upper part of the column (Fig. 2.7), caused isolation of some portions where calcite grains did not react, limiting the barrier efficiency.

The contribution of gypsum and goethite precipitates to porosity decrease was calculated using the mCT image segmentation method (Fig. 2.9). After 12 days, precipitation of goethite and gypsum contributed, respectively, ~ 15% and ~ 5% of porosity decrease from the inlet to the middle of the column. In the upper half, contributions of each phase diminished to 5 to 10 % and 1 to 2 %, respectively (Fig. 2.9). Variation with time of each phase shows that the reaction front progressed upwards, indicating that precipitation of goethite and gypsum was simultaneous (driven by calcite dissolution) and initiated at the inlet where precipitates were more abundant.

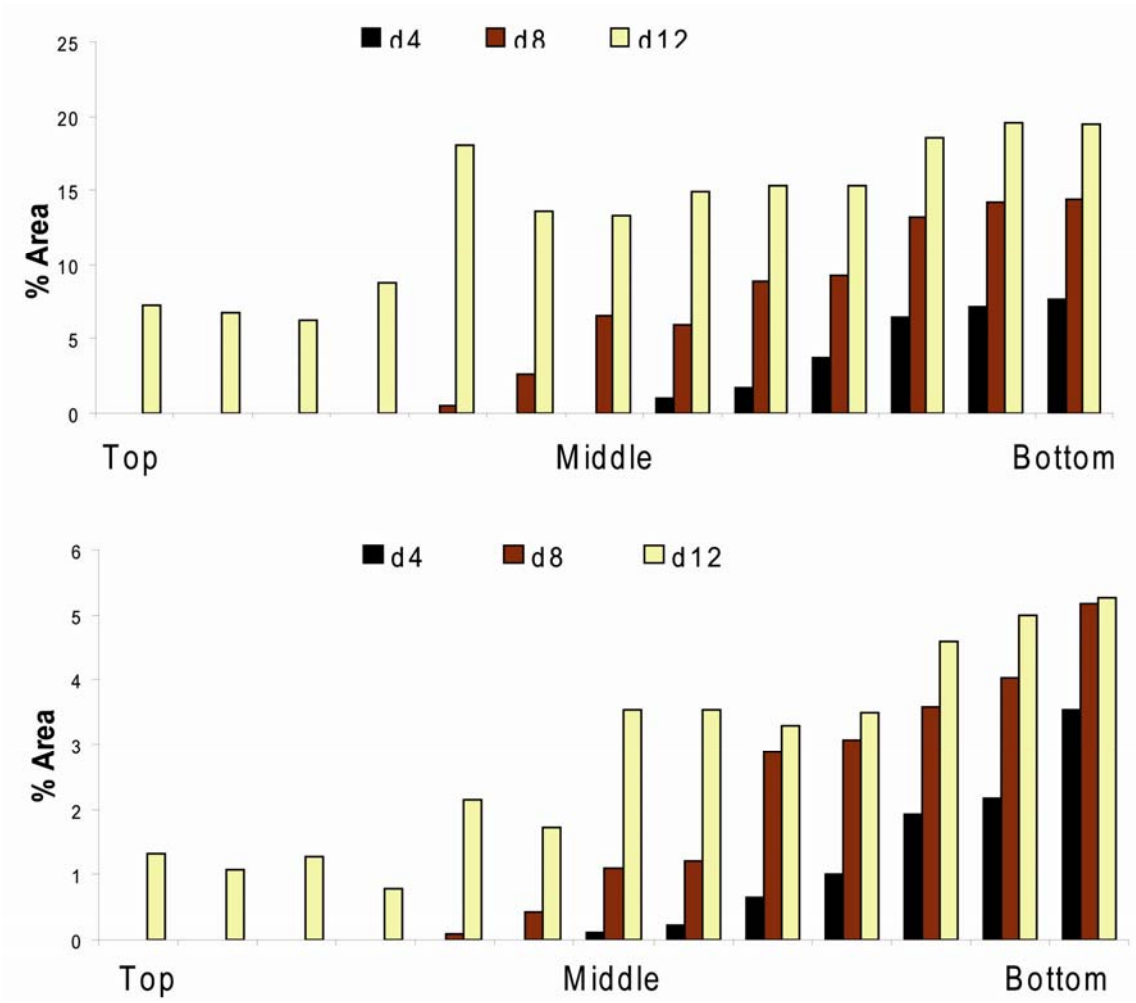

Figure2.9 *Contributions of goethite (a) and gypsum (b) to porosity variation in column H. They were calculated by segmentation of the mCT images taken after 4, 8 and 12 days. After passivation, the average gypsum content is about 3% and that of goethite is ca. 14 %. Consistent with the formation of preferential flow paths, the amount of precipitates decreases from the bottom (inlet) to the top (outlet).*

In order to avoid preferential flow paths, two longer columns (6 cm of length and 2.6 cm in diameter) packed with a homogeneous mixture of glass beads (2 mm in diameter; 67 wt %) and calcite grains (1-2 mm; 33 wt %) were run in an iron-rich solution (Table 2.2). Use of glass beads improves solution circulation through the column. Variation of the output pH and output Fe, SO_4 and Ca concentrations is shown in Fig. 2.10. It is observed that full column passivation (output pH drop to initial value and iron increase) was achieved after a longer time compared to that in calcite filled columns (e.g. see Fig 2.4).

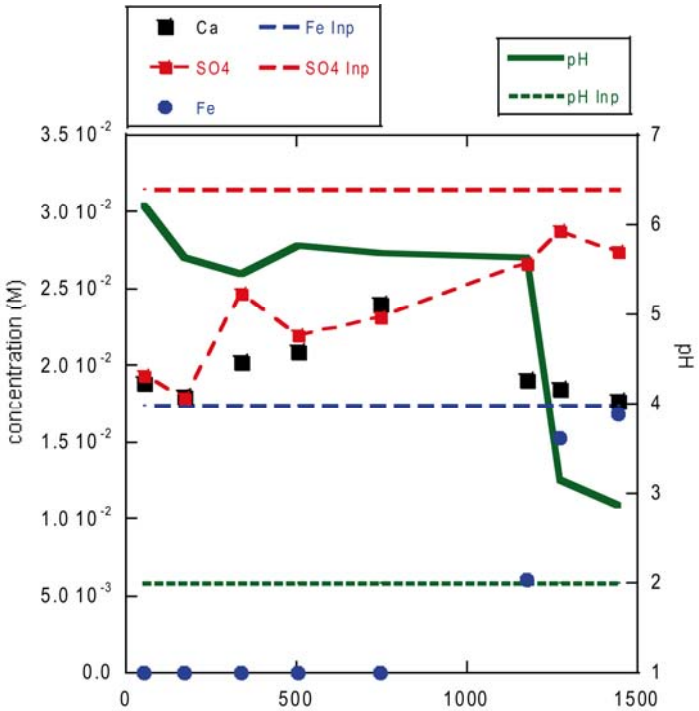

Figure 2.10 *Variation of the output concentrations of Ca, SO_4 and Fe and pH with time in experiment LCAL 1mix.*

The mCT images show regular distribution of calcite grains and beads along the columns (Fig. 2.11). In fact, formation of preferential flow paths was significantly prevented (only a little unreacted region was observed; Fig. 2.11). Duration of the bead-filled experiments was longer before full passivation was achieved and reproducibility was improved (Table 2.2 and Figs. 2.4a and b). The longer period of activity originated a larger and homogenous porosity decrease along the column (Fig. 2.12). Overall, using this column design, the performance of the system was improved. This result is in accordance with those reported by Caraballo et al. (2011) and Rötting et al. (2005, 2008), who showed that addition of inert material in the limestone treatment systems enhances the efficiency of the systems.

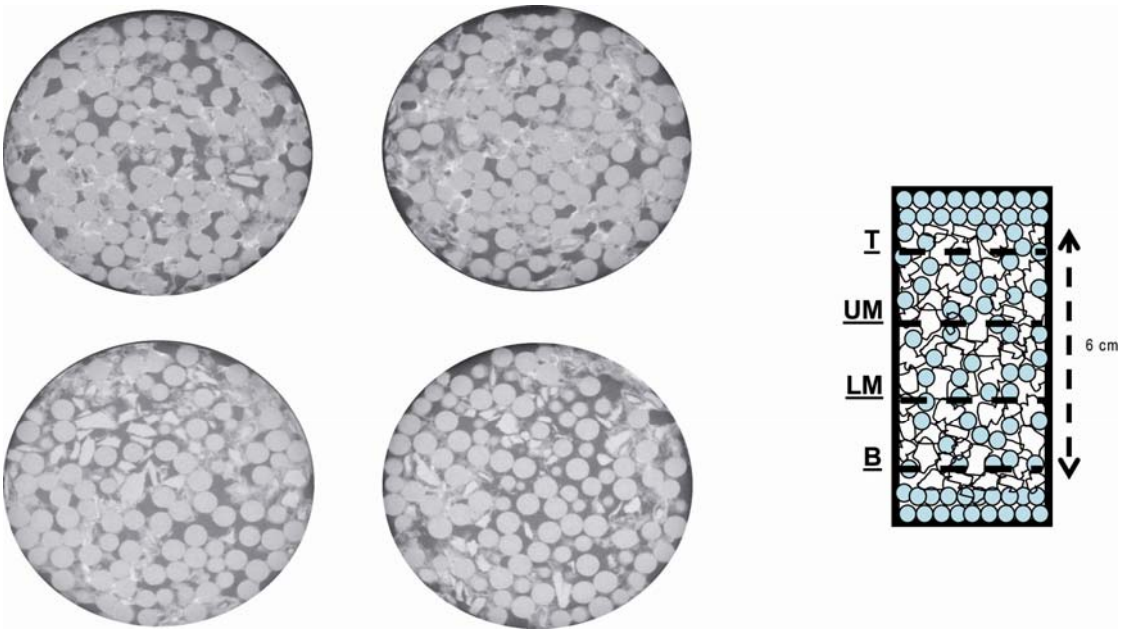

Figure 2.11 *mCT images of four sections from column LCAL1-mix after passivation. The distribution of precipitates is homogeneous with no preferential flow paths. The whitish particles between grains and beads are goethite. The final mean porosity is 16 ± 3%.*

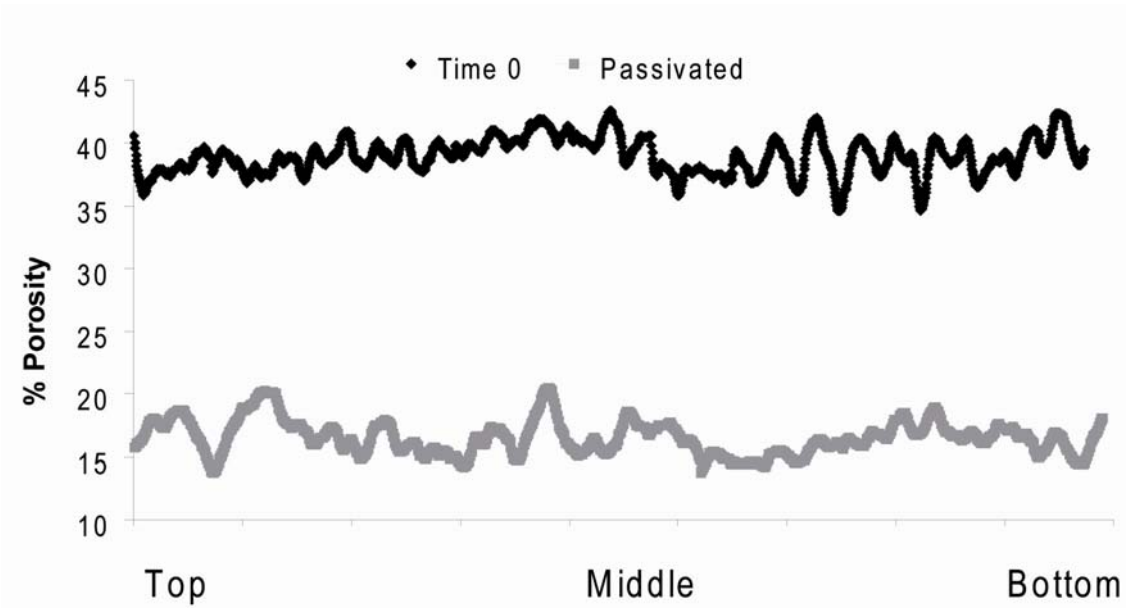

Figure 2.12 *Porosity variation along Column LCAL-1. The upper line is the distribution of porosity along the column (39 ±3 %) before the experiment start. The lower line is the final porosity after passivation (16±3 %, passivation time was ~ 50 days). The homogenous distribution of porosity along the column suggests that no preferential flow paths were formed, yielding a constant porosity decrease.*

2.3.5 Reactive transport modeling of the columns

2.3.5.1 Model parameters

Model parameters correspond to those of column experiment H. The length of the one-dimensional domain was 1.2 cm (the length of the column). Grid spacing was 0.6 mm. Calcite was the only initial mineral, and the secondary minerals that were taken into account were goethite and gypsum (Table 2.3). Initial porosity of the column and initial volume fraction of calcite were 0.494 and 0.506, respectively. The initial surface area of calcite (20 m^2 m^{-3}) was adjusted to fit the model to the experimental results. It has to be noted that this area is much smaller than either the geometric surface area of the limestone assuming spherical grains (ca. 2000 m^2 m^{-3}) or the area calculated from the BET measurements (ca. $6x10^5$ m^2 m^{-3}). An explanation for the small value could be given by the transport (diffusion) control of the net dissolution reactions under acidic pH (e.g. Sjöberg and Rickard, 1984). The resulting small net dissolution rates are implemented in the model through a small surface area term (see eq. 2.3). Goethite and gypsum surface areas were also adjusted to reproduce the observed experimental data (Table 2.3). The composition of the injected water (input solution) was the same as the experimental composition of the input solution ($1.74x10^{-2}$ mol L^{-1} of Fe(III), $3.11x10^{-2}$ mol L^{-1} of SO_4 and pH 2). The composition of the initial water in the column was at equilibrium with calcite and atmospheric CO_2 (Table 2.3). The dispersivity was considered to be equal to grid spacing. Darcy velocity was calculated from the constant flow rate used in the experiments (Table 2.3).

Table 2.3 Parameters used in the reactive transport calculations.

minerals	reactive surface area (m^2 mineral/m^3 rock)	vol. fraction
calcite	20	0.506
gypsum	10	0
goethite	0.1	0
input water	(mol/kg)	
Ca^{2+}	1.00E-09	
Fe^{3+}	1.74E-02	
HCO^-_3	1.29E-05	
SO^{2-}_4	3.11E-02	
pH	2.00	
initial rock water	(mol/kg)	
Ca^{2+}	5.32E-04	
Fe^{3+}	1.00E-19	
HCO^-_3	1.06E-03	
SO^{2-}_4	1.00E-09	
pH	8.22	
effective diffusion coefficient De (m^2/sec)	5.00E-10	
dispersivity a (m)	1.30E-03	
Darcy velocity m^3/m^2/sec	1.03E-06	
nodes	20	

Three minerals and 23 species in solution were taken into account in the calculations. The equilibrium constants for the three mineral reactions are given in Table 2.4.

Table 2.4 *Equilibrium constants for the mineral reactions considered in the calculations*

	$\log K_{T=25^aC}$	
Calcite	1.8480	$CaCO_3 + H^+ \leftrightarrow Ca^{2+} + HCO_3^-$
Gypsum	-4.4820	$CaSO_4 \cdot 2H_2O + 3H^+ \leftrightarrow Ca^{2+} + SO_4^{2-} + 2H_2O$
Goethite	0.5345	$FeO \cdot OH + 3H^+ \leftrightarrow Fe^{3+} + 2H_2O$

All the chemical equilibria in solution are listed in Table 2.5 All the equilibrium constants at 25 °C were taken from the database included in CrunchFlow, which is based on the EQ3/6 database (Wolery et al. 1990). The kinetic rate laws used in the present study were obtained from (Palandri and Kharaka, 2004). Rate parameters for the minerals considered in the calculations are shown in Table 2.6.

Table 2.5 ***Equilibria in solution considered in the calculations.***

$\log K_{25°C}$	reactions
-6.3447	$CO_{2(aq)} + H_2O \leftrightarrow HCO_3^- + H^+$
10.3288	$CO_3^{2-} + H_+ \leftrightarrow HCO_3^-$
7.0017	$CaCO_3 + H+ \leftrightarrow Ca^{2+} + HCO^-{}_3 + H_2O$
-1.0467	$CaHCO_3^- \leftrightarrow Ca^{2+} + HCO_3^- + H_2O$
12.85	$CaOH^+ + H^+ \leftrightarrow Ca^{2+} + H_2O$
-2.111	$CaSO_{4(aq)} \leftrightarrow Ca^{2+} + SO_4^{2-} + H_2O$
5.67	$Fe(OH)_2^+ + 2H^+ \leftrightarrow Fe^{3+} + 2H_2O$
12	$Fe(OH)_{3(aq)} + 3H^+ \leftrightarrow Fe^{3+} + 3H_2O$
21.6	$Fe(OH)_4^-{}_{(aq)} + 4H^+ \leftrightarrow Fe^{3+} + 4H_2O$
-3.2127	$Fe(SO_4)^{2-} \leftrightarrow Fe^{3+} + 2SO_4^{2-}$
2.95	$Fe_2(OH)_2^{4+} + 2H^+ \leftrightarrow 2Fe^{3+} + 2H_2O$
6.3	$Fe_3(OH)_4^{5+} + 4H^+ \leftrightarrow 3Fe^{3+} + 4H_2O$
0.6088	$FeCO_3^+ + H^+ \leftrightarrow Fe^{3+} + HCO3^-$
9.5	$FeOH^{2+} + H^+ \leftrightarrow Fe^{3+} + H_2O$
-1.9276	$FeSO_4^+ \leftrightarrow Fe^{3+} + SO_4^{2-}$
1.0209	$H_2SO_{4(aq)} \leftrightarrow SO_4^{2-} + 2H^+$
-1.9791	$HSO_4^- \leftrightarrow SO_4^{2-} + H^+$

Table 3.6 *Kinetic parameters in the mineral dissolution/precipitation rate laws (25ºC) (Palandri and Kharaka, 2004).*

mineral	$k_{m,25}$[mol $m^{-2}s^{-1}$]	n(aH+n)
calcite	5.01E-01	1
	1.55E-06	-
goethite	1.15E-08	-
gypsum	1.62E-03	-

2.3.5.2 Results

As passivation is controlled by gypsum coating on calcite surfaces, calcite reactivity should diminish as a consequence of the loss of calcite reactive surface area. The initial calcite surface area was adjusted to 20 m^2 mineral m^{-3} rock. The initial surface area for gypsum and goethite were also fitted to the initial experimental results. During the course of the simulation, the calcite surface area was decreased stepwise at two different times. After 230 h, the value was reduced to 10 m^2/m^3; after 300 h it was reduced to 0.1 m^2/m^3 (Fig. 2.13).

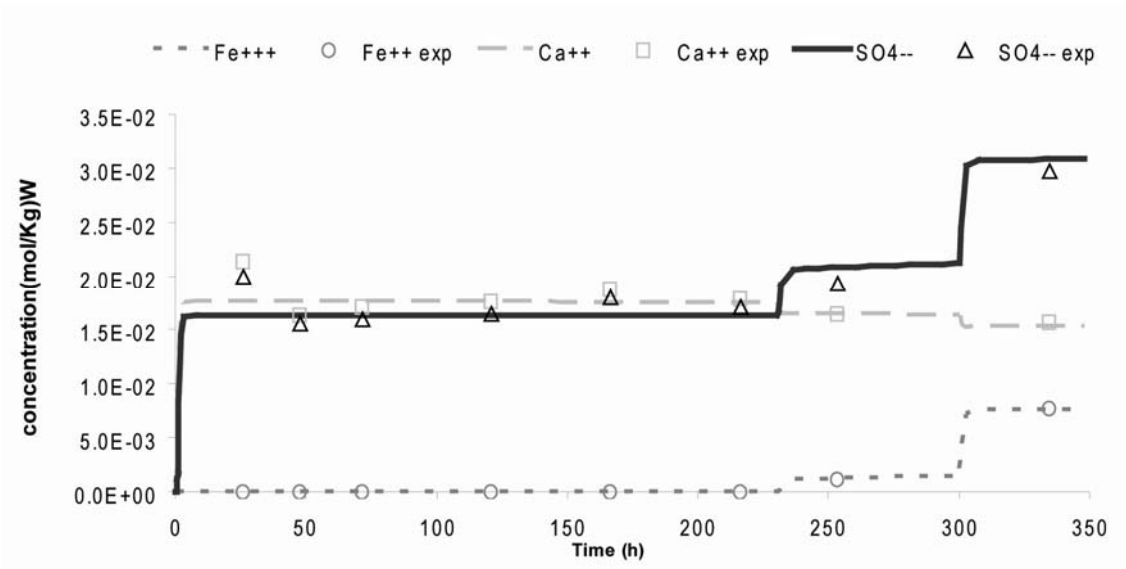

Figure 2.13 ***Experimental and modeling results (output concentrations vs. time) from column H.***

The reactive surface areas of goethite and gypsum were assumed constant during the experiment. This is a model simplification, since areas should increase with

precipitation. But even with this underestimation of gypsum and goethite reactivity it was necessary to reduce the calcite surface area to match the experimental results (smaller Ca concentrations due to less dissolution of calcite and larger SO_4 and Fe concentrations due to less precipitation of secondary gypsum and goethite). This simple model (stepwise reduction of calcite surface area) shows that the experimental results are consistent with a reduction of calcite reactivity induced by the precipitation of gypsum.

2.4 Summary and conclusions

Factors affecting the efficiency of limestone in passive treatment systems for AMD were studied using centimetric-scale columns packed with crushed limestone. In these systems, calcite passivation by gypsum coating is an important limitation to the limestone buffer capacity, and the main factors for controlling passivation time were the initial sulfate concentration and pH. A decrease in sulfate concentration and the use of low flow rate enhance the column passivation time. In those experiments run with higher pH passivation time also improved.

Metal retention does not show the same trends as passivation time: there is little sensitivity of metal retained on initial sulfate (and metal) concentration due to the negative correlation between initial concentration and passivation time.

Another limitation for the treatment efficiency is the formation of preferential flow paths and column clogging. These complementary phenomena are caused by the precipitation of iron or aluminum oxyhydroxides which impede homogeneous circulation of the solutions through the columns. To improve the efficiency in the passive treatment, mixtures of calcite grains and glass beads were used to pack the columns. The addition of an inert substrate clearly improves the efficiency.

mCT images and mXRD measurements were used to determine how gypsum coating and metal-oxyhydroxide precipitation occurred and to quantify porosity variation along the columns. It was observed that porosity decreased progressively with time. Gypsum coating contributed 5 % in porosity reduction, whereas goethite contribution was ~15%.

Gypsum and goethite precipitation was simultaneous.

A good match between experimental results and reactive transport simulations was achieved. Fitting of the results required a reduction in the reactive surface area of calcite with time, which is consistent with a passivation mechanism (formation of gypsum coatings on calcite surfaces).

Chapter 3

Comparison between the efficiency of aragonite and dolostone with that of limestone in passive treatments for AMD: column experiments

3.1 Introduction

This chapter presents the comparison between the efficiency of the columns filled with aragonite and dolostone with those filled with limestone, shown in Chapter 2, under atmospheric pressure and 25 ºC, using H_2SO_4 solutions of pH 2 and different concentrations of Fe(III), Al and sulfate. Likewise, to decipher how secondary phases precipitate and influence the porosity changes, several X-ray microtomography (mCT) measurements were carried out before and during the experiments.

3.2 Materials and methods

3.2.1 Sample preparation and characterization

Aragonite was obtained from the shell of commercially available common cockle, *Cerastoderma edule*. Shells were immersed in 0.5 M NaOH solution for a week and cleaned with a brush to eliminate possible films of organic matter usually adhered on the surfaces. Thereafter, shells were crushed and sieved to obtain a grain fraction of 1-2 mm in size. Residual microparticles on selected grains were removed using an ultrasonic bath in anhydrous ethanol for 15 min. XRD analysis showed only aragonite

peaks (Fig. 3.1a). Dolostone samples were obtained from a Triassic dolostone formation in the Corbera area (Barcelona). Samples were crushed and sieved to obtain a grain size of 1-2 mm. To remove microparticles, grains were pre-washed with MilliQ water several times until clear output water was collected. Thereafter, grains were dried at 50 ºC for 24 h. XRD patterns of the dolostone sample showed only dolomite peaks (Fig. 3.1b).

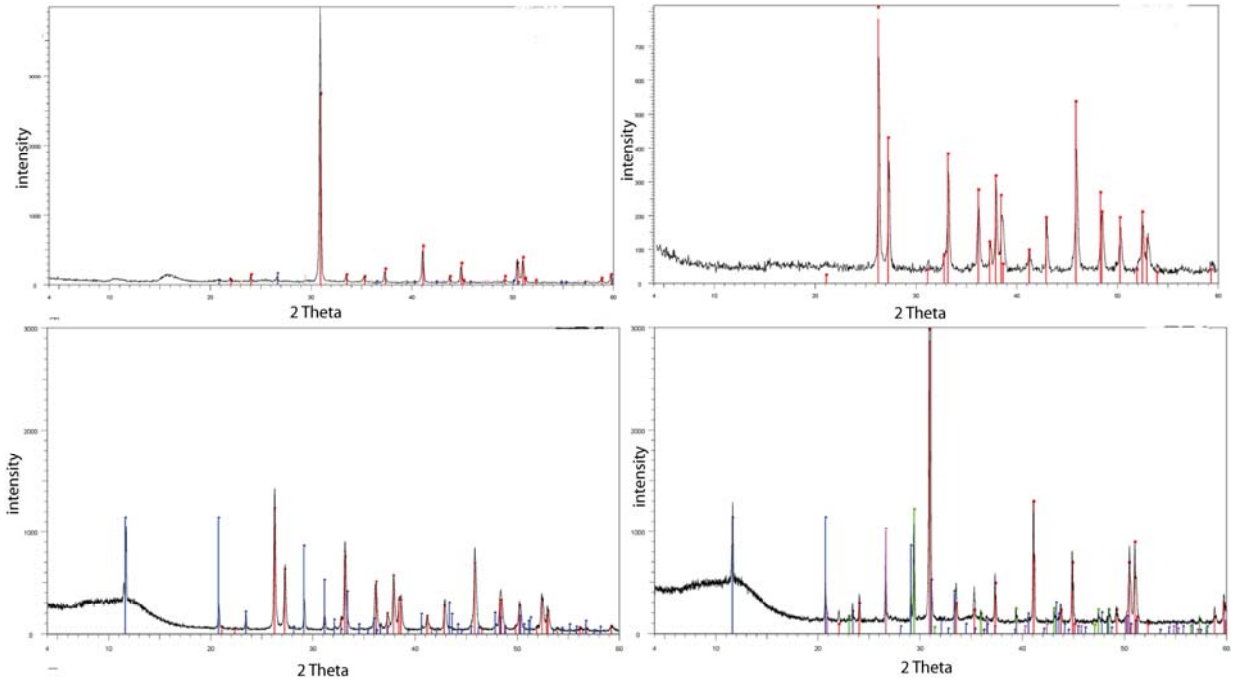

Figure 3.1 *XRD patterns of the aragonite sample (a), dolostone sample (b) (showing only dolomite peaks), aragonite-Al-column sample(c) and dolomite-Fe-column sample (d).*

3.2.2 Column experiments

Cylindrical columns, similar to those described in Chapter 2, were made from transparent polymethyl methacrylate with inner diameters and lengths which ranged from 1.2 to 2.6 cm and from 1.1 to 6 cm, respectively (Tables 3.1 and 3.2). Likewise, column characteristics and experimental setup were the same as those detailed in Chapter 2. However, in this part of the study a larger number of experiments with columns 6 cm long and 2.6 cm in diameter, mixed with glass beads, were performed.

Column porosities were calculated from the known masses of aragonite and dolostone, volumes of the column and densities of aragonite and dolomite (2.93 and 2.84 g cm^{-3}, respectively) and also from the acquired mCT images of the columns using the gray-scale segmentation method. The initial porosities, based on density calculations and mCT measurements, ranged from 35 to 59 % (Tables 3.1 and 3.2).

Table 3.1 *Experimental conditions in the aluminum-column experiments.*

column	weight mineral (g)	Al (M)	SO_4^{2-} (M)	column lenght (cm)	column diameter (cm)	porosity (%)	tpass/τ	time (h)	$mg_{Al}/g_{mineral}$
DOLOSTONE									
6 DOL mix	15.95	1.85E-02	3.28E-02	6	2.6	41	67	453	27
7 DOL mix	15.96	1.85E-02	3.28E-02	6	2.6	39	43	286	17
8 DOL mix	13.14	1.85E-02	3.28E-02	6	2.6	45	169	1269	92
9 DOL mix	15.89	7.41E-03	1.61E-02	6	2.6	42	177	1245	30
10 DOL mix	15.98	7.41E-03	1.61E-02	6	2.6	42	178	1245	30
12 DOL	18.98	8.11E-03	2.11E-02	2.5	2.6	55	186	797	30
11 DOL mix	14.02	3.71E-03	1.05E-02	6	2.6	44	296	2177	30
12bis DOL mix	14.03	7.41E-03	1.61E-02	6	2.6	44	351	2586	35
13 DOL mix	14	3.71E-03	1.05E-02	6	2.6	44	420	3093	42
ARAGONITE									
6 AR mix	15.75	1.85E-02	3.28E-02	6	2.6	42	90	622	38
7 AR mix	15.74	1.85E-02	3.28E-02	6	2.6	43	33	237	14
8 AR mix	16.08	1.85E-02	3.28E-02	6	2.6	42	179	1269	75
9 AR mix	12.45	7.41E-03	1.61E-02	6	2.6	46	186	1437	44
13bis AR	18.98	8.00E-03	2.00E-02	3	2.6	55	104	416	9
10 AR mix	14.76	7.41E-03	1.61E-02	6	2.6	44	223	1632	42
11 AR mix	14.01	3.71E-03	1.05E-02	6	2.6	45	406	3018	41
12 AR mix	14.01	3.71E-03	1.05E-02	6	2.6	45	155	1154	16
13 AR mix	14.01	3.71E-03	1.05E-02	6	2.6	45	432	3213	44

All column experiments were run at $1x10^{-3}$ L m^{-2} s^{-1} and initial pH of 2 and were passivated.
t_{pass} denotes time in hours needed to passivate the column.
τ denotes residence time calculated as V/Q.
t_{pass}/τ denotes passivation time normalized with respect to residence time.
$mg_{Al}/g_{mineral}$ denotes amount of aluminum retained by mineral (dolomite and aragonite).
"mix" indicates columns filled with mineral and glass beads.
Porosity calculated from mineral mass and density.

Table 3.2 *Experimental conditions in the iron-column experiments.*

column	weight mineral (g)	Fe (M)	SO_4^{2-} (M)	column lenght (cm)	column diameter (cm)	porosity (%)	t_{pass}/τ	time (h)	$mg_{Fe}/g_{mineral}$	Passivated
DOLOSTONE										
2 DOL	2.02	1.79E-02	3.18E-02	1.2	1.2	48	86	136	27	YES
3 DOL	2.08	1.79E-02	3.18E-02	1.2	1.2	46	198	305	60	YES
4 DOL	15.97	1.79E-02	3.18E-02	1.7	2.6	35	185	303	36	YES
1 DOL	1.90	8.95E-03	1.84E-02	1.2	1.2	48	221	356	38	YES
14 DOL	19.02	8.95E-03	1.84E-02	3.0	2.6	58	138	667	34	YES
5 DOL	14.95	8.95E-03	1.84E-02	1.8	2.6	42	188	398	25	CLOG.
5A	1.96	3.58E-03	1.04E-02	1.2	1.2	49	658	1077	45	YES
6A	1.86	3.58E-03	1.04E-02	1.2	1.2	52	593	1023	45	YES
8A	2.04	3.58E-03	1.04E-02	1.2	1.2	47	580	910	36	YES
mCT DOL 1	14.05	1.79E-02	3.18E-02	1.8	2.6	43	120	242	36	YES
mCT DOL 2	1.62	1.79E-02	3.18E-02	1.2	1.2	45	68	121	31	YES
mCT DOL 3 mix	14.00	1.79E-02	3.18E-02	6	2.6	40	-	-	-	NO PASS
ARAGONITE										
2 AR	1.62	1.79E-02	3.18E-02	1.1	1.2	56	80	136	34	YES
3 AR	1.59	1.79E-02	3.18E-02	1.1	1.2	56	79	136	35	YES
4 AR	13.43	1.79E-02	3.18E-02	1.7	2.6	49	130	303	43	YES
1 AR	1.62	8.95E-03	1.84E-02	1.1	1.2	56	397	675	85	YES
5 AR	14.45	8.95E-03	1.84E-02	1.8	2.6	48	911	2204	146	YES
15 AR	17.37	8.95E-03	1.84E-02	2.7	2.6	59	247	1085	60	CLOG.
3A	1.81	3.58E-03	1.04E-02	1.2	1.2	54	1661	3017	136	CLOG.
4A	1.50	3.58E-03	1.04E-02	1.1	1.2	59	986	1773	96	CLOG.
9A	1.70	3.58E-03	1.04E-02	1.2	1.2	57	782	1492	71	CLOG.
mCT AR 1	14.12	1.79E-02	3.18E-02	1.8	2.6	39	54	122	18	YES
mCT AR 2	1.64	1.79E-02	3.18E-02	1.2	1.2	44	38	72	18	YES
mCT AR 3 mix	13.08	1.79E-02	3.18E-02	6	2.6	37	-	-	-	NO PASS

All column experiments run at 1x10-3 L m-2 s-1 and initial pH of 2.
t_{pass} denotes time in hours needed to passivate the column.
τ denotes residence time calculated as V/Q.
t_{pass}/τ denotes passivation time normalized with respect to residence time.
$mg_{Fe}/g_{mineral}$ denotes amount of iron retained by mineral (dolomite and aragonite).
"mix" indicates column filled with mineral and glass beads.
mCT indicates columns scanned by X-ray microtomography.
Porosity calculated from mineral mass and density except for "mCT" experiments where it was measured by microtomography.

Input solutions were injected from the column bottom upwards by a Gilson peristaltic pump under constant flow rate, yielding a flux of $1x10^{-3}$ L m^{-2} s^{-1}. Residence time (τ) ranged from 1.6 to 7 h. The experiments carried out for mCT measurements were temporarily stopped at different times to acquire mCT images before the experiments (d0) and after 3, 4, 5, 7, 8 and 11 days (d3, d4, d5, d7, d8, and d11). After each image acquisition the experiments were restarted again. During mCT measurements, columns with size of 1.2x1.2 cm and 2.6x2.6 cm were passivated. In the 2.6x6 cm columns, passivation was not achieved. All experiments were repeated at least 3 times to check their reproducibility.

3.2.3 Solutions

Input solutions were made from adequate amounts of $Fe_2(SO_4)_3{\cdot}5H_2O$ and $Al_2(SO_4)_3{\cdot}16H_2O$ reagents (pro analysis grade) and Millipore MQ water (18 MΩ cm). The solutions (H_2SO_4) had initial concentrations of Fe(III) ranging from $3.58x10^{-3}$ to $1.79x10^{-2}$ mol L^{-1} and of Al ranging from $3.73x10^{-3}$ to $1.85x10^{-2}$ mol L^{-1}. Sulfate concentrations ranged from $1.00x10^{-2}$ to $3.20x10^{-2}$ mol L^{-1} for iron columns and from $1.05x10^{-2}$ to $3.28x10^{-2}$ mol L^{-1} for aluminum columns. In all experiments solution pH was 2, which was adjusted by adding concentrated H_2SO_4 to the iron sulfate and aluminum sulfate solutions (Tables 3.1 and 3.2).

3.2.4 Analytical methods

Input and output concentrations of Fe, Al, S, Mg, Ca, Na and Si were measured by Inductively Coupled Plasma - Atomic Emission Spectrometry (ICP-AES), using a Thermo-Jarrel Ash spectrometer equipped with a CID detector. The detection limits for Fe, S, Mg, Ca, Al and Si were 1.8×10^{-7}, 3.5×10^{-6}, 10^{-5}, 5×10^{-6}, 7.5×10^{-7} and 7×10^{-7} mol L^{-1}, respectively. The error associated with ICP-AES measurement was estimated to be around 3%, based on measurement of different standard solutions in the calibration process. The solution pH was measured during the experiments with a Thermo Electron Orion 720 A+ pH meter at room temperature (22 ± 2 ºC) with an error of ± 0.02 pH units. The electrode was regularly calibrated with buffer solutions at pH 2 and 7. The output solution pH was continuously measured by placing the electrode in a sealed tube in which the output solution circulated (see Fig. 2.1a in Chapter 2). The

saturation indexes for dolomite, aragonite and gypsum were calculated at 25 °C using the PHREEQC code (Parkhurst, 1995) and MINTEQ database (Allison et al., 1991).
XRD patterns of the solid samples (before and after the experiments) were measured with a Bruker D-5005 diffractometer, using Cu K-α1 radiation (λ = 1.5406 Å) at 40 kV and 30 mA, 2θ scanning range from 4° to 60°, and a scan step and step duration of 0.05° and 3 s.

X-ray microtomography (mCT) images were taken at the National Institute for Lasers, Plasma and Radiation Physics (NILPRP, Bucharest-Magurele, Romania). The mCT equipment was described in Chapter 2. All mCT images were taken before and during the experiments at regular time intervals. The segmentation method (separation of gray-scale range values) was applied to quantify porosity using the ImageJ software (Schneider et al., 2012). Since acquirement of mCT images is based on the different density of the materials, and the density of Al-hydroxides is very low, it was impossible to obtain mCT images of the Al-compounds in the aluminum columns. Hence, only the mCT images in some of the iron columns were used to characterize the mineral variation with time at different time intervals. Time to capture the mCT images was ~ 2 h. In the mCT images each mineral (dolomite, aragonite, Fe-oxyhydroxides, gypsum, glass beads) has a different gray color according to its density and composition (X-ray absorption coefficient). The pore space is black.

3.3 Results and Discussion

Tables 3.1 and 3.2 show the experimental conditions of the aluminum and iron column experiments, respectively. The experiments lasted from 72 to 3213 h depending on their geochemical evolution.

In the columns filled with dolostone or aragonite run with iron-rich or aluminum-rich input solutions the following steps were observed: (1) dissolution of the carbonate minerals once the acidic solution entered into the column; (2) pH increase up to ≈ 5-7 and precipitation of metal hydroxides with consequent aqueous metal depletion; (3) supersaturation with respect to gypsum and gypsum precipitation on the surface of the carbonate grains and gypsum coating preventing carbonate dissolution to lead to column

passivation. Like in the limestone-filled columns (Chapter 2), the time required to reach passivation (passivation time, t_{pass}), depended on the input concentration of SO_4, which correlated with metal concentration (Fe and Al were added as sulfate salts). It was considered that columns were passivated when pH remained at values near that of the input solution for 5 consecutive days.

3.3.1 Aluminum columns

Figure 3.2a,c shows variation of the output concentrations of Ca, Mg, SO_4 and Al and output pH with time in two representative Al column experiments (12 DOL (dolostone) and 13bis AR (aragonite). Input Al and sulfate concentrations were 7.41×10^{-3} mol L^{-1} and 2.00×10^{-2} mol L^{-1}, respectively, for experiment 12 DOL and 3.71×10^{-3} mol L^{-1} and 1.05×10^{-2} mol L^{-1}, respectively, for experiment 13bis AR. As the solution reacted with dolomite and aragonite, the output pH increased from 2 to pH between 4 and 6 for around 500 h and 300, respectively. During this time, when pH was ≥ ca. 5, dissolved Al was depleted. In experiment 12 DOL the concentrations of Ca and Mg raised to ~ 1.2×10^{-2} mol L^{-1} and ~ 9×10^{-3} mol L^{-1}, and the output concentration of sulfate was fairly constant at 2.0×10^{-2} mol L^{-1}. In experiment 13bis AR, the concentration of Ca raised to ~ 1.7×10^{-2} mol L^{-1}, and the output concentration of sulfate maintained circa constant value of 1.8×10^{-2} mol L^{-1} (Fig. 3.2a,c). Therefore, at this stage, the dolostone-filled and the aragonite-filled columns were acting as expected, removing Al from solution, decreasing slightly sulfate concentration and neutralizing acidity. PHREEQC calculations showed that the output solution was undersaturated with respect to dolomite and aragonite, but supersaturated with respect to Al-hydroxide (gibbsite ($Al(OH)_3$) and gypsum ($CaSO_4 \cdot 2H_2O$). Gypsum was identified by XRD (Fig. 3.1c), but not gibbsite, indicating that $CaSO_4 \cdot 2H_2O$ and likely an amorphous $Al(OH)_3$ precipitate under these conditions. After this stage the output pH and the output Ca (and Mg for experiment 12 DOL) concentration gradually decreased. pH decreased to approach a nearly constant value of ~ 4 for both aragonite and dolomite experiments. In experiment 12 DOL Ca and Mg reached concentration ~2.3×10^{-3} mol $L^{-1}$and ~1.7×10^{-3} mol L^{-1}, respectively. Dolostone, containing calcite, realize less of Mg then Ca. In experiment 13bis AR Ca reached an approximately constant concentration ~1.3×10^{-3} mol L^{-1} until the end of the experiment (Fig. 3.2a,b). The output concentrations of SO_4 and Al tended to reach the values of the input concentration. Therefore, this behavior suggests that

dissolution of dolomite and aragonite was likely prevented by gypsum precipitation on the surfaces (*armoring* or *coating* effect), diminishing the buffer capacity of the mineral carbonates.

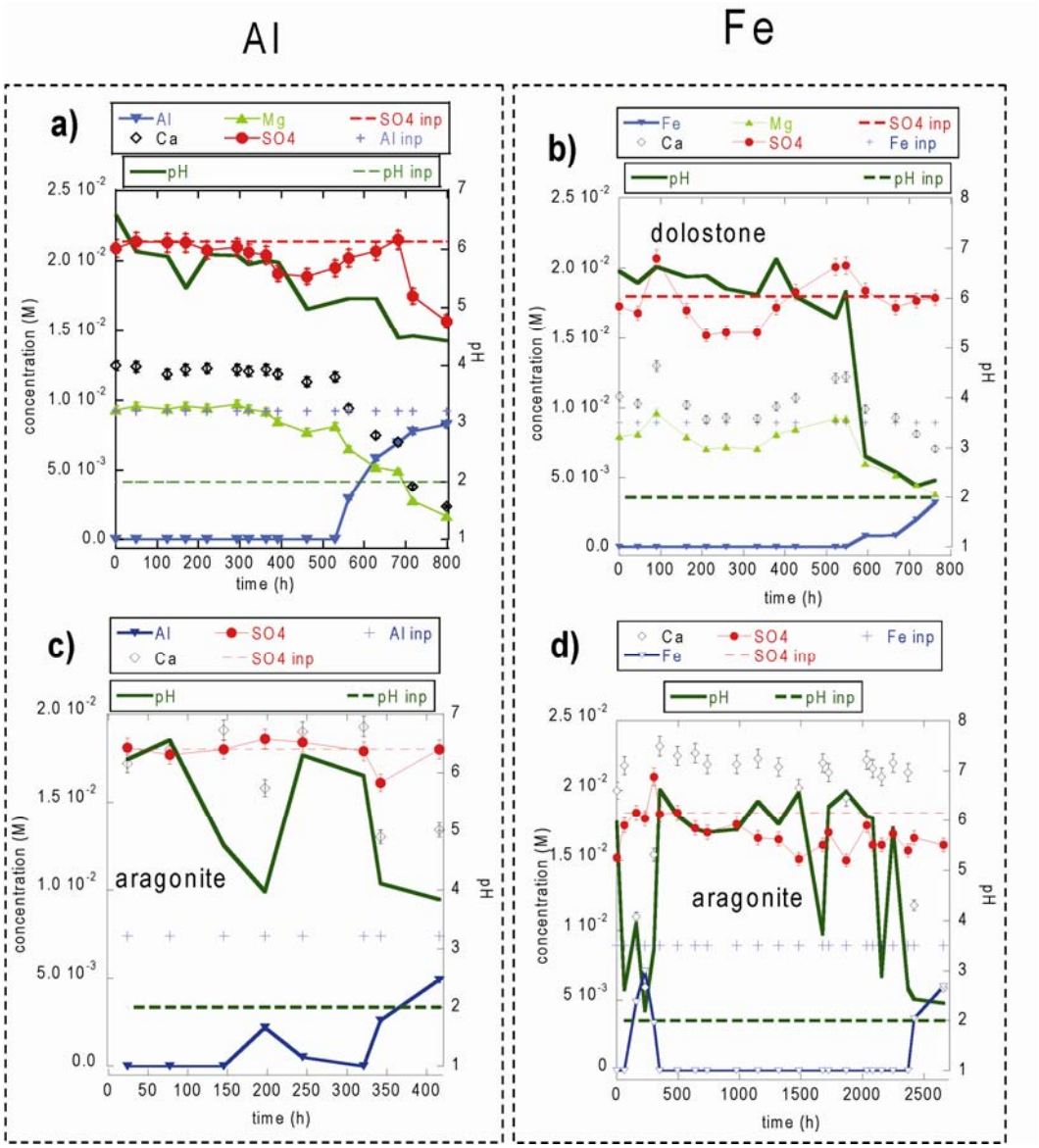

Figure 3.2 *Representative column experiments of dolostone and aragonite. Variation of output pH and output concentrations of Al, Fe, Ca, Mg and SO_4 with time in experiments 12 DOL (dolstonee) (a), 14 DOL (dolostone) (b), 13bis AR (aragonite) (c) and 15 AR (aragonite) (d).*

3.3.2 Iron columns

Figure 3.2b,d shows variation of the output concentrations of Ca, Mg, SO_4, Fe and pH as a function of time in two representative Fe column experiments (experiments 14 DOL and 15AR; Table 3.1 and Table 3.2). Overall, input pH increased to ~ 6 due to dissolution of dolomite and aragonite as shows the increase in Ca (and Mg for

dolostone): Ca and Mg ≈ 1.0 x 10^{-2} mol L^{-1} (14 DOL); Ca ≈ 2.2x10^{-2} mol L^{-1} (15 AR). While dissolution of the carbonate minerals, Fe was depleted. Although precipitation of gypsum was clearly identified (Fig. 3.1d), goethite was not detected, suggesting that amorphous $Fe(OH)_3$ likely precipitated. After ~ 600 h in 14DOL and 2200 h in 15 AR, the output pH sharply dropped to ≈ 2, the output Fe concentration started to eventually reach the initial one, and Ca concentration decreased to 5.4 x 10^{-3} mol L^{-1} (14 DOL) and 1.2 mol L^{-1} (15 AR) (Fig. 3.2c,d). This variation indicates that aragonite and dolostone were losing reactivity. Like in the limestone-filled columns, temporary passivation of dolostone and aragonite occurred during experiments (Fig. 3.2d).

3.3.3 Column Efficiency

Efficiency of the dolostone- and aragonite-filled columns to retain Fe and Al and neutralize acidity depended on the composition of the input solution and the type of carbonate mineral.

3.3.3.1 Dolostone-filled columns

Figure 3.3a,c shows plots of t_{pass} normalized to residence time τ (column length divided by initial linear velocity) vs. initial SO_4 concentration for the iron and Al experiments. Column size for iron experiments was mostly 1.2x1.2 cm, while for aluminum experiments, it was mostly 2.6x6 cm and columns were filled with glass beads and dolostone grains (70% and 30% in weight, respectively). The tendency observed in both Fe and Al columns is that t_{pass}/τ increased when decreasing the input sulfate (and metal) concentrations (Fig. 3.3a,c). This trend was already observed for the limestone-filled columns described in Chapter 2 and those performed by Soler et al. (2008). On the one hand, at low SO_4 concentrations (1.02x10^{-2} mol L^{-1}), t_{pass}/τ reached higher values in the iron column than in the aluminum ones, indicating better efficiency in the former columns. On the other hand, at high SO_4 concentration (3.0x10^{-2} molL^{-1}), t_{pass}/τ reached comparable values in both aluminum and iron column experiments.

Dolostone dissolution caused an increase in pH from 2 to ~ 5-7 (proton consumption), resulting in supersaturation of the solutions with respect to Fe- or Al-oxyhydroxides.

Clogging of the pore space, caused by precipitation of metal-oxyhydroxides between grains, was observed in only one experiment (see arrow in Fig. 3.3a,b).

Reproducibility of the results was similar in both the iron and aluminum column experiments, yielding a t_{pass}/τ variability, among the experiments run at similar input SO_4^{2-} concentration, that ranged between 100 and 120 approximately (Fig. 3.3a,c and Tables 3.1 and 3.2).

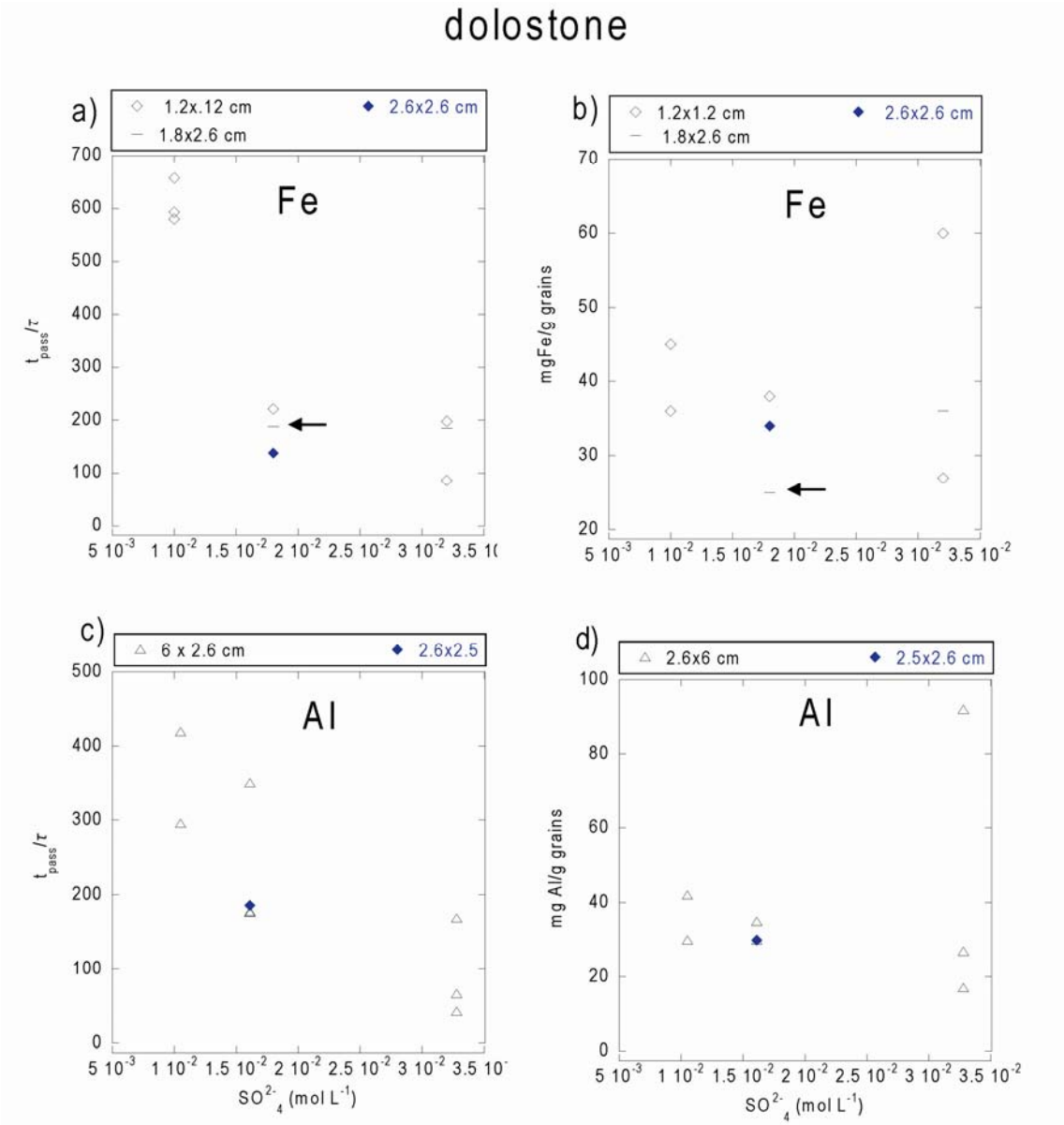

Figure 3.3 *Efficiency of the dolostone column experiments. Plots of passivation time normalized to residence time (τ) vs. input concentration of SO_4 are shown in a) and c): a) = column experiments with $Fe_2(SO_4)_3$ input solutions and c) = column experiments with $Al_2(SO_4)_3$ input solution). Plots of metal retention vs. input SO_4 relative to iron and aluminum experiments in b) and d): b) = Fe input solution and d) = Al input solution. Black arrows in (a) and (b) show the column that underwent clogging (Table 3.2). Different symbols represent different column sizes (length and diameter).*

Figure 3.3b,d shows the amount of metal retained (calculated as the product between input metal concentration in mg L^{-1}, flow rate in L h^{-1} and t_{pass} in h), normalized to the initial mass of dolostone, vs. sulfate concentration of the input solution. Like in the limestone-filled column experiments, the plots show no clear trend. Results plotting on the left correspond to experiments with small input sulfate concentrations which gave large t_{pass} values, and results plotting on the right correspond to experiments with larger input concentration which gave lower t_{pass} values. This opposite distribution of input concentrations and t_{pass} can explain the lack of a trend in metal retention with input concentration.

3.3.3.2 Aragonite-filled columns

Figure 3.4a,c shows plots of t_{pass}/τ *vs*. initial SO_4 concentration for iron and aluminum experiments, respectively. Trend of the plots shows that, similarly to the limestone and dolostone-filled column experiments (Chapter 2 and Soler et al. (2008)), t_{pass}/τ increased when decreasing the input sulfate (and metal) concentrations in both, the Fe and Al columns.

Clogging occurred only in three iron-column experiments of 1.2 x 1.2 cm and one of 2.6x2.6 cm. Reproducibility of the experiments was little in both iron and aluminum experiments at low sulfate concentration (SO_4 = 1.05x10^{-2} mol L^{-1}): $t_{pass/\tau}$ varied from 782 to 1661 (Fe experiments) and from 155 to 432 (Al experiments). Aluminum experiments also displayed little t_{pass}/τ reproducibility at high sulfate concentrations (SO_4 = 3.28x10^{-2} mol L^{-1}; t_{pass}/τ ranged from 90 to 179).

Figure 3.4b,d shows the amount of metal retained, normalized to the initial mass of aragonite, vs. sulfate concentration of the input solution. The graphs show that those experiments with small input sulfate concentrations had longer t_{pass} (left side), and the experiments with higher sulfate concentration had lower t_{pass} (right side). Like in the dolostone experiments, experiments show no clear trend between metal retained and the initial sulfate concentration.

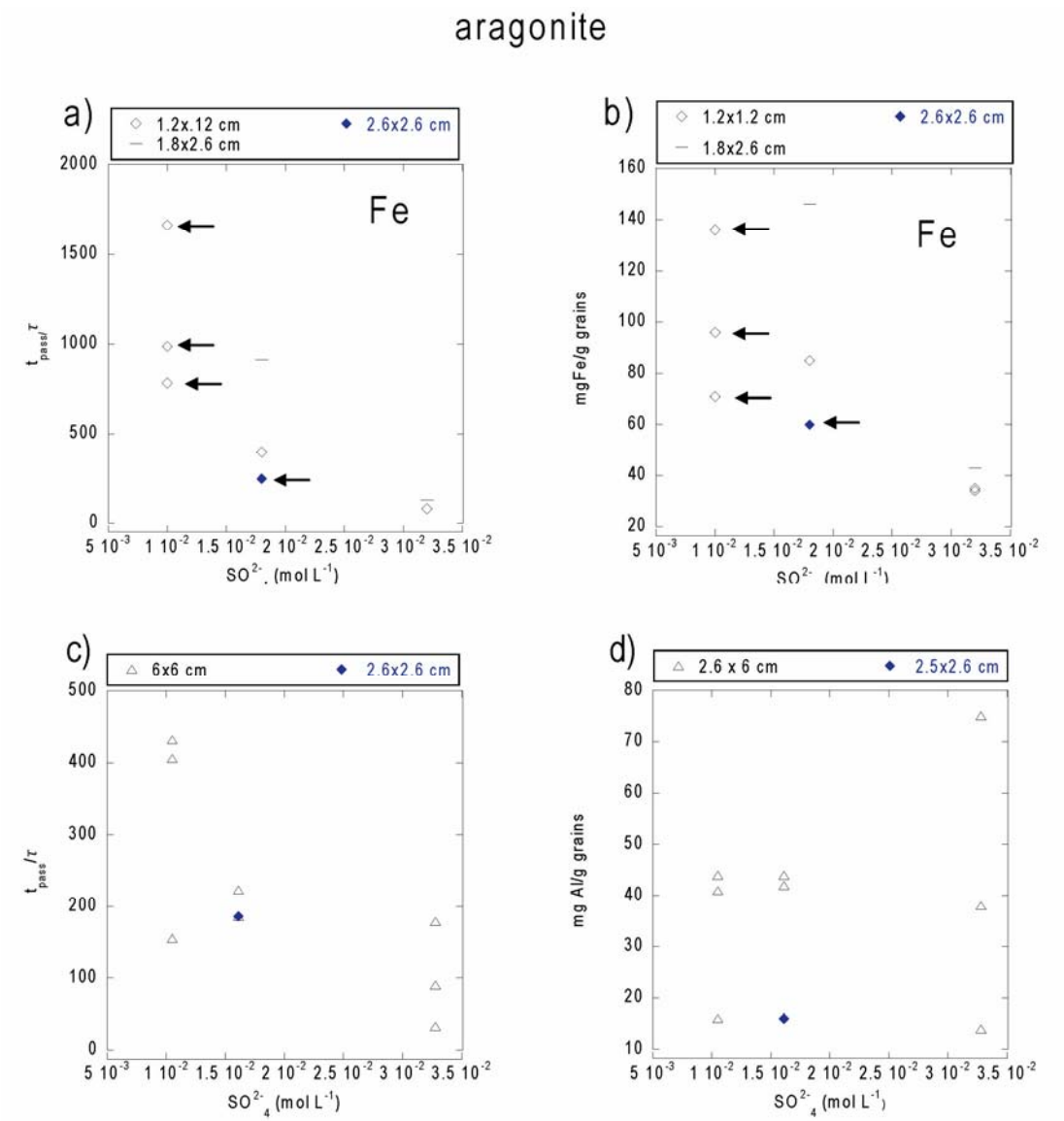

Figure 3.4 *Efficiency of the aragonite column experiments. Plots of passivation time normalized to residence time (τ) vs. input concentration of SO_4 are shown in a) and c): a) = column experiments with $Fe_2(SO_4)_3$ input solutions and c) = column experiments with $Al_2(SO_4)_{3v}$ input solution). Plots of metal retention vs. input SO_4 relative to iron and aluminum experiments in b) and d): b) = Fe input solution and d) = Al input solution. Black arrows in (a) and (b) show columns that underwent clogging (Table 3.2). Different symbols represent different column sizes (length and diameter).*

3.3.3.3 Comparison between dolostone and aragonite-filled columns and limestone-filled ones

The plots in Fig 3.5 are useful to compare the efficiency between the limestone-filled columns (Chapter 2) and the dolostone- and aragonite-filled columns. In all experiments, regardless the mineral carbonate (calcite in limestone, dolomite in dolostone and aragonite) experiments showed a similar trend characterized by an

increase in t_{pass}/τ by decreasing the initial sulfate concentration (Fig 3.5 a, c). In the iron experiments (Fig 3.5a), t_{pass}/τ ranged from 580 to 2561 in columns run with low initial sulfate solution ($1.0x10^{-2}$ $molL^{-1}$). In the aluminum experiments, t_{pass}/τ ranged from 160 to 460 at lower concentration (Fig. 3.5c). The variability in t_{pass}/τ diminishes as the input sulfate concentration increases.

Large variability in t_{pass}/τ and metal retention as a function of the input sulfate concentration makes the comparison between the three carbonate minerals difficult. A reasonable explanation for this fact would be that, more than compositional and mineralogical differences, creation of preferential flow paths affects the efficiency of the carbonate mineral-filled columns (see Chapter 2 and following section).

Comparison of the amounts of iron and aluminum retained normalized to the initial mass of calcite, dolomite or aragonite *vs.* initial sulfate concentration is shown in Fig. 3.5b,d. It appears that iron retention is similar between the limestone-filled columns and the aragonite-filled ones compared to the dolostone-filled columns, resulting in a lack of trend in either case. In addition, iron retention is higher in the limestone and aragonite-filled columns compared to dolostone. In the case of aluminum, Al retention vs. input sulfate concentration does not show a clear trend.

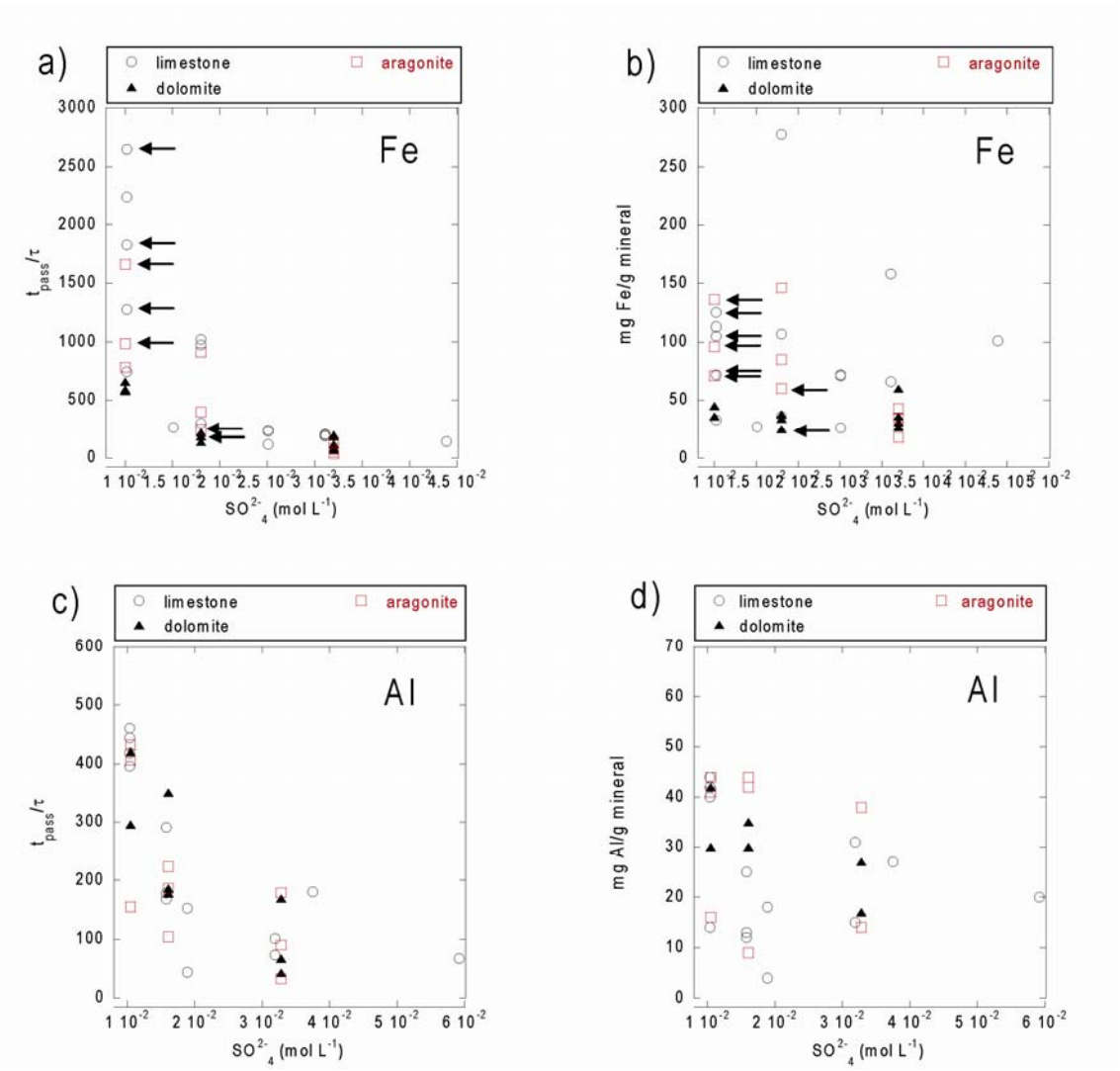

Figure 3.5 *Comparison of the efficiency between the limestone columns (Chapter 2) and aragonite and dolostone columns. Different symbols represent different mineral. Plots of passivation time normalized to residence time (t_{pass}/τ) vs. input concentration of SO_4 are shown in a) and c) (input solution of $Fe_2(SO_4)_3{\cdot}5H_2O$ and $Al_2(SO_4)_3{\cdot}16H_2O$, respectively). Plots of metal retention vs. input SO_4 concentration are shown in b) and d). The black arrows indicate columns that underwent clogging.*

3.3.4 Porosity variation

mCT examination of six column experiments (mCT AR1, mCT AR2, mCT AR3 mix, mCT DOL1, mCT DOL2 and mCT DOL3 mix; Tables 3.1 and 3.2) allowed detailed identification of the changes in mineralogy and porosity with time. Figures 3.6 and 3.7 show passivated column experiments (mCT AR2 and mCT DOL2, respectively).

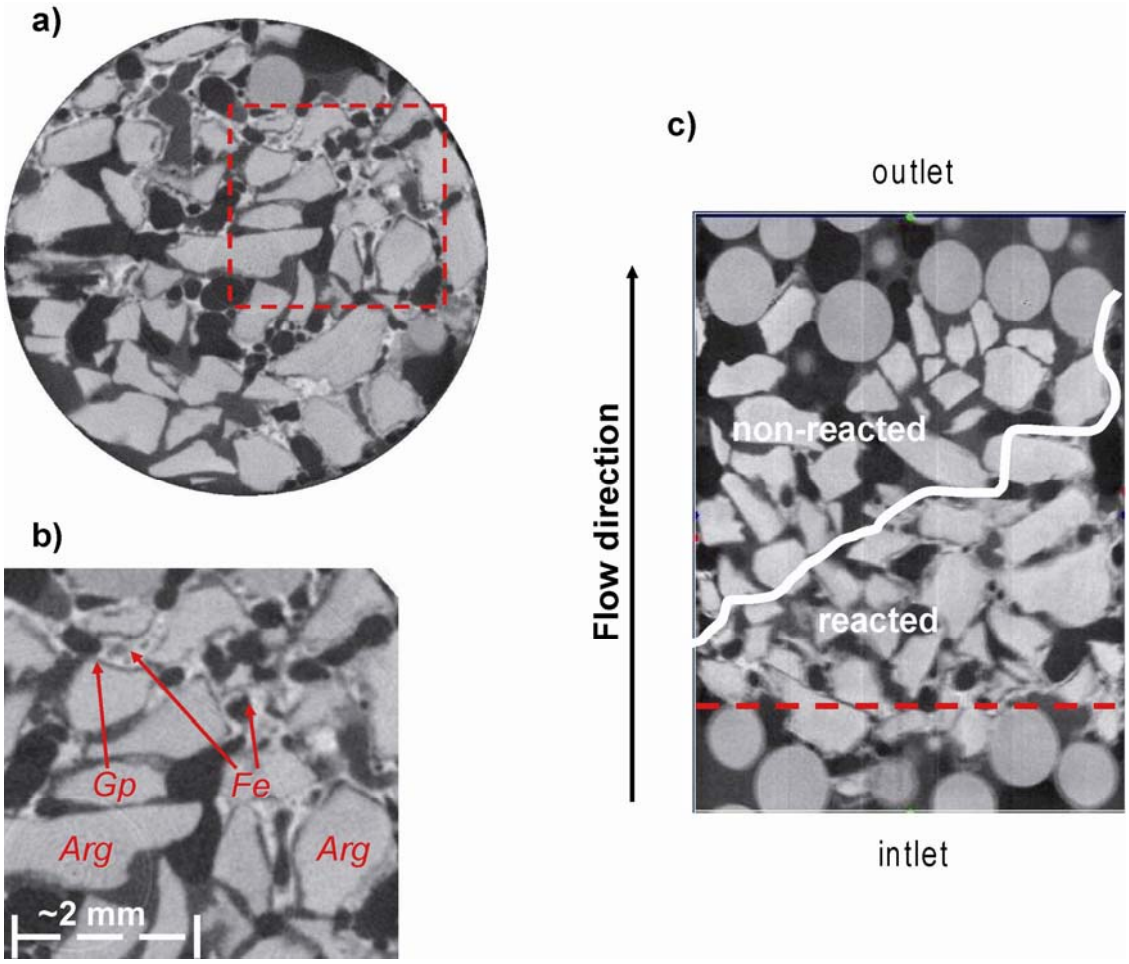

Figure 3.6 *mCT images of column mCT AR 2 (aragonite) of 1.2 cm in diameter and 1.2 cm long after passivation. Aragonite grains (Arg) are coated by gypsum (Gp) (dark-gray layer surrounding aragonite surfaces), amorphous $Fe(OH)_3$ (Fe) precipitates between aragonite grains, and dark areas are pores: a) horizontal cross section near the inlet (shown by the dashed line in c); b) zoom-in of the red dotted square in a); c) vertical cross section taken at a diametric plane: light-gray circles at the outlet and inlet areas are glass beads. The white line separates a reacted from a non-reacted zone.*

Figures 3.6a and 3.7a show two horizontal cross sections of the lower part of the columns (near the inlet). In both columns, the images show that precipitates have surrounded most of the dolostone and aragonite grains, suggesting homogenous carbonate dissolution. Enlargements of the framed zone (Figs. 3.6b and 3.7b) show a whitish mass, which corresponds to amorphous $Fe(OH)_3$, precipitated between grains and dark-grey layers, associated to gypsum, coating the grain surfaces (*Gp*; previously identified by XRD). The mCT measurements showed formation of preferential flow paths that left isolated volumes of unreacted grains in the columns (Figs. 3.6c and 3.7c). This was already observed in the limestone-filled columns (Chapter 2). Formation of the isolated volumes was rather random from one experiment to another, leading to an

unpredictable variability of t_{pass}/τ in experiments run under the same conditions (see Figs. 3.3, 3.4 and 3.5).

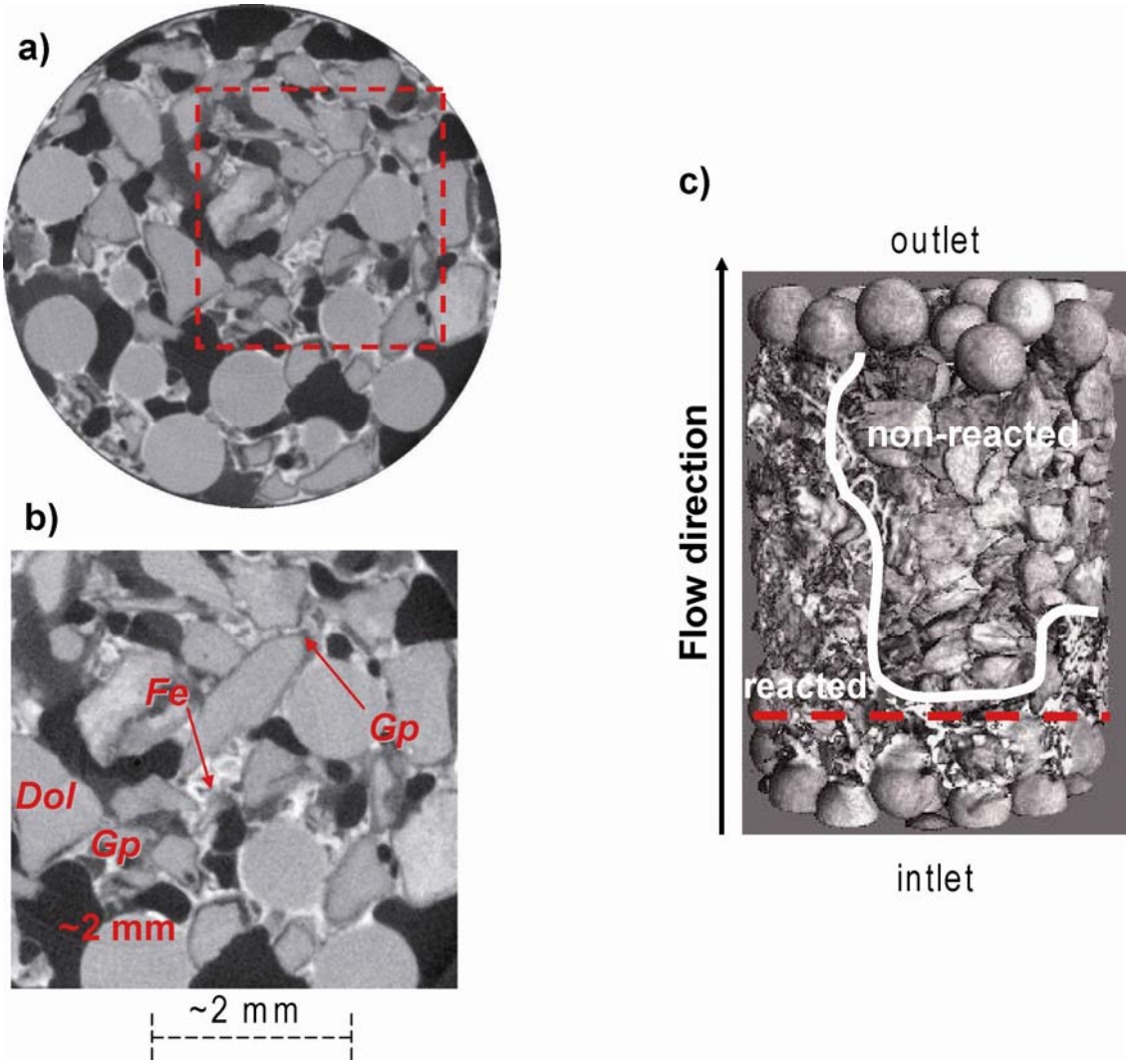

Figure 3.7 *mCT images of column mCT DOL 2 (dolostone) of 1.2 cm in diameter and 1.2 cm long after passivation. Dolomite grains (Dol) are coated by gypsum (Gp) (dark-gray layer surrounding aragonite surfaces), amorphous $Fe(OH)_3$ (Fe) precipitates between dolomite grains, and dark areas are pores: a) horizontal cross section near the inlet (shown by the dashed line in c); b) zoom-in of the red dotted square in a); c) 3D reconstruction of the entire passivated column: light-gray spheres at the outlet and inlet areas are glass beads. The white line separates a reacted from a non-reacted zone.*

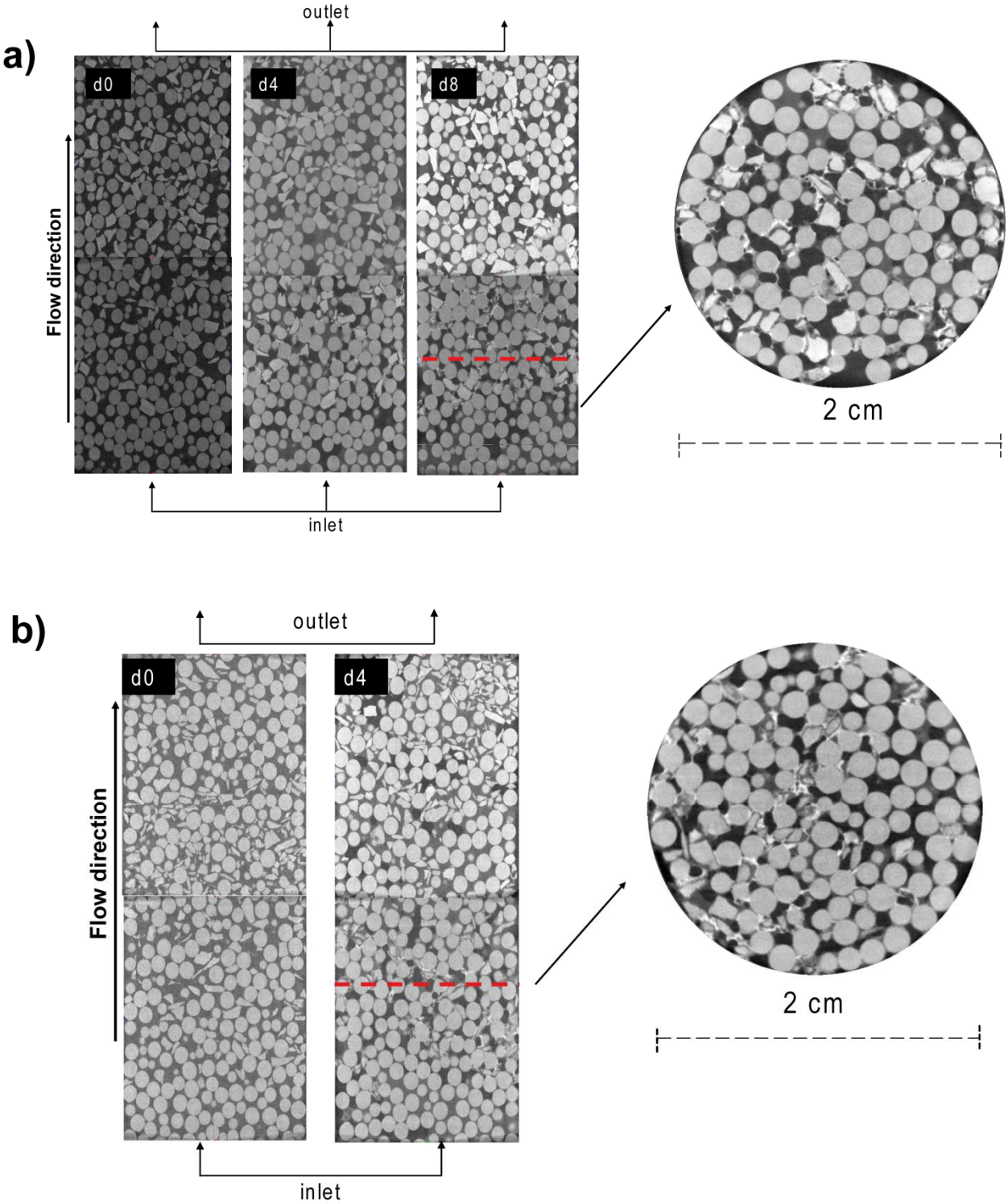

Figure 3.8. *mCT images of a) column mCT AR 3 (aragonite) and b column)mCT DOL 3 (dolostone) both with 2.6 cm in diameter and 6 cm long. Vertical cross sections taken at a diametral plane during the experiment: d0, before reaction; d4 and d8 after 4 and 8 days. Experiments were stopped before reaching passivation. The depicted horizontal cross sections of the lower part of both columns show homogeneous distribution of amorphous* $Fe(OH)_3$ *precipitates.*

In columns filled with a mixture of beads and mineral grains (Tables 3.1 and 3.2), dissolution and precipitation reactions occurred homogeneously along the columns, as it is shown in the mCT images of Fig. 3.8. Passivation was not observed during these

experiments. Distribution of precipitates with time suggests that mixing glass beads and mineral grains yields a homogeneous circulation of the solution as it was observed in the limestone-filled columns (Chapter 2) and different experimental setups (DAS experiments by Rotting et al. (2005) and Caraballo et al. (2011)). Nevertheless, although preferential flow paths were eliminated, variation in t_{pass}/τ still occurs (Fig. 3.3 and 3.4).

As expected, porosity variation in the dolostone and aragonite-filled column occurred. Similar to limestone-filled columns (Chapter 2) precipitation of metal-hydroxides and gypsum and formation of preferential flow paths play a key role in porosity changes. Once the injected solution reacted with the grains, a reaction front advanced upwards. The contribution of gypsum and amorphous $Fe(OH)_3$ precipitates to porosity decrease during the experiment was calculated using the mCT image segmentation method. Figure 3.9 shows porosity variation along the column in 4 column experiments (mCT AR1, mCT AR2, DOL1 and mCT DOL2).

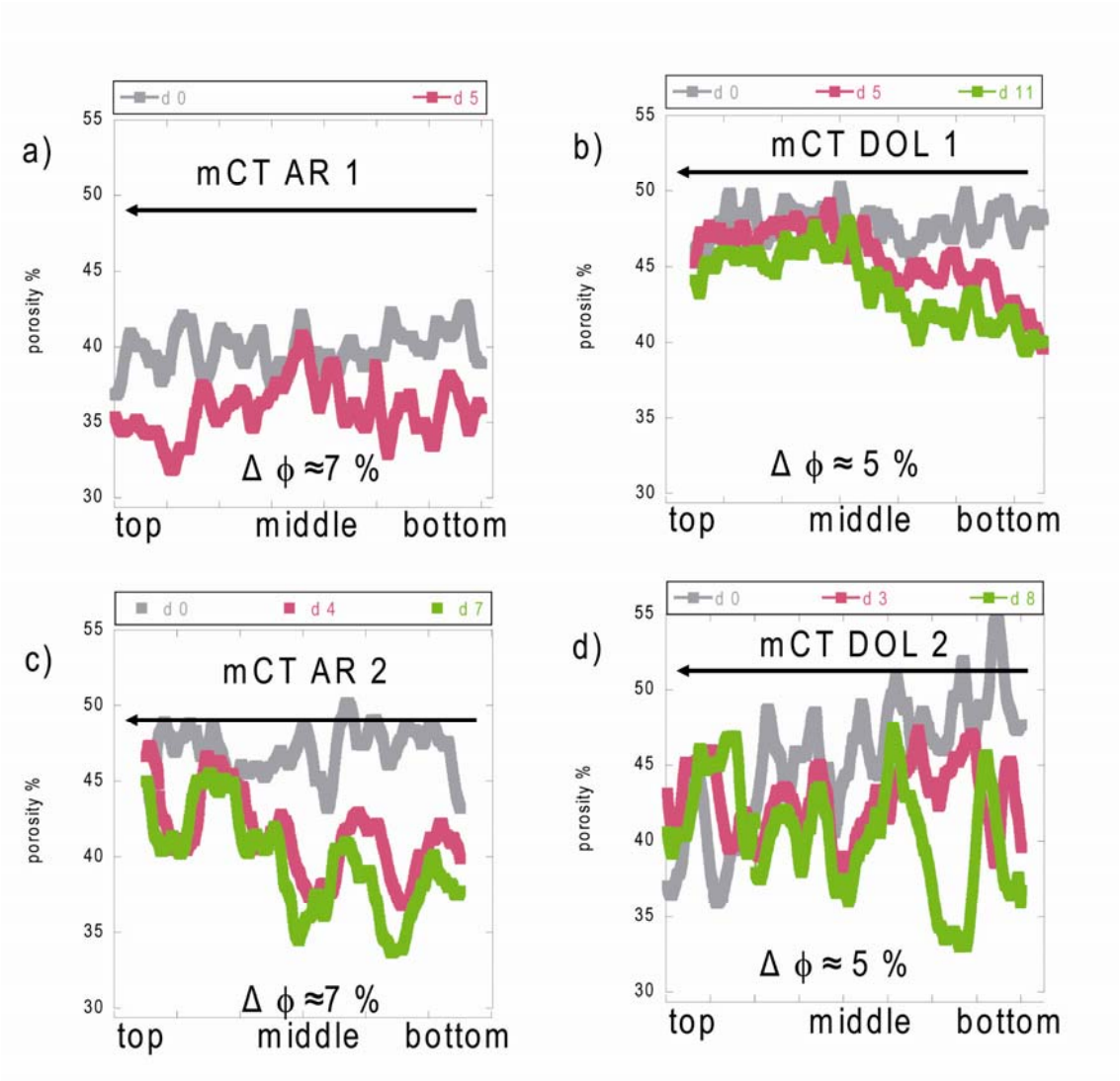

Figure 3.9 *Porosity variation with time along four passivated columns: a) mCT AR1 (aragonite), b) mCT DOL1 (dolostone), c) mCT AR2 (aragonite) and d) mCT DOL 2 (dolostone). The arrows indicate the flux direction. d0 represents measurement at time 0 and di represents measurements at different days. Porosity always decreased from initial value of: a) 39 ± 2 % to 36 ± 2 %; b) 48 ± 2 % to 43 ± 2 %; c) 47 ± 2 % to 40 ± 2 % and d) 45 ± 2 % to 40 ± 2 %.*

Gray lines represent porosity distributions before the experiment, red lines represent porosity after the first stop (3, 4 or 5 days depending on the experiment), and green lines represent porosity once columns were passivated. As already shown in Chapter 2, reaction fronts start to act at the bottom and then move forward to the top of the column; so also porosity decreases from the bottom to the top. The final average of porosity decrease was 7% for aragonite-filled columns (mCT AR1 and mCT AR2), and 5% for dolostone-filled columns (mCT DOL1 and mCT DOL2). A preferential flow path effect is especially visible in (mCT AR2; Figure 3.9c). Once the experiment started, after the first mCT measurement, the column was scanned after 4 days and after 7 days.

Passivation was achieved after ~4 days and porosity decreased abruptly during this first step. The negligible porosity changes after 7 days (Figure 3.6) show the clear role of preferential flow paths in porosity decrease. After the column was passivated, flow continued to circulate and with no further effect on porosity changes.

3.4 Summary and conclusions

The use of crushed aragonite and dolostone in passive treatment of AMD was studied employing centimetric-scale column experiments. Both aragonite and dolostone turned out to be efficient in treatments of AMD. Processes inducing acidity neutralization and metal retention are essentially the same as those for calcite: carbonate dissolution, proton consumption, and metal and gypsum precipitation. Passivation by gypsum coating is an important limitation to the dolomite and aragonite buffer capacity. Nonetheless the main factor for controlling passivation time was the initial sulfate concentration. A decrease in sulfate concentration rate enhance the column passivation time. Aragonite-filled columns tended to show longer passivation time and higher metal retention than dolomite at low input sulfate concentration in iron experiments. A comparable passivation time was observed in aluminum experiments.

Like in the limestone-filled columns, metal retention does not show the same trends as passivation time in the aragonite- and dolostone-filled columns: there is little sensitivity of metal retained on initial sulfate (and metal) concentration due to the negative correlation between initial concentration and passivation time.

In several experiments precipitation of iron or aluminum hydroxides between grains favored formation of preferential flow paths and column clogging. These complementary phenomena impede homogeneous circulation of the solutions through the columns, limiting significantly the treatment efficiency and causing unpredictable passivation time. To improve the efficiency in the passive treatment, mixtures of carbonate grains and glass beads were used to pack the columns. The addition of an inert substrate leads to an improvement of the efficiency.

It was observed that porosity decreased progressively with time. Porosity loss was between 5 and 7 %. Due to the formation of preferential flow path, porosity reduction was stronger at the inlet of the columns.

Comparison between aragonite and dolostone experiments with limestone ones showed that passivation time and Al retention occurred at the same order of magnitude for the three minerals; this encourages their use in AMD treatment. In the case of Fe, dolostone experiments showed that passivation time and Fe retention tended to be lower than those of calcite and aragonite experiments. This latter observation is an issue concerning further investigation since only dolomite has less Ca ($CaMg(CO_3)_2$) than calcite and aragonite ($CaCO_3$).

Part II:

Processes regulating gypsum coating on carbonate minerals' surface

Chapter 4

Coupled dissolution of Ca-carbonate minerals and precipitation of gypsum: batch experiments

4.1 Introduction

This chapter deals with the coupled reactions of dissolution of carbonate minerals and gypsum precipitation and attempts to discern differences and similarities of the overall mechanism when calcite, aragonite or dolomite dissolve. In addition, the gypsum precipitation rates on the Ca-carbonate substrate are quantified allowing a comparison with the gypsum precipitation rate calculated from the rate law proposed by Reznik et al. (2011) and Rosenberg et al. (2012), in the absence of a Ca-carbonate substrate. To this end, batch experiments at constant temperature (25 ± 1°C) and atmospheric pressure were carried out in acidic solutions at pH 2 (H_2SO_4) and equilibrated with respect to gypsum ($CaSO_4 \cdot 2H_2O$) in which Ca-carbonate samples of different size (powder, grains and fragments) acted as substrate.

4.2 Materials and methods

4.2.1 Sample characterization

Batch experiments were performed with calcite, limestone, aragonite and dolostone. Aragonite was obtained from the shell of commercially available common cockle,

Cerastoderma edule. Shells were immersed in 0.5 M NaOH solution for a week and cleaned with a brush to eliminate possible films of organic matter usually adhered on the surfaces. Thereafter, the shells were crushed and sieved to obtain a grain fraction of 1-2 mm in size. Residual microparticles on selected grains were removed using an ultrasonic bath in anhydrous ethanol for 15 min. XRD analysis showed the grains to be composed of aragonite only. Limestone samples obtained from the Roca Quarry in the Garraf area (near Barcelona) were crushed and sieved to obtain a grain fraction of 1-2 mm in size. To remove calcite microparticles, grains were pre-washed with doubly distilled water several times until clear output water was collected. Finally grains were dried at 50 ºC for 24 h. Optically pure specimens of Iceland Spar from Chihuahua (Mexico) were used to obtain powder samples of 100-300 micrometers in size and single fragments of ≈ 1.5x1.2x05 cm^3 with freshly cleaved surfaces. Dolostone samples were obtained from a Triassic dolostone formation in the Corbera area (Barcelona). Samples were crushed and sieved to obtain a grain size of 1-2 mm. To remove microparticles, grains were pre-washed with doubly distilled water several times until clear output water was collected.

XRD patterns of the limestone and dolostone samples, performed with a Bruker D-5005 diffractometer, using Cu K-α1 radiation (λ = 1.5406 Å) at 40 kV and 30 mA, 2θ scanning range from 4° to 60°, and a scan step and step duration of 0.05° and 3 s, respectively, showed only calcite peaks in the limestone and peaks of calcite and dolomite in the dolostone. The Rietveld analysis of the dolostone-XRD pattern (Young, 1995) yielded 90 wt. % of dolomite and 10 wt. % of calcite.

4.2.2 Experimental setup

Batch experiments were conducted in 250 mL polyethylene bottles (Kartell company) placed in a rocking thermostatic water-bath held at a constant temperature (25±0.1 ºC) (Fig.4.1). Most of the experiments were horizontally shaken at 50 rpm. 200 mL of solution of pH 2 (H_2SO_4 and equilibrated with respect to gypsum) were mixed with desired amounts of mineral (powder, grain or fragment) that ranged from ca. 1.7 g to 3 g. A set of 7 experiments, namely multi-point experiments (Table 4.1), was performed to sample 0.5 g of solution after time spans progressively increased by a factor of ≈ 2

(e.g., after 2, 4, 8, 16 min, etc.) until the end of the experiment (between 21 and 150 days ;Table 4.1).

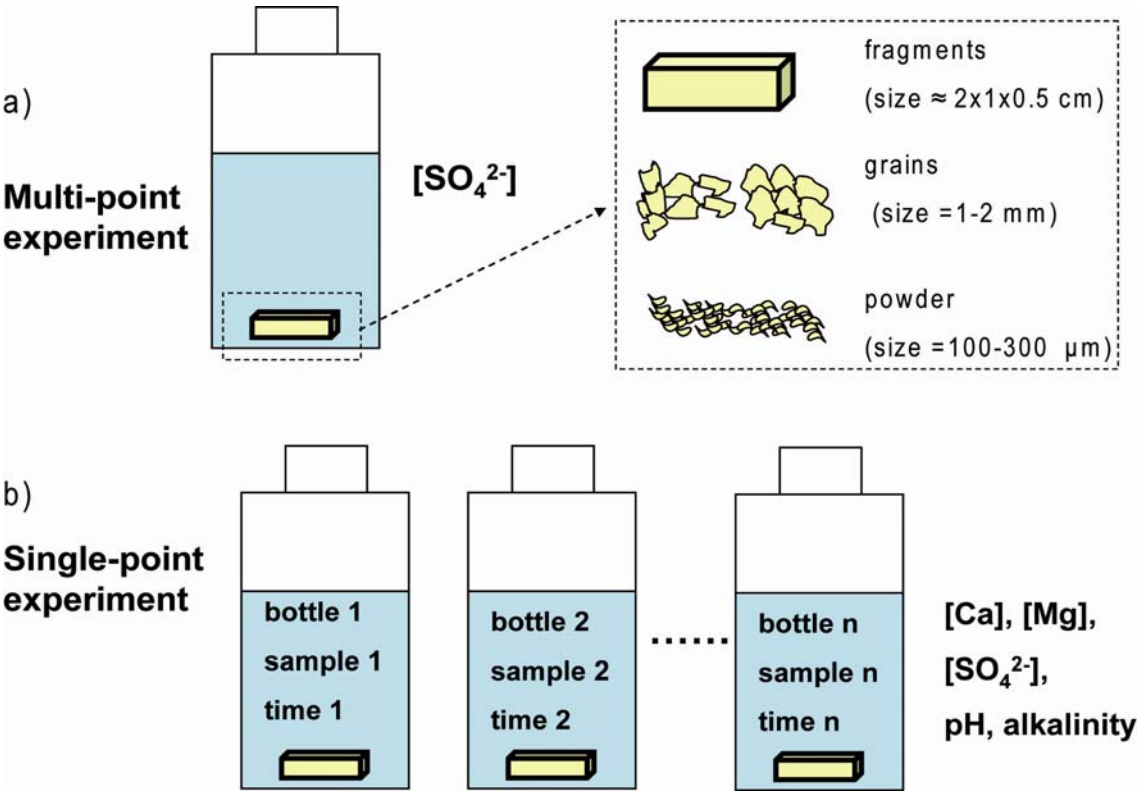

Figure 4.1 *Scheme of the experimental setup a) multi-point experiments: solution and solid sample were placed in a single bottle from the beginning to the end of the experiment. 0.5 g of solution were taken at different time intervals to measure the SO_4^{2-} concentration. At the end of the experiment, the solid sample was retrieved; b) single-point experiments: several bottles filled with 200 mL of the same input solution and the same amount of mineral sample. 1.5 g of solution were taken from each bottle at different time intervals to measure the SO_4^{2-}, Ca and Mg concentrations. pH was immediately measured after sampling. Thereafter, solid sample was retrieved and the bottle was removed.*

Sample solutions were immediately filtered through a 0.45 µm Millipore filter, diluted by a factor of 100 (by weight) using doubly distilled water and analyzed for SO_4^{2-} concentration. Throughout the multipoint experiments the volume of solution decreased less than 5 % of the initial volume. Once the batch experiments were finished, the liquid suspension containing the solid grains was filtered trough a 0.45 µm Millipore filter to examine the solids by XRD and scanning electron microscopy (SEM) using a Hitachi H-4100 FE instrument under a 15–20 kV potential. Most of the experiments were repeated at least twice to ensure reproducibility of the results (Fig. 4.2).

A second set of 4 experiments, namely single point, consisted of mixing the same amount of solid sample in 200 mL of solution in different 250 mL polyethylene bottles. First, 0.5 g of solution were sampled from the first bottle after the first desired time

span, and the solid sample was retrieved. Next bottles were consequently sampled after time spans that were also increased by a factor of ≈ 2 from the previous one (e.g., after 2, 4, 8, 16 min, etc.) until the end of the experiment (last bottle) (Table 4.1). Sampled solutions were filtered through a 0.45 μm Millipore filter and analyzed for concentrations of SO_4^{2-}, Ca and Mg, pH and alkalinity. The solid/liquid ratio in all single point experiments was the same. The retrieved solid samples were also examined by SEM and XRD.

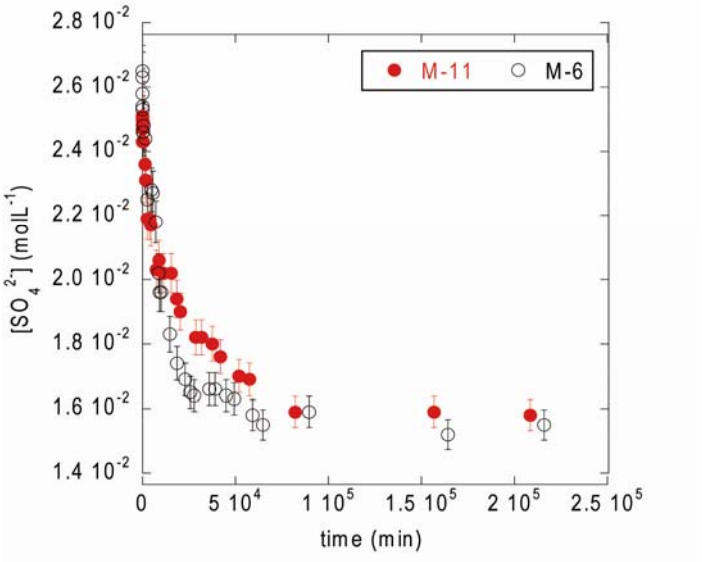

Figure 4.2 *Variation in SO_4^{2-} concentration with time in two experiments run under the same experimental conditions. The reproducibility of the experiments is shown.*

4.2.3 Solutions

Solutions of pH 2 (H_2SO_4) were prepared with doubly distilled water and equilibrated with respect to gypsum at 25 °C. Solution pH was adjusted by adding a proper amount of analytical-grade H_2SO_4 (95-97%). Equilibration with respect to gypsum was achieved by adding sufficient amounts of $CaSO_4 \cdot 2H_2O$ powder to reach equilibrium (ca. 8 g in 2 L). Solutions were stirred for 90 h and filtered through a 0.45 μm Millipore filter using a vacuum pump.

pH measurements were carried out using a InoLab pH meter, equipped with a WTW Sentix 21 electrode calibrated with an accuracy of ± 0.02 pH units. The electrode was calibrated with Crison buffer solutions at pH 4 and 7. Concentration of SO_4^{2-} was measured by high pressure liquid chromatography (Dionex DX500). Eluent solution containing 1.8 mM Na_2CO_3 and 1.7 mM $NaHCO_3$ was pumped through a guard column (AG4A-SC) and an anion column (AS4ASC) at a flow rate of 2 mL min^{-1}. Approximately 0.5 mL of diluted sample (sample/doubly distilled water ratio = 1:100) was injected using an auto-sampler into a 25 μL feeding loop. Based on standard solution measurements, the associated uncertainty was ± 3% (one standard deviation). Total concentrations of Ca and Mg were analyzed by Inductively Coupled Plasma Atomic Emission Spectroscopy (ICP-AES) using a thermo Jarrel-Ash spectrometer equipped with a CID detector. Detection limits for Ca and Mg were 10^{-5} mol L^{-1} and $5 \cdot 10^{-6}$ mol L^{-1}, respectively. The associated uncertainty was better than ± 3% (one standard deviation). Alkalinity was measured by titration (HCl) using a Potentiometric Tritando mod 907 (Metrhom).

Table 4.1 *Initial and final experimental conditions in the batch experiments*

	initial conditions					final conditions			
experiment	pH	mass (g)	sample	SO_4^{2-} (mol L^{-1})	Ca (mol L^{-1})	dissolved mass (g)	dissolved mass (%)	precipitated gypsum (g)	duration (minute; day)
M-6	2.12	1.767	Iceland spar fragment	2.64E-02	n.a.	–	–	0.375	216000; 150
M-7 *	2.12	1.690	Iceland spar fragment	2.64E-02	n.a.	–	–	0.341	64860,;45
M-10	2.13	2.901	Iceland spar powder (100-300 µm)	2.51E-02	n.a.	–	–	0.374	210300; 146
M-11	2.21	3.087	Iceland Spar fragment	2.45E-02	n.a.	–	–	0.300	208620; 144
M-14	2.21	3.029	limestone (1-2 mm)	2.42E-02	n.a.	–	–	0.300	198720; 138
M-15	2.21	3.067	aragonite (1-2 mm)	2.42E-02	n.a.	–	–	0.258	198720; 138
M-16 **	2.21	3.096	dolostone (1-2 mm)	2.42E-02	n.a.	–	–	0.210	198720; 138
S-17	2.17	3.000	Iceland spar powder (100-300 µm)	2.48E-02	1.59E-02	0.173	5.8	0.245	33120; 23
S-18 **	2.20	3.000	dolostone (1-2 mm)	2.50E-02	1.61E-02	0.041	1.2	0.188	30120; 23
S-19	2.25	3.000	aragonite (1-2 mm)	2.48E-02	1.61E-02	0.187	6.2	0.141	28527; 19
S-20	2.21	3.000	limestone (1-2 mm)	2.32E-02	1.57E-02	0.168	5.6	0.160	31357; 21

*S = single-point experiment; M= multipoint experiment; * unshaken experiment; ** 90 % dolomite and 10 % calcite; n.a. = not analyzed*

4.2.4 Solids

After conclusion of the batch experiments, the retrieved solid samples were examined by scanning electron microscopy (SEM) using a Hitachi H-4100 FE instrument under a 15–20 kV potential and XRD.

4.2.5 Calculations

Based on the measured pH and the concentrations of Ca, Mg and SO_4^{2-} of the sampled solutions, the saturation indexes (SI) with respect to calcite, aragonite, dolomite and gypsum were calculated at 25ºC using PHREEQC and the MINTEQ database (Parkhurst and Appelo, 2013).

The overall reaction that accounts for the coupled dissolution of calcite (or aragonite) and precipitation of gypsum in the batch experiments is:

$$CaCO_3 + SO_4^{2-} + 2H_2O + 2H^+ \leftrightarrow CaSO_4 \cdot 2H_2O + H_2CO_3 \qquad (4.1)$$

The concentrations of Ca released from calcite (or aragonite) dissolution ($[Ca^{2+}]_{diss}$) and sulfate trapped by gypsum precipitation ($[SO_4^{2-}]_{ppt}$) were calculated from the following mass balance equations:

$$\left[Ca^{2+}\right]_{diss} = \left[Ca^{2+}\right]_{sam} - \left[Ca^{2+}\right]_{in} + \left[Ca^{2+}{}_{ppt}\right] \qquad (4.2)$$

$$\left[Ca^{2+}{}_{ppt}\right] = \left[SO^{2-}{}_{4\,ppt}\right] \qquad (4.3)$$

$$\left[SO^{2-}{}_{4\,ppt}\right] = \left\lfloor SO^{2-}{}_{4}\right\rfloor_{in} - \left[SO^{2-}{}_{4}\right]_{sam} \qquad (4.4)$$

where $[Ca^{2+}]_{sam}$ and $[SO^{2-}{}_4]_{sam}$ represent the measured Ca^{2+} and SO_4^{2-} concentrations, respectively, $[Ca^{2+}]_{ppt}$ represents the Ca^{2+} concentration taken by gypsum precipitation, and $[Ca^{2+}]_{in}$ and $[SO_4^{2-}]_{in}$ represent the Ca^{2+} and SO_4^{2-} concentrations of the initial solution, respectively.

In the batch experiments, when the change in $[Ca^{2+}]_{diss}$ and $[SO_4^{2-}]_{ppt}$ is linear with time, the dissolution rates of the Ca-carbonate minerals (R_{diss}) and the gypsum precipitation rate (R_{ppt}) were obtained by linear regression as (mol g^{-1} s^{-1}):

$$R_{diss} = +\frac{d[Ca^{2+}]_{diss}}{dt} \cdot \frac{V}{m_{calcite}} \tag{4.5}$$

and

$$R_{ppt} = +\frac{d[SO_4^{2-}]_{ppt}}{dt} \cdot \frac{V}{m_{gypsum}} \tag{4.6}$$

where V is the volume of the solution and $m_{calcite}$ and m_{gypsum} are the initial and final mass of dissolved calcite and precipitated gypsum, respectively. In the experiments with grains of 1-2 mm of size, R_{diss} was also normalized to the initial geometric surface area (mol m^{-2} s^{-1}) calculated by assuming spherical grains of 1.5 mm in diameter and considering the initial mass of sample and the densities of calcite, aragonite and dolomite.

4.3 Results and discussion

4.3.1 Overall process (carbonate mineral dissolution and gypsum precipitation)

Figure 4.3a, b shows the variation in concentration of SO_4^{2-} with time in a representative experiment performed with an Iceland spar fragment (exp. M-11; Table 4.1). Three stages were distinguished based on the temporal variation of the concentration. The first stage was characterized by a negligible variation in SO_4^{2-} (stage I), the second one by a decrease in SO_4^{2-} (stage II) and the third one by constant SO_4^{2-} concentration (stage III). During stage I, the negligible variation in SO_4^{2-} concentration was associated to gypsum precipitation induction time, which in the absence of crystallization seeds, is the time lapse between the establishment of supersaturation in a solution and the detection of a new phase in the system (Sohnel and Mullin, 1988). In the present study, induction time was determined by measuring the variation in SO_4^{2-} concentrations with time. The uncertainty in SO_4^{2-} measurement was estimated to be 3%. Therefore, the induction time was determined as the first significant change in SO_4^{2-} concentrations from the initial

concentration (beyond 6% from the initial concentration), in the present study it was determined at ca 1000 minutes. In the second stage, the decrease in SO_4^{2-} concentration was caused by gypsum precipitation, and in the third stage, with a constant SO_4^{2-} concentration, equilibrium with respect to calcite was approached, preventing Ca release and further gypsum precipitation.

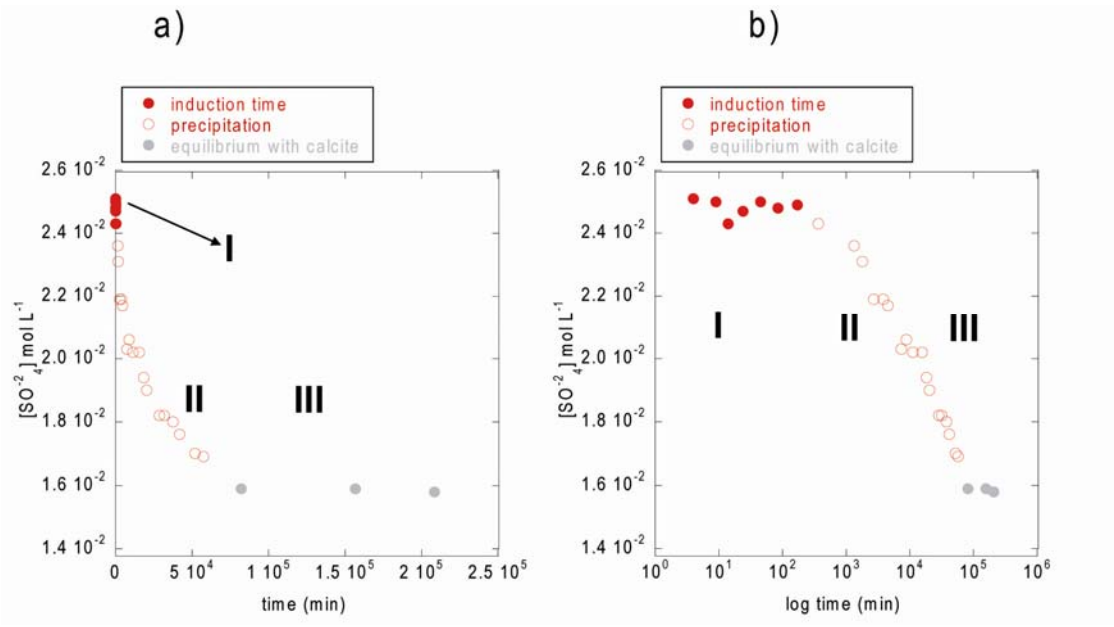

Figure 4.3 *Representative multipoint experiment with Iceland spar fragment (exp. M-11). Variation in SO_4^{2-} concentration versus time in (a) linear scale and (b) logarithmic scale. During the experiment 3 stages were distinguished: stage I (induction time), stage II (gypsum precipitation) and stage III (equilibrium with respect to calcite).*

Figure 4.4 compares the variation in concentration of Ca, SO_4^{2-} and pH with time in three single point experiments with limestone, aragonite and dolostone. The variation in concentration of Ca and SO_4^{2-} and pH with time was similar in the three experiments, suggesting that the coupled dissolution of carbonate mineral and gypsum precipitation occurred similarly.

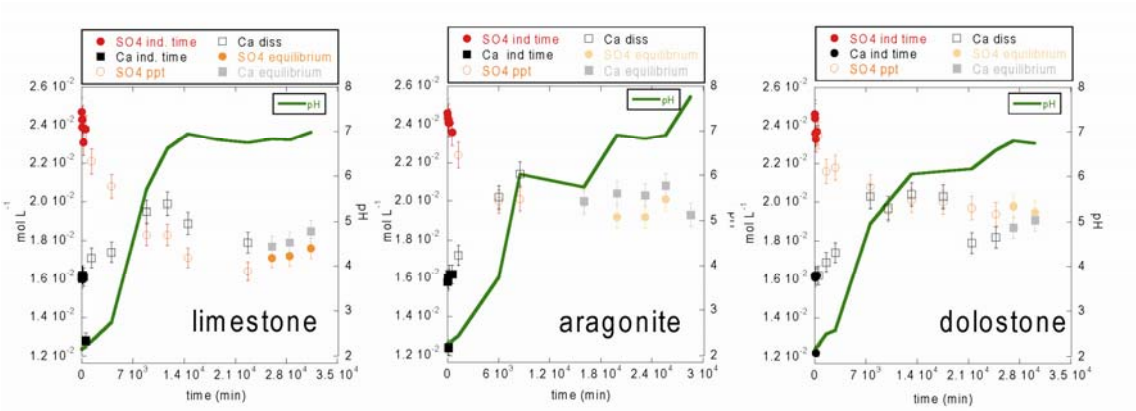

Figure 4.4 *Single point experiments.* *Variation of pH and concentrations of Ca and SO_4^{2-} with time in a) limestone (exp. S-20), b) aragonite (exp. S-19) and c) dolstone (exp. S-18). Ind. time = induction time; ppt. = precipitation and diss. = dissolution.*

The pH increased to reach a value close to 7. The dolostone sample contained 10 % wt. of calcite. Since the calcite dissolution rate is one order of magnitude faster than that of dolomite (Morse and Arvidson, 2002), the release of calcium into solution was mainly from calcite dissolution, and the amount of dissolved calcite using Eq. (4.5) was less than 6% (Table 4.1). Therefore, in the experiments with dolostone, gypsum precipitated from the Ca released by calcite dissolution, a fact that impedes the calculation of gypsum precipitation at the expense of dolomite dissolution.

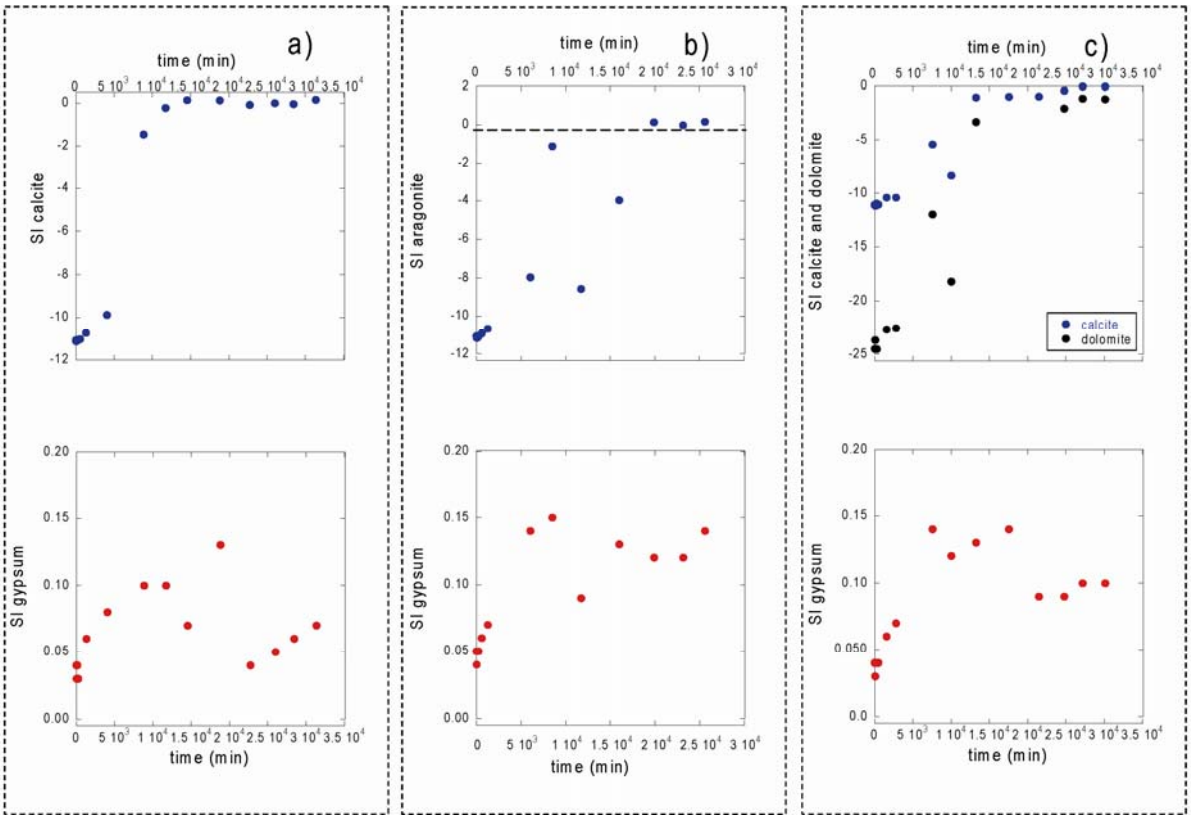

Figure 4.5 *PHREEQC calculated SI with respect to calcite, aragonite, dolomite and gypsum from the sampled solutions of experiments: a) limestone (exp. S-20), b) aragonite (exp. S-19) and c) dolostone (exp. S-18). In b), calculated SI with respect to calcite was nearly the same as that with respect to aragonite.*

The SI values depicted in Fig. 4.5 show that solutions reached equilibrium with respect to calcite (Fig. 4.5a), aragonite (Fig. 4.5b) and calcite (in dolostone experiments) (Fig. 4.5c) and were calculated to be slightly supersaturated with respect to gypsum. Experiments were terminated once equilibrium with respect to calcite was reached or closely approached. The retrieved solid samples showed the presence of gypsum (Fig. 4.6). In the Iceland-Spar powder experiments, gypsum needles were abundant (Fig. 4.6a). In the experiments with grains (Fig. 4.6b,c,d), precipitated gypsum was readily observed on limestone (Fig. 4.6b) and aragonite (Fig. 4.6c) but hardly visible on dolomite (Fig. 4.6d).

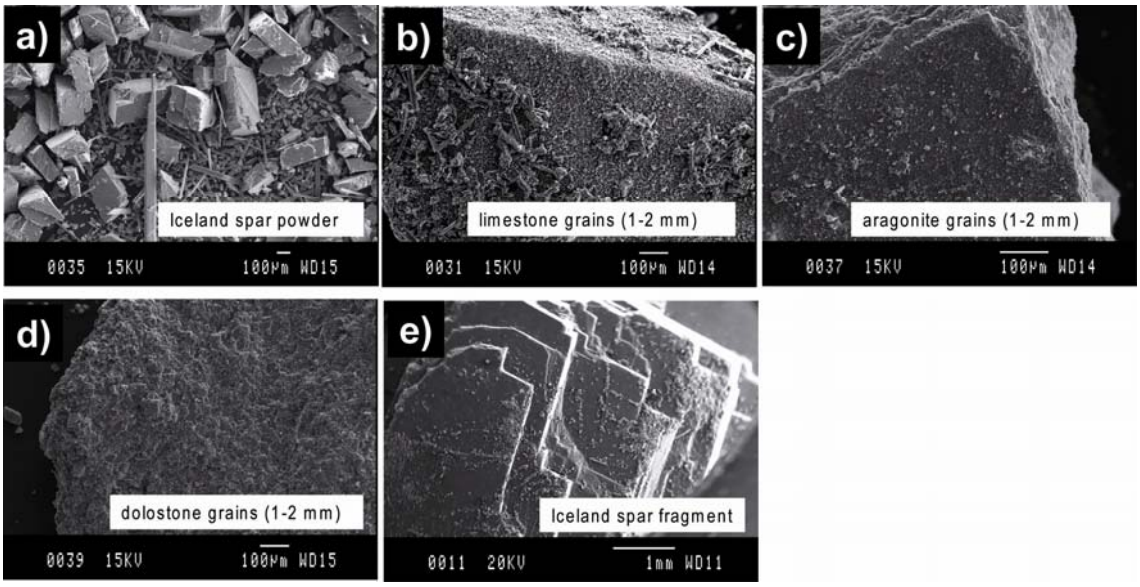

Figure 4.6 *SEM images of the retrieved mineral samples after the experiments were stopped: a) Iceland spar powder (size = 100-300 µm) and needles of precipitated gypsum; grains of b) limestone, c) aragonite and d) dolostone. Precipitated gypsum is observed on the surface of the aragonite and limestone grains. e) Gypsum precipitates spread over the Iceland spar fragment.*

Gypsum precipitates were spread over the Iceland spar fragment (Fig. 4.6e). Figure 4.7a shows that duration of the induction time in the limestone, dolostone and aragonite experiments was similar (≈ 1000 min), as well as the decrease in SO_4^{2-} concentration, independently of the type of experiment (multi or single point). Figure 4.7b shows that equilibrium with respect to calcite and aragonite was also attained after the same time span.

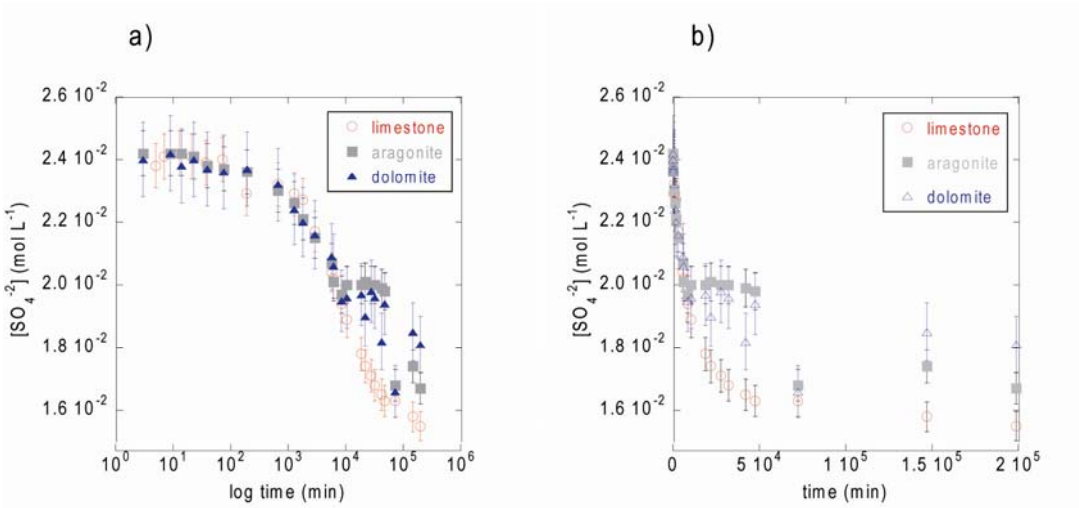

Figure 4.7 *Variation of sulfate concentration in three experiments (limestone (M-14), aragonite (M-15) and dolostone (M-16)): a) log time scale and b) in linear scale.*

4.3.2 Effects of shaking and reactive surface

Experiments M-6 and M-7 were run with the same type of sample and mass to evaluate the influence of shaking on the processes (Table 4.1). Figure 4.8a shows that the variation in concentration with time was similar in both experiments, only with a slightly faster precipitation in the shaken experiment. Taking into account the analytical uncertainty (3%), shaking had a negligible effect on the experimental evolution. Considering this fact and that calcite dissolution is transport controlled (Atanassova et al., 2013 and references therein), it is suggested that the applied shaking was insufficient to favor an increase in dissolution rate.

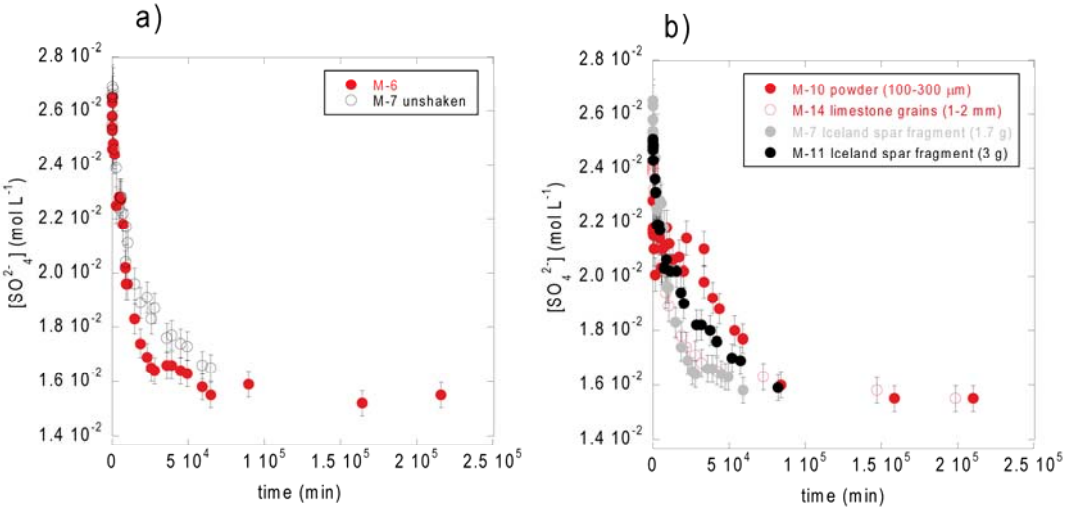

Figure 4.8 *Variation of sulfate concentration with time in: a) shaken and non-shaken experiments and b) experiments with samples of calcite and limestone with different size (powder, grains and fragments).*

Figure 4.8b compares the variation in SO_4^{2-} concentration with time in four different experiments with calcite and limestone with different sample sizes: two experiments were performed with a single Iceland spar fragment (1.7 and 3 g respectively), one with Iceland spar powder (100-300 μm) and one with limestone grains (1-2 mm). The geometric surface areas calculated assuming spherical grains of 100-300 μm, 1-2 mm and 1.0 cm radii are 3.0×10^{-2}, 4.0×10^{-3}, and 4.0×10^{-4} m^2, respectively. The similar decrease in the SO_4^{2-} concentration observed in the four experiments indicated that the effect of the reactive surface area on the dissolution of $CaCO_3$ and, consequently, gypsum precipitation was only minor. This results points out to a transport control of the reaction.

4.3.3 Rates of dissolution of Ca-carbonate minerals and precipitation of gypsum

During the experiments, gypsum precipitation was limited by the Ca released from the $CaCO_3$ dissolution, which was dependent on pH (increase from ca. 2 to 7; Figs. 4.9, 4.10 and 4.11). In the experiments with grains, the dissolution rates (R_{diss}) of calcite, aragonite and dolomite and the gypsum precipitation rate (R_{ppt}) were calculated at pH intervals (pH ≈ 2-3 and pH ≈ 3-5.5) using Eqs. (4.5) and (4.6).

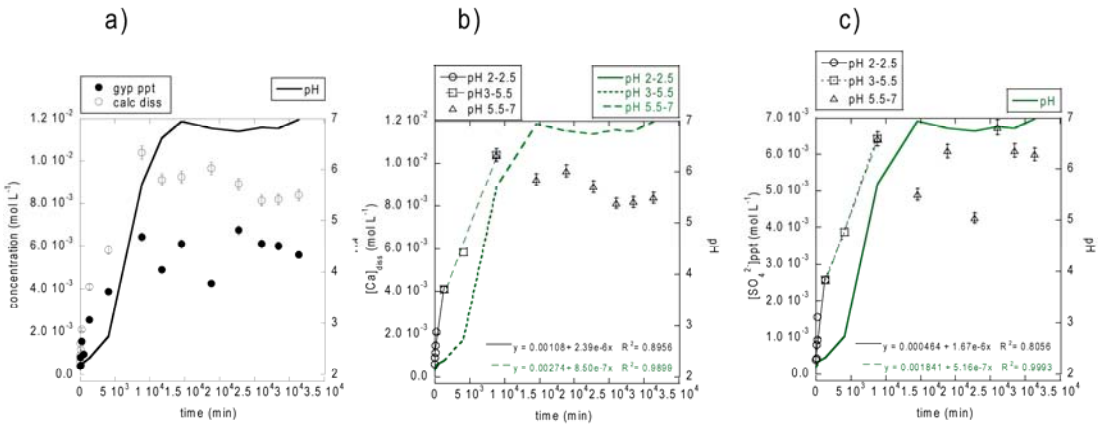

Figure 4.9 Experi*ment with calcite (exp. S-20). a) Variation of $[Ca^{2+}]_{diss}$ and $[SO_4^{2-}]_{ppt}$ concentrations and pH; b) slopes to calculate the calcite dissolution rate with pH and c) slopes to calculate the gypsum precipitation rate with pH.*

In the limestone experiment, R_{diss} of calcite over the pH ranges of ≈ 2-2.5 and ≈ 3-5.5 was 2.4×10^{-6} mol L^{-1} min^{-1} and 8.5×10^{-7} mol L^{-1} min^{-1} (Fig. 4.9b), which normalized to initial limestone mass were 2.7×10^{-9} mol $g^{-1}s^{-1}$ and 9.4×10^{-10} mol $g^{-1}s^{-1}$, respectively. Likewise, gypsum precipitation rates were calculated at the same pH intervals (Fig. 4.9c): $R_{ppt} = 1.7 \times 10^{-6}$ mol L^{-1} min^{-1} (pH ≈ 2-2.5) and 5.2×10^{-7} mol L^{-1} min^{-1} (pH ≈ 3-6), which normalized to the mass of precipitated gypsum were 4.4×10^{-8} mol g^{-1} s^{-1} and 1.4×10^{-8} mol g^{-1} s^{-1}, respectively (Table 4.2). Using the gypsum precipitation rate law that describes the crystal growth of gypsum in the absence of a Ca-carbonate substrate as a function of pH (Reznik et al., 2011 and Rosenberg et al., 2012)

$$\frac{Rate}{S_{BET}} = k_1 \cdot \left(\Omega^{0.5} - 1\right)^{10} + k_2 \cdot \left(\Omega^{0.5} - 1\right)^{2} \qquad (4.7)$$

and the reported BET specific surface area of the gypsum seeds (0.41 m^2 g^{-1}), the rate of gypsum precipitation at pH 2 and pH 3 yields R_{ppt} = 2.1x10^{-9} mol g^{-1} s^{-1} and 8.6x10^{-10} mol g^{-1} s^{-1}, respectively, with the calculated SI value of 0.1 (Fig. 4.5). The rates obtained using Eq. (4.7) are smaller than the ones obtained from the variation in sulfate concentration (Eq. (4.6)).

Table 4.2 *Rates of dissolution of calcite, aragonite and dolomite and rates of precipitation of gypsum.*

pH	mineral (exp.)	R_{diss}			R_{ppt}		
		(mol L^{-1} min^{-1})	(mol g^{-1} sec^{-1})	(mol cm^{-2} s^{-1})	(mol L^{-1} min^{-1})	(mol g^{-1} sec^{-1})	
	calcite (limestone) (S-20)						
2-2.5		2.4x10^{-6}	2.7x10^{-9}	1.8x10^{-10}	1.7x10^{-6}	4.4x10^{-8}	2.1x10^{-9} *
4.25		8.5x10^{-7}	9.4x10^{-10}	6.4x10^{-11}	5.2x10^{-7}	1.4x10^{-8}	8.6x10^{-10} *
	aragonite (S-19)						
2-2.5		3.1x10^{-6}	3.5x10^{-9}	2.4x10^{-10}	1.6x10^{-6}	4.64x10^{-8}	
3		3.6x10^{-7}	3.9x10^{-10}	2.7x10^{-11}	2.3x10^{-7}	6.87x10^{-9}	
	dolomite (dolostone) (S-18)						
2.25		7.5x10^{-8}	8.3x10^{-11}	1.4x10^{-10}	-	-	-
4.25		6.3x10^{-8}	7.0x10^{-11}	1.0x10^{-11}	-	-	-
	Iceland spar (S-17)						
2.5		1.3x10^{-6}	1.5x10^{-9}	1.3x10^{-11}	1.1x10^{-6}	1.9x10^{-8}	
4.5		1.7x10^{-7}	1.8x10^{-10}	1.7x10^{-12}	4.9x10^{-7}	8.4x10^{-9}	

*Rosenberg et al. (2012)

The absence of a substrate in the experiments performed by Reznik et al. (2011) and Rosenberg et al. (2012) suggests that gypsum homogenous nucleation tends to be slower than a heterogeneous one in the presence of substrate (Gill and Nancollas, 1979; Kagawa et al., 1981; Reznik et al., 2009). In addition, dissolution of a Ca-carbonate substrate is a permanent source of Ca, which would increase supersaturation with respect to gypsum, thus enhancing the gypsum precipitation rate. Therefore, gypsum growth is more feasible upon a $CaCO_3$ substrate as the released Ca is readily available.

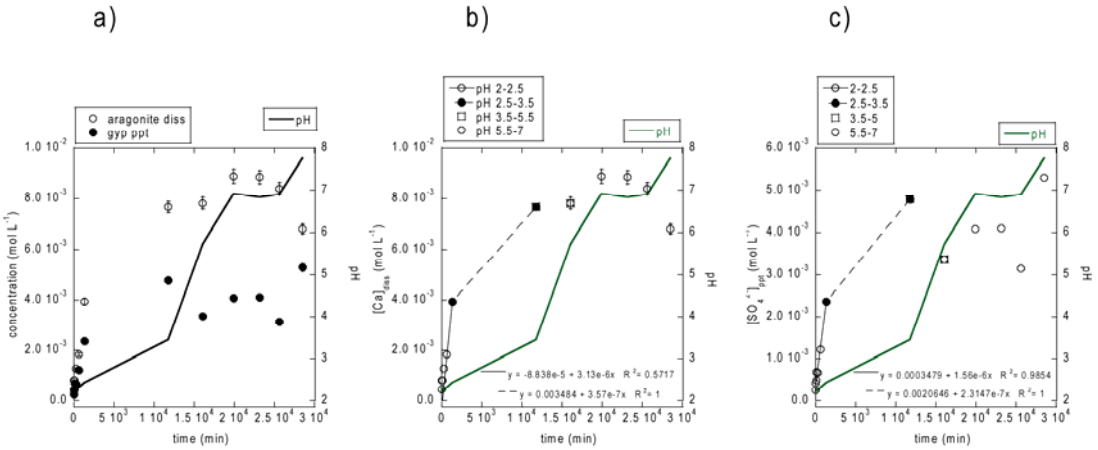

Figure 4.10 *Experiment with aragonite (exp. S-19). a) Variation of* $[Ca^{2+}]_{diss}$ *and* $[SO_4^{2-}]_{ppt}$ *concentrations and pH; b) slopes to calculate the calcite dissolution rate with pH and c) slopes to calculate the gypsum precipitation rate with pH.*

In the aragonite experiment (Fig. 4.10) the rates of aragonite dissolution and gypsum precipitation were likewise calculated: 3.1×10^{-6} mol L^{-1} min^{-1} at pH 2-2.5 and 3.6×10^{-7} mol L^{-1} min^{-1} at pH ≈ 2.5-3.5; Fig. 4.10b). R_{diss} normalized to initial aragonite mass was calculated as: 3.5×10^{-9} mol $g^{-1}s^{-1}$ at pH 2-2.5 and 3.9×10^{-10} mol $g^{-1}s^{-1}$ at pH ≈ 2.5-3.5. Likewise, gypsum precipitation rates were calculated (1.6×10^{-6} mol L^{-1} min^{-1} or 4.6×10^{-8} mol g^{-1} s^{-1} at pH ≈ 2-2.5 and 2.3×10^{-7} mol L^{-1} min^{-1} or 6.9×10^{-9} mol g^{-1} s^{-1} at pH ≈ 2.5-3.5; Fig. 4.10c). Both, the rates of aragonite dissolution and gypsum precipitation at the two different pH intervals are comparable with those obtained in the calcite experiment (Table 4.2). In the dolostone experiment **(**Fig. 4.11a,b), the dolomite dissolution rates were calculated based on the released Mg to be 7.5×10^{-8} mol L^{-1} min^{-1} at pH ≈ 2-2.5 and 6.3×10^{-8} mol L^{-1} min^{-1} at pH ≈ 3-6, which normalized with the dolomite initial mass R_{diss} = 8.3×10^{-11} and 7.0×10^{-11} mol g^{-1} s^{-1}, respectively. As expected, the rates were slower than those of calcite, limestone and aragonite (Table 4.2).

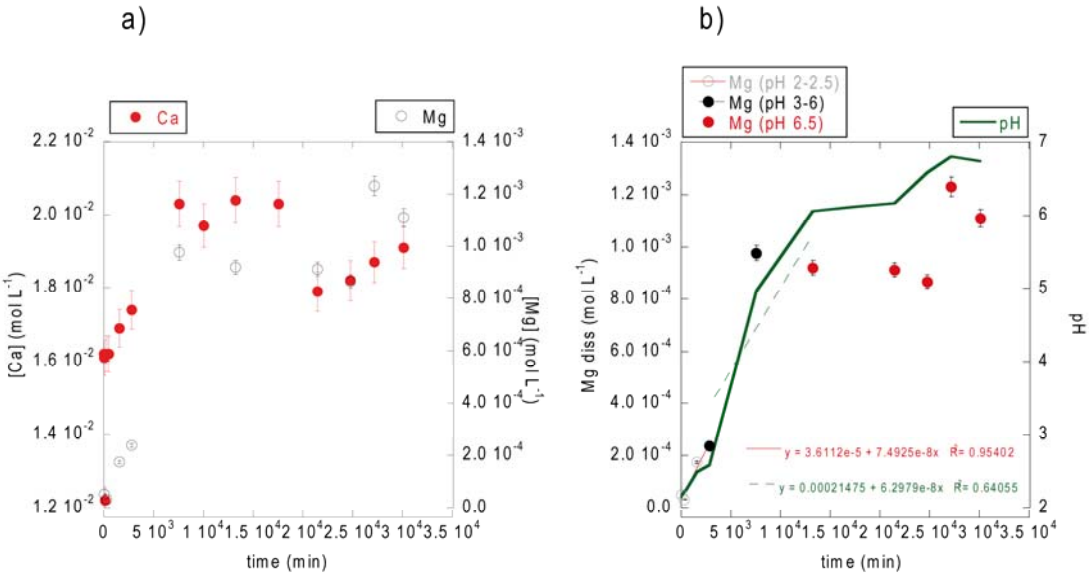

Figure 4.11 *Experiment with dolomite (exp. S-18): a) variation of Ca and Mg concentrations with time and b) variation of* $[Mg^{2+}]_{diss}$ *concentration and pH with time.*

R_{diss} of calcite and R_{ppt} of gypsum from the experiment run with calcite (Iceland spar) powder were also calculated at two different pH intervals (Table 4.2), showing that the rates were similar to those obtained with the substrate made of limestone 1-2 mm grains. The dissolution rates for all experiments were normalized to the geometric surface area (mol cm^{-2} s^{-1}; Table 4.2) to enable a comparison with the rates of calcite and dolomite reported in the literature (e.g., Morse and Arvidson, 2002; Atanassova et al., 2013; Xu et al., 2013). Figure 4.12 shows significantly slower dissolution rates at low pH in this study than those of calcite and dolomite from the literature (far-from-equilibrium conditions). The rates obtained in the performed batch experiments were likely slowed down by two processes inherent to a system where a $CaCO_3$ substrate controls the coupled reactions: diffusion of solutes (Ca^{2+}, H_2CO_3, H^+) between the carbonate substrate surface and the bulk solution that limits the dissolution of calcite (transport control), and formation of gypsum coatings upon the substrate surfaces that reduces the reactive surface area.

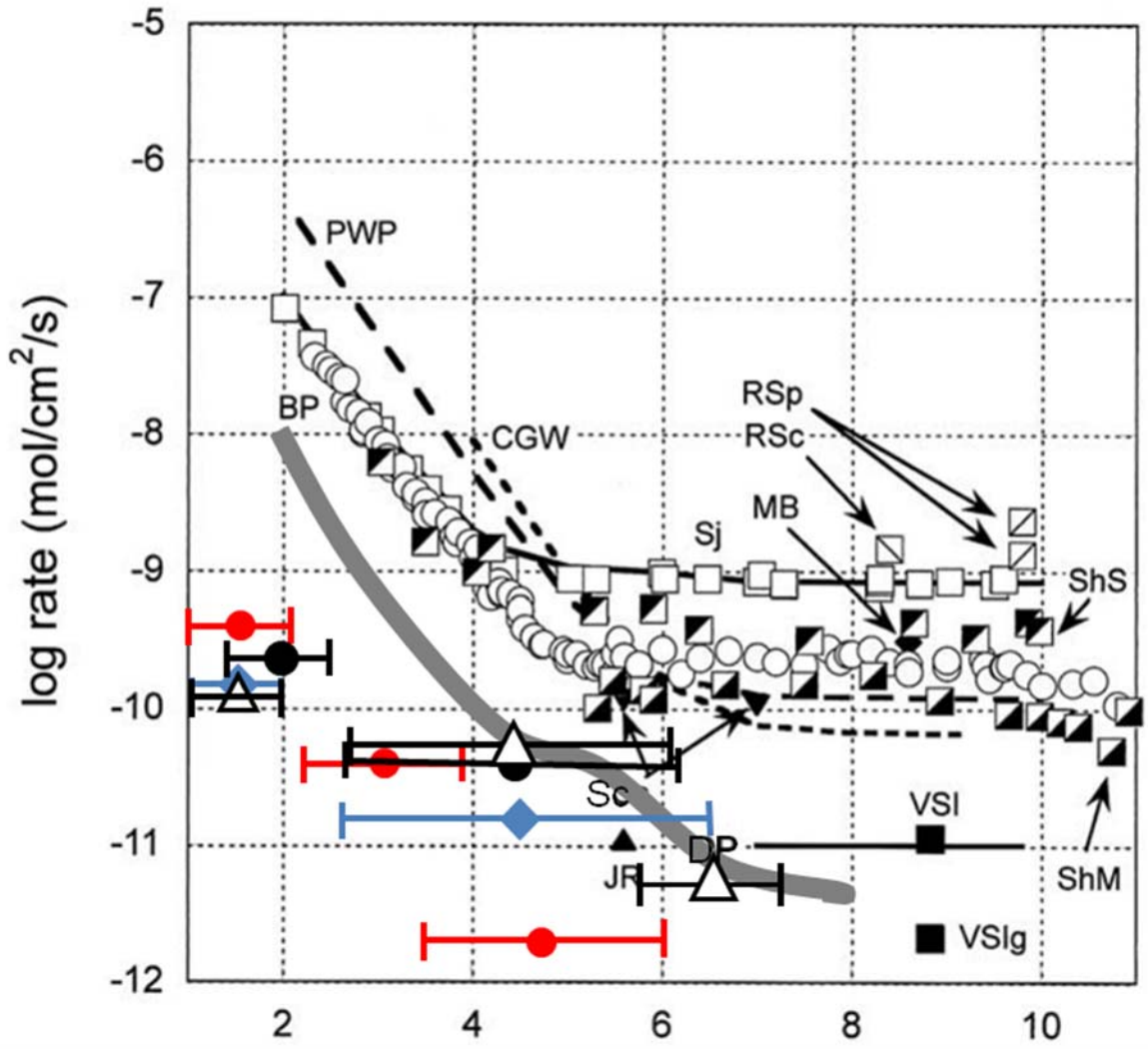

Figure 4.12 *log dissolution rates of Ca-carbonate minerals versus pH obtained in this study [red solid circle = aragonite; black solid circle = limestone; empty triangle = Iceland spar; blue solid rhomb = dolostone] and from literature (modified from Arvidson et al., 2003 and Morse and Ardvison, 2002) [dolomite: grey solid line; aragonite: CGW = Chou et al. (1989); calcite: Sj = Sjöberg (1978); RSp = Rickard and Sjöberg (1983); RSc = Rickard and Sjöberg (1983); PWP = Plummer et al. (1978); CGW) = Chou et al. (1989); BP = Busenberg and Plummer (1986); MB = MacInnis and Brantley (1992); Sc = Schott et al. (1989); ShM = Shiraki et al. (2000); solid line with no symbol, DP = Dove and Platt (1996); JR = Jordan and Rammensee (1998); VSI = Arvidson et al. (2003)].*

4.4 Summary and conclusions

Batch experiments were performed to obtain information on the kinetics of the coupling between carbonate mineral dissolution and gypsum precipitation.

In solutions of pH 2 (H_2SO_4) in equilibrium with respect to gypsum, where samples of $CaCO_3$ minerals with different size dissolved, the induction time of gypsum

precipitation at the expense of calcite or aragonite dissolution was similar and independent of the initial geometric surface area of the substrate. Also for the one of dolostone dissolution, where calcite dissolution dominated over dolomite dissolution.

The dissolution rates of calcite, aragonite and dolomite reduced from the far-from equilibrium rates under acidic conditions due to the diffusive transport of solutes (Ca^{2+}, H_2CO_3 and H^+) close to the substrate surface and passivation of the surface as gypsum precipitated (see Chapter 5). The precipitation rates were slower by a factor range of 0.3-0.8 than those of $CaCO_3$ dissolution, indicating that the rate of gypsum precipitation depended on the rate of Ca release. This fact makes the general rate law to describe gypsum growth as a function of pH reported by Rosenberg et al. (2012) difficult to apply in systems where the gypsum growth occurs upon $CaCO_3$ substrates.

The experimental results point out similar reactivity between calcite and aragonite, which suggests similar behavior of both minerals as a backfilling material in the passive treatments of AMD.

Chapter 5†

Direct nanoscale observations of the coupled dissolution of calcite and dolomite and gypsum precipitation

5.1 Introduction

In this chapter it is attempted to enhance the current knowledge on the complementary processes of calcite/dolomite dissolution and gypsum precipitation. Two types of solution were used: (1) acid sulfate solution (Na_2SO_4) undersaturated with respect to gypsum and (2) acid sulfate solution ($CaSO_4$) equilibrated with respect to gypsum. The experimental pH ranged from approximately 2 to 6 and the *in situ* AFM experiments were run at ambient temperature (23 ± 1°C) and pressure.

5.2 Materials and methods

The experiments were carried out using a Digital Instruments (Bruker) Nanoscope III AFM equipped with a fluid cell sealed with an O-ring (50 μL volume), in contact mode using Si_3N_4 tips (Bruker, NP-S20) at room temperature (23 ±1 °C). The scanning frequency was ≈3 Hz and image resolution was of 256 lines per scan, giving an average

† the present chapter is based on the paper *Direct nanoscale observations of the coupled dissolution of calcite and dolomite and the precipitation of gypsum* by Francesco G. Offeddu, Jordi Cama , Josep M. Soler and Christine V. Putnis in Beilstein Journal of Nanotechnology. 2014, 5, 1245–1253.

scan time of 1 image every ≈ 100 seconds. Scan size ranged from 1x1 μm^2 to 15x15 μm^2. Images were analyzed with WSxM free software(Horcas et al., 2007).

Single fragments of calcite (Iceland Spar, Chihuahua, Mexico) and crystalline dolomite (Eugui, Navarra, Spain) of approximately 4 x 3 x 1 mm (crystal volume ≈ 12 mm^3) were cleaved immediately prior to experiments, attached with commercial Conductive Carbon Cement (CCC) to a fixed and oriented Teflon holder and mounted in the fluid cell. The cleavage surface of calcite and dolomite is the (104) surface.

Acid solutions were prepared immediately before the experiments adding the appropriate amounts of reactive analytical grade, $CaSO_4 \cdot 2H_2O$ (Merck pro analysis) and Na_2SO_4 (Grüssing purity 98%), to Millipore MQ water (resistivity = 18 MΩ cm) (Table 5.1). Solution pH was adjusted to the chosen pH (approximately from 2 to 6) by adding concentrated H_2SO_4. pH measurements were carried out using a InoLab pH meter, equipped with a WTW Sentix 21 electrode calibrated with an accuracy of ± 0.02 pH units. The electrode was calibrated with Crison buffer solutions at pH 4 and 7. The saturation index (SI) with respect to gypsum and calcite of the input solutions was calculated using the PhreeqC code and the PhreeqC database (Parkhurst and Appelo, 2013).

Table 5.1 *Initial experimental conditions*

experiment	substrate	pH	electrolite	Ca_{inp} (mol L^{-1})	Na_{inp} (mol L^{-1})	SO_{4inp} (mol L^{-1})	SI calcite	SI gypsum
cal14	calcite	2.23	Na_2SO_4		5.42E-02	3.10E-02	-	-
cal12	calcite	2.20	Na_2SO_4		4.62E-02	2.70E-02	-	-
cal9	calcite	2.18	$CaSO_4$	1.60E-02	-	2.50E-02	-11.04	0.05
cal10	calcite	2.18	$CaSO_4$	1.60E-02	-	2.50E-02	-11.04	0.05
dol6	dolomite	2.11	Na_2SO_4		1.02E-02	1.00E-02	-	-
dol3	dolomite	2.11	Na_2SO_4		2.62E-02	1.80E-02	-	-
dol4	dolomite	2.18	$CaSO_4$	1.60E-02	-	2.50E-02	-11.04	0.05
dol1	dolomite	2.14	Na_2SO_4		5.02E-02	3.00E-02	-	-
cal19	calcite	3.37	Na_2SO_4		5.56E-02	2.70E-02	-	-
cal8	calcite	3.06	$CaSO_4$	1.50E-02	-	1.60E-02	-9.22	0.00
cal21	calcite	2.92	Na_2SO_4		1.12E-02	6.00E-03	-	-
dol5	dolomite	3.00	$CaSO_4$	1.50E-02	-	1.60E-02	-9.22	0
dol7	dolomite	3.00	Na_2SO_4		2.70E-02	1.40E-02	-	-
cal4	calcite	4.08	$CaSO_4$	1.50E-02	-	1.50E-02	-7.18	-0.01
cal2	calcite	4.03	Na_2SO_4		1.12E-02	6.00E-03	-	-
cal6	calcite	4.80	$CaSO_4$	1.50E-02	-	1.50E-02	-5.77	-0.02
cal3	calcite	5.82	$CaSO_4$	1.50E-02	-	1.50E-02	-3.73	-0.02

The experimental strategy consisted of three stages. First, prior to each *in situ* experiment an *in air* image of a selected region of the cleaved surface was taken to examine the initial topography and surface features of interest (flat/rough areas, steps terraces and edges; Figs. 5.1a, d). Secondly, after an appropriate region of the cleavage surface was selected, the Millipore MQ water was injected using a syringe to fill the available volume of the fluid cell containing the sample (≈ 38 μL) and flow over the mineral surface. Renovation of the Millipore MQ water was performed after each sequential image capture (≈ 1.5 min) to ensure similar bulk solution concentration as the reaction took place during the experiment and prevent the effect of solution saturation state on the reaction (close-to-equilibrium approach). During this stage the calcite dissolution rate, R_{AFM} (mol $cm^{-2}s^{-1}$), was obtained from the dissolved volume of calcite created by the etch pits (as described by Urosevic et al. (2012)):

$$R_{AFM} = \Delta V \cdot N_{pit} / V_{cal} \cdot (t_2 - t_1) \quad (5.1)$$

$$\Delta V = (w_2 \cdot u_2 - w_1 \cdot u_1) \cdot h \quad (5.2)$$

where ΔV is the increase in dissolved volume of an etch pit between t_2 and t_1 in two sequential images, *w, u and h* are the etch pit's width, length and depth, respectively (h remains constant, ca. 0.3 nm), N_{pit} is the average number of etch pits per cm^2, and V_{cal} is the molar volume of calcite (31.20 cm^3 mol^{-1}). Using sequential time images, the pit expansion rate, R_s (nm s^{-1}), was also calculated from the variation in length of the etch pit sides (Δw or Δu) with time ($R_s = \Delta w/(t_2 - t_1)$). Likewise the step velocity, R_T (nm s^{-1}), was calculated from the increase in length of terrace width (ΔL) with time ($R_T = \Delta L/(t_2 - t_1)$). After conclusion of mineral dissolution in Millipore MQ water, the third stage started as the cell was filled with the chosen sulfate-rich acid solution in order to promote the precipitation of gypsum. During this stage, solution renovation was not allowed. Hence, the solution saturation state approached equilibrium with respect to the dissolving carbonate mineral.

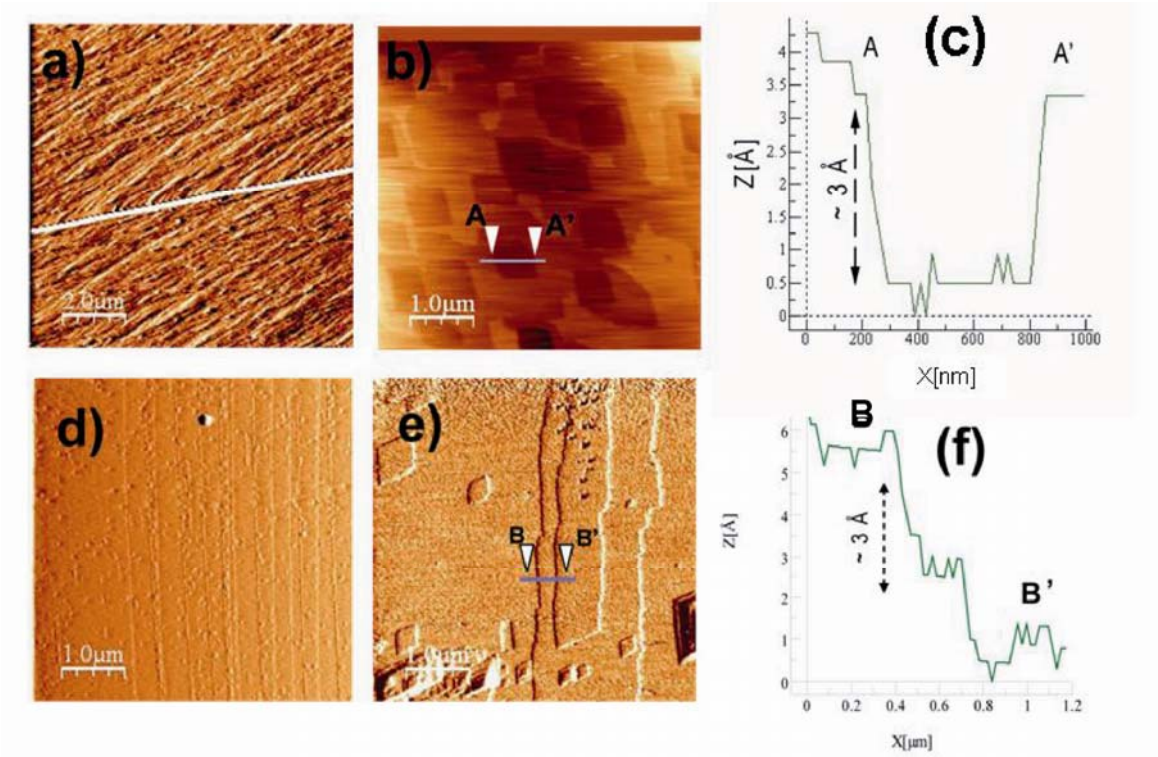

Figure 5.1 *AFM deflection images of calcite cleavage surfaces. Top row: a) image in air shows the initial flat surface with a topographic variation that ranges 2 nm. White line across the image corresponds to a terrace; b) same surface region with some drift after 300 s in Millipore MQ water showing a high density of etch pits homogeneously distributed and c) depth profile of an etch pit section. Bottom row: d) image in air shows the initial flat surface with a topographic variation that ranges 4 nm and e) same surface region after 240 s in Millipore MQ water showing random formation of etch pits and f) depth profile of a step edge section shown by arrows in e).*

Micro-Raman analysis was used to identify the newly precipitated sulfate phases on the calcite and dolomite cleavage surfaces. Micro-Raman spectra were obtained using a dispersive spectrophotometer Jobin-Yvon LabRam HR 800 with 532 nm light for sample excitation and CCD detector cooled at -70º C. Laser power used was between 0.5 and 4 mW. The spectrophotometer was coupled to optic microscopy Olympus BXFM with 50x and 100x objectives. Samples were dried before measurement.

5.3 Results and discussion

5.3.1 Dissolution of calcite

Dissolution of the (104) calcite surface in Millipore MQ water was readily observed. Figs. 5.1b, c show the formation of shallow (depth of ≈ 0.3 nm ≈ calcite unit cell) and deep rhombohedral etch pits over the surface (Atanassova et al., 2013; Harstad and Stipp, 2007; Ruiz-Agudo and Putnis. 2012; MacInnis,.and Brantley, 1992). The ratio between the etch pit rhombus diagonals was 0.71 ± 0.02, which is similar to that reported by Pérez-Garrido et al. (2007). Etch pit merging and formation of trenches or steps were observed (Figs. 5.1b,e). The number of etch pits per square centimeter of surface (N_{pit}) varied from 8 x 10^7 (only etch pits, Fig. 5.1b) to 5 x 10^8 (etch pits and steps, Fig. 5.1e) in scanned flat regions with similar initial roughness. The measured calcite dissolution rate, R_{AFM}, was 1.45 x 10^{-10} mol cm^{-2} s^{-1}, which agrees with that at nearly neutral pH reported elsewhere (Atanassova et al., 2013; Duckworth and Martin, 2004; De Giudici, 2002). The etch pit expansion rate, R_s, was measured to be 1.82 ± 0.12 nm s^{-1} and falls within the range of those calculated in deionized water by Jordan and Rammensee (1998) (velocity of slow step 0.5 ± 0.2 nm/s and of fast steps 2.5 ± 0.5 nm/s).

Interaction between the acidic sulfate-rich solutions and the calcite cleavage surface (solution injected and not renewed) induced faster dissolution than in Millipore MQ water. A massive nucleation of new rhombohedral etch pits took place at pH 4.80 after solution injection, in contrast to the fairly regular distribution of etch pits in Millipore MQ water (Fig. 5.2). At pH 4.80 R_{AFM} was 5.50 x 10^{-10} mol cm^{-2} s^{-1}, which is faster than that at pH 7, and agrees with the expected rate at pH 5 and 25 °C (e.g., (Atanassova et al., 2013)).

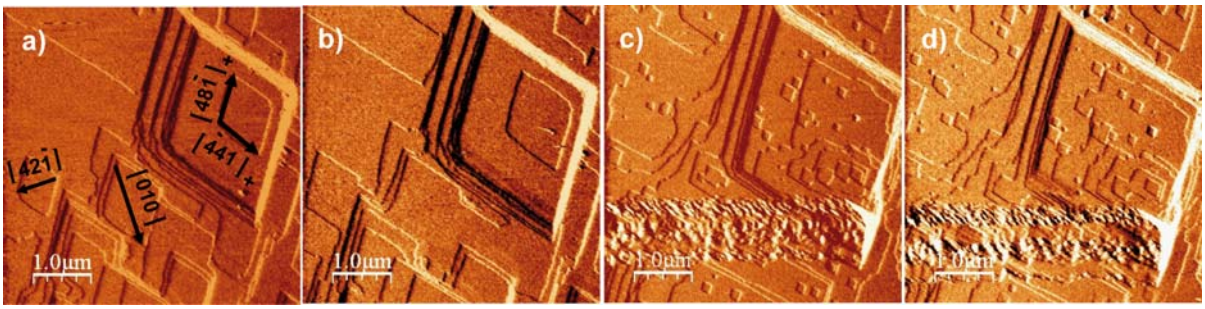

Figure 5.2 *Sequential AFM deflection images of the reacted calcite (104) surface: initially in Millipore MQ water (after 14 minutes (a) and 19 minutes (b) from MQ water injection) and acid solution (pH 4.80) (after 3 minutes (c) and 5 minutes(d) from acidic injection). Etch pits developed and spread. As pH was decreased to 4.80, a large population of etch pits suddenly formed. Rhombohedra formed along the [48$\bar{1}$]+ and [$\bar{4}$41]+ directions with the long and short diagonals parallel to [010] and [42$\bar{1}$], respectively.*

In the experiments with Na_2SO_4 solution (Fig. 5.3a; solution injected and not renewed) dissolution of the calcite cleavage surface was taking place such that equilibrium with respect to calcite was being approached. It was observed that the shape of newly formed rhombohedral etch pits was changing with time as the solution approached equilibrium with respect to calcite. The evolving shape was characterized by rounding of the obtuse-obtuse corner (Fig. 5.3b, c, d). According to Teng et al. (1999) and Teng (2004) the retreat velocities of acute and obtuse steps do not show linear dependence on supersaturation. In addition, several studies have shown that velocities of acute and obtuse step spreading have different sensitivities to solute activity ratios in solution (Larsen et al., 2010; Ruiz-Agudo and Putnis, 2012; Stack and Grantham, 2010). Calcite dissolution continuously took place during the solution saturation state drift. This implies a change in Gibbs energy along the experimental runs. As pointed out by Stipp et al. (1994) and De Leeuw et al. (1999), the observed distortion of the etch pit shape (figs. 5.3b,c) likely corresponds to an increase in the difference of velocities between obtuse and acute steps.

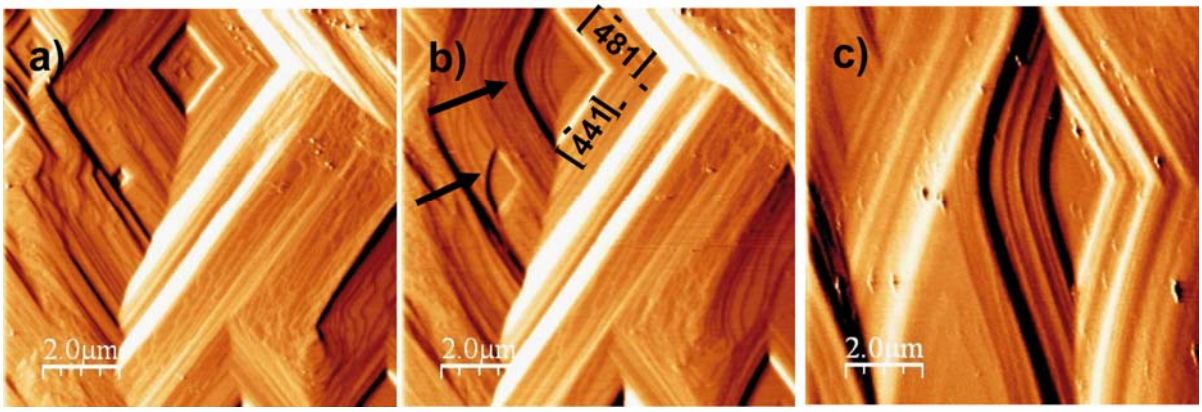

Figure 5.3 *Sequential AFM deflection images of the reacted calcite cleavage surface in contact with Na_2SO_4 solution: a) characteristic morphology of rhombohedral etch pits (after acid injection, pH 4.08) and b) rounding of the obtuse-obtuse corner of the rhombohedral etch pits (shown by arrows) after 12 min, and c) rhombohedral etch pit with elongated shape after 43 min with a short/long diagonal ratio of 0.35 ± 0.02.*

5.3.2 Dissolution of dolomite

Dolomite dissolution experiments were carried out similarly to those of calcite. First, dolomite dissolved in Millipore MQ water, and then, the reaction took place in sulfate-rich solutions at pH 2 and 3 (Table 5.1). Contrary to calcite dissolution, when dolomite reacted in Millipore MQ water, nucleation of etch pits was not observed for approximately 25 min. Only, at specific surface localities, step retreat was observed (Fig. 5.4a), allowing the calculation of the retreat velocity R_S, considered to be the average retreat velocity of non-crystallographically equivalent steps (Fig. 5.4b and c), which was 0.14 ± 0.03 nm s^{-1}. This value is not far from the etch spreading rate of 0.09 ± 0.01 nm s^{-1} reported by Urosevic et al. (2012) and is about one order of magnitude lower than the etch pit expansion rate of calcite obtained in this study.

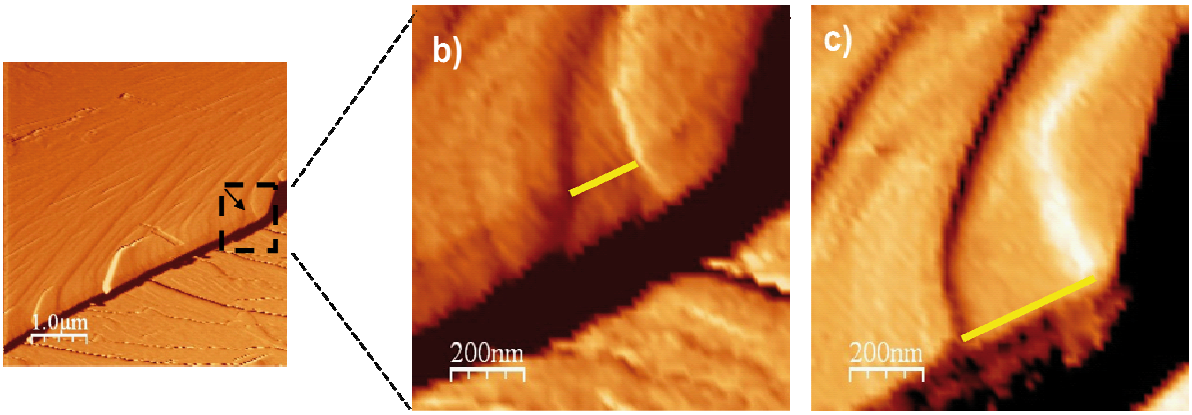

Figure 5.4 *AFM deflection images of dolomite dissolution in Millipore MQ water: a) in air image of the dolomite (010) surface (exp. dol 1 in Table 5.1). Selected squared region in (a) to calculate the step-retreat rate based on the variation in length with time of the pointed terrace. The sequential images in b) and c) after 7.5 and 11.5 respectively, show the consequent terrace evolution.*

As dolomite reacted in acid solution, etch pit nucleation of isolated etch pits was observed over the cleavage surface after 10 min. Single etch pits presented an elongated rhombohedral shape (Fig. 5a). As the surface kept dissolving for 8 h, etch pit nucleation occurred all over the surface. Lack of sequential images for this long run prevented us calculating R_{AFM} under acid conditions (Fig. 5b). The formed etch pits showed the typical rhombohedral shape as expect from carbonate mineral dissolution (Urosevic et al., 2012).

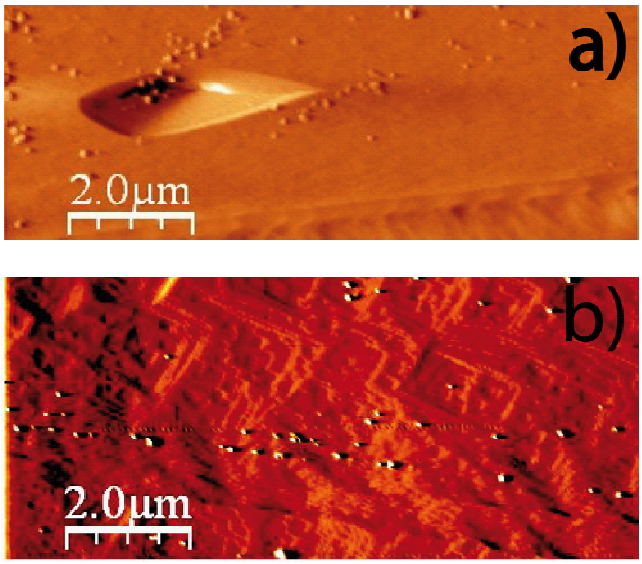

Figure 5.5 *AFM deflection images of the reacted dolomite (104) cleavage surface in acid Na_2SO_4 solutions: a) after 10 min in pH 2, isolated etch pits were observed and b) in pH 3, nucleation of etch pits was observed all over the surface after 8 h.*

5.3.3 Coupled dissolution of calcite and dolomite and gypsum precipitation

As the calcite (104) cleavage surface reacted with the pH 2 solution equilibrated with respect to gypsum, gypsum precipitation was readily observed (Fig. 5.6). Micro-Raman analyses of the retrieved reacted samples confirmed the presence of gypsum. Gypsum nucleation took place uniformly all over the calcite surface immediately after the acid solution interacted with the dissolving cleavage surface (Figs. 6a,b). At pH 2, the gypsum precipitation induction time was slower than 100 s (time between two sequential image captures). The epitaxially grown gypsum crystals displayed an elongated (arrow-like) shape, consistent with their crystallographic monoclinic form, usually presented as tabular crystals, with the long and short sides parallel to the calcite [$\bar{4}41$] and [481] directions, respectively (Figs. 5.6a,c).

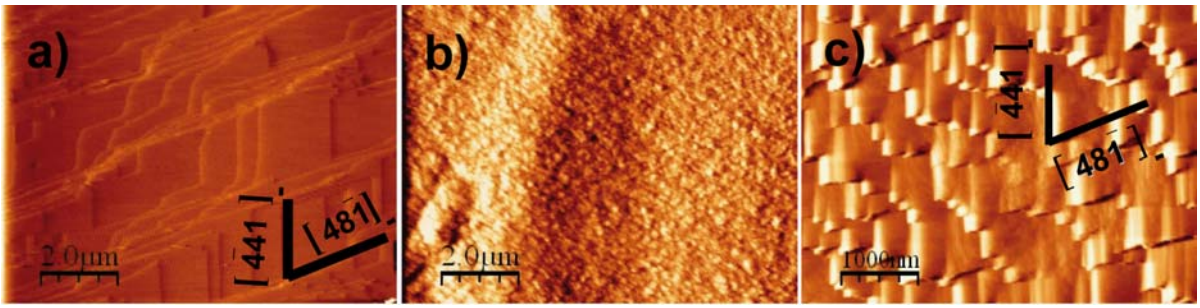

Figure 5.6 *AFM deflection images of reacting (104) calcite surface: a) dissolution in Millipore MQ water; b) after injecting a solution in equilibrium with gypsum at pH 2.18, gypsum precipitation starts (1.5 min) and c) gypsum arrows grow laterally and coalesce (41 min).*

This crystal morphology was observed by Booth et al. (1997). 3-D images of the arrow-shaped gypsum crystals showed that the formed gypsum crystals, which coated entirely the cleavage surface, were slightly tilted (~1º) with respect to the calcite (104) cleavage surface. The lack of a reference surface on the calcite substrate and the fast-formed gypsum coating prevented calculation of gypsum growth rates at the pH range studied. Gypsum precipitation ceased as Ca release from calcite dissolution stopped. This was most likely because calcite dissolution stopped as either the entire calcite surface was

totally passivated impeding ion release through the gypsum layer, or because equilibrium with respect to calcite was achieved.

In experiments where calcite dissolved at pH ≥ 3 in gypsum equilibrated solutions, the gypsum induction time was longer than 240 s, indicating slower gypsum growth than that at pH 2 due to slower calcite dissolution. Gypsum also grew epitaxially over the entire surface and, in general, the crystals showed the arrow-like shape (Fig. 5.7 a). In some Na_2SO_4 experiments, however, gypsum precipitation occurred non-uniformly over the cleavage surface, taking place at specific localities, mostly at step edges, and forming individual protuberances (spikes), suggesting preferential sites for the formation of these nuclei (Fig. 5.7 b).

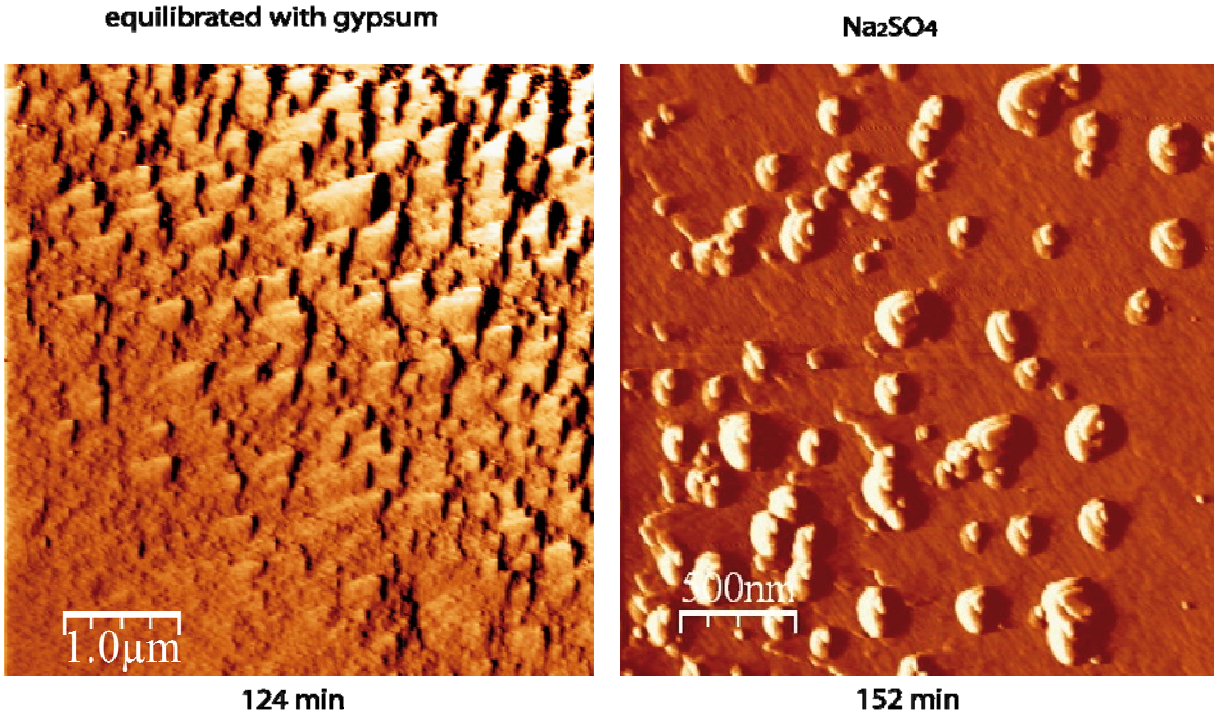

Figure 5.7 *Gypsum precipitation on a calcite surface at pH 3: a) Experiment with gypsum equilibrated $CaSO_4$ solution homogeneous, arrow-type gypsum growth on the cleavage calcite surface; b) Experiment with Na_2SO_4 solution, random protuberances over the calcite surface.*

When the cleaved dolomite surface was the substrate, gypsum precipitation from dolomite dissolution was slower than that from calcite dissolution at the same pH. Micro-Raman analyses of the reacted fragments at pH 2 and 3 confirmed precipitated gypsum on the dolomite cleavage surfaces. Gypsum precipitation occurred on the

previously etch pitted dolomite surface after about 6 h, and again it was difficult to establish an induction time. Epitaxial growth was observed to be non-uniform over the surface (Fig. 5.8), taking place on preferential surface regions, such as step and terrace edges, and areas with marked roughness. This behavior suggests that gypsum precipitation on dolomite cleavage surfaces was favored at highly reactive surface regions, where dolomite dissolution and hence element release was highest. After 8 h of reaction time, dolomite passivation was still only partial with etch pitted regions still visible, contrasting with the full gypsum armouring on the calcite surface.

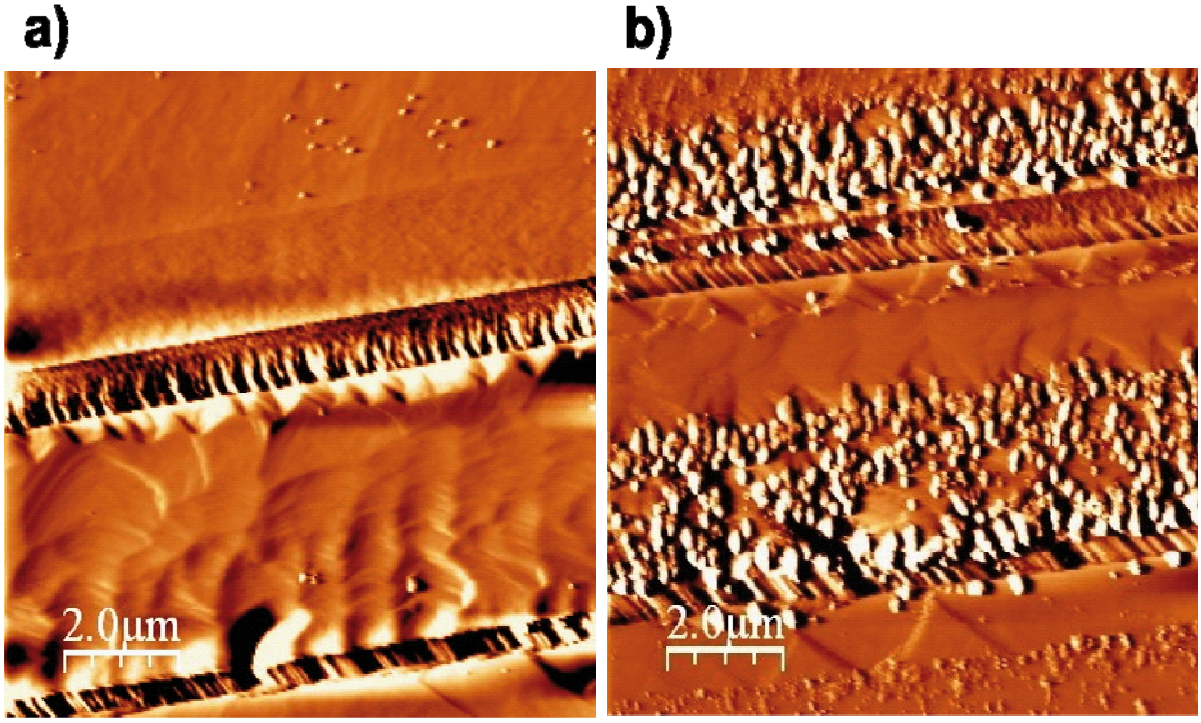

Figure 5.8 *Sequential AFM deflection images of reacted dolomite surface in pH 3 (H_2SO_4) in solution equilibrated with respect to gypsum: a) after 4 h, shallow and deep etch pits are visible on the dolomite surface and b) after 6 h, gypsum precipitated mainly along the step edges.*

5.4 Summary and conclusions

In situ Atomic Force Microscopy was used to investigate the coupled processes of carbonate mineral dissolution and gypsum precipitation in acid sulfate-rich solutions in solutions both undersaturated and in equilibrium with respect to gypsum at room temperature.

Dissolution of calcite and dolomite occurred forming the characteristic rhombohedral etch pits. Calcite dissolution rates measured at nearly neutral pH and pH of 4.80 agreed with VSI-measured rates (Atanassova et al., 2013). The calcite etch pit expansion rate and the dolomite step retreat velocity were calculated in near neutral pH (Millipore MQ water), the latter being about one order of magnitude lower than the former.

Gypsum precipitation occurred as a result of the carbonate mineral dissolution. Therefore, as in acidic pH conditions calcite dissolution rates were faster than those of dolomite, gypsum precipitation was correspondingly faster in the calcite dissolution experiments. Epitaxial growth was the growth mechanism as observed by Booth et al. (1997), and gypsum nucleation induction times were shorter in the calcite dissolution experiments.

In the case of calcite dissolution in gypsum-equilibrated solutions, gypsum nucleation occurred immediately and surface coating was uniform all over the calcite surface, yielding total calcite passivation. Arrow-shaped gypsum crystals evolved along the etch pit crystallographic directions ($[\bar{4}41]$ and [-481]). In solutions undersaturated with respect to gypsum (Na_2SO_4), precipitation occurred via the formation of isolated growth protuberances, randomly distributed over the cleavage surface.

In the case of dolomite dissolution in gypsum-equilibrated solutions, gypsum precipitation was favored at high reactive surface regions (step and terrace edges) and rough regions. Gypsum partially coated the dolomite surface during the experimental runs.

In all experiments gypsum precipitation resulted from a two-step process: 1. The calcite or dolomite dissolved, as observed in the regular formation of rhombohedral etch pits and step retreat, thereby releasing Ca^{2+} or Ca^{2+} and Mg^{2+} ions to solution. 2. The solution at the mineral-solution interface became supersaturated with respect to gypsum, which then precipitated. These two processes were coupled at the interface and continued while Ca^{2+} was being released.

Part III:

Conclusions

Chapter 6

General conclusions

The main conclusions of this thesis are:

1) Regarding the efficiency of the Ca-carbonate minerals in the AMD treatment (**column experiments**):

- Calcite passivation by gypsum coating is an important limitation to the limestone buffer capacity, and the main factors for controlling passivation time were the initial sulfate concentration and pH. A decrease in sulfate concentration enhances the column passivation time. Likewise, by increasing the solution pH, together with a decrease in flow rate, passivation time also improved.

- Metal retention does not show the same trends as passivation time: there is little sensitivity of metal retained on initial sulfate (and metal) concentration due to the negative correlation between initial concentration and passivation time.

- The formation of preferential paths and clogging is another limitation for the treatment efficiency. These complementary phenomena are caused by the precipitation of iron or aluminum oxyhydroxides which impede homogeneous circulation of the solutions through the columns. To improve the efficiency in the passive treatment, mixtures of calcite grains and glass beads were used to pack the columns. The addition of an inert substrate clearly improves the efficiency.

- mCT and mXRD measurements revealed that precipitation of gypsum coating and metal-oxyhydroxide occurred simultaneous. Porosity variation along the columns was quantified. Porosity decreased progressively with time. Gypsum coating contributed 5% in porosity reduction, whereas goethite contribution was ~15%.

- A good match between limestone experimental results and reactive transport simulations was achieved. Fitting of the results required a reduction in the reactive surface area of calcite with time, which is consistent with a passivation mechanism (formation of gypsum coatings on calcite surfaces).

- The efficiency of aragonite and dolostone (dolomite) in passive treatment of sulfate-reach acid waters is fairly comparable to that of limestone.

- Passivation of aragonite and dolomite by gypsum precipitation (coating) and the formation of preferential flow paths limits the efficiency of the columns. The negative correlation between the initial sulfate (and metal) concentration and passivation time also affects the efficiency.

- Porosity decrease is strongly linked to formation of preferential flow paths; porosity loss was between 7 % and 5% for aragonite and dolostone experiments, respectively.

2) Regarding the coupled reactions of carbonate mineral dissolution and gypsum precipitation (**batch and in-situ AFM experiments**):

- In batch experiments where samples of $CaCO_3$ minerals (calcite and aragonite) with different size (powder, grains and fragments) dissolved in solutions of pH 2 in equilibrium with respect to gypsum, the induction time of gypsum precipitation at the expense of calcite or aragonite dissolution was similar and independent of the initial geometric surface area of the substrate.

- The dissolution rates of calcite, aragonite and dolomite reduced from the far-from-equilibrium rates due to the diffusive transport of Ca from the substrate surface and passivation of the surface as gypsum precipitated. The precipitation rates were slower by a factor range of 0.3-0.8 than those of $CaCO_3$ dissolution, indicating that the rate of gypsum precipitation depended on the rate of Ca release. This fact makes the general rate law to describe the gypsum growth as a function of pH reported by Rosenberg et al. (2012) hardly applicable in systems where the gypsum growth occurs upon $CaCO_3$ substrates.

- The similar reactivity observed between calcite and aragonite suggests similar behavior of the two studied $CaCO_3$ polymorphs as a backfilling material in the passive treatments of AMD. This fact is in accordance with the results obtained in the column experiments.

- In situ Atomic Force Microscopy observations showed that dissolution of calcite and dolomite occurred forming the characteristic rhombohedral etch pits. Calcite dissolution rates measured at nearly neutral pH and pH of 4.80 agreed with VSI-measured rates (Atanassova et al, 2013). The calcite etch pit expansion rate was one order of magnitude faster than the dolomite step retreat velocity in near neutral pH.

- Gypsum precipitation occurred as a result of the carbonate mineral dissolution. Therefore, as in acidic pH conditions calcite dissolution rates were faster than those of dolomite, precipitation was correspondingly faster in the calcite dissolution experiments. Epitaxial growth was the growth mechanism as observed by Booth et al. (1997), and gypsum nucleation induction times were shorter in the calcite dissolution experiments.

- In the case of calcite dissolution in gypsum-equilibrated solutions, gypsum nucleation occurred immediately and surface coating was uniform all over the calcite surface, yielding total calcite passivation. Arrow-shaped gypsum crystals evolved along the etch pit crystallographic directions ($[\bar{4}41]$ and $[\bar{4}81]$). In solutions undersaturated with respect to gypsum (Na_2SO_4), precipitation occurred via the formation of isolated growth protuberances, randomly distributed over the cleavage surface.

- In the case of dolomite dissolution in gypsum-equilibrated solutions, gypsum precipitation was favored at high reactive surface regions (step and terrace edges) and rough regions. Gypsum partially coated the dolomite surface during the experimental runs.

- In all experiments gypsum precipitation resulted from a two-step process: 1. The calcite or dolomite dissolved, as observed in the regular formation of rhombohedral etch pits and step retreat, thereby releasing Ca^{2+} or Ca^{2+} and Mg^{2+} ions to solution. 2. The solution at the mineral-solution interface became

supersaturated with respect to gypsum, which then precipitated. These two processes were coupled at the interface and continued while Ca^{2+} was being released.

References

Allison, J.D., Brown, D.S. Novo-Gradac, K., 1991. MINTEQA2/PRODEF2, A Geochemical Assessment Model for Environmental Systems: Version 3.0 User's Manual, EPA/600/3-91/021 Athens, GA, 30605: EPA (USA).

Amira 5.2 3D visualization software, Visage Imaging, Berlin, Germany (www.amira.com).

Arvidson, R.S., Collier, M., Davis, K.J., Vinson, M.D., Amonette, J.E., Luttge, A., 2006. Magnesium inhibition of calcite dissolution kinetics. Geochim. Cosmochim. Acta 70, 583-594.

Arvidson, R.S., Ertan, I.E., Amonette, J.E., Luttge, A., 2003. Variation in calcite dissolution rates:A fundamental problem? Geochim. Cosmochim. Acta 67, 1623-1634.

Astilleros, J.M., Fernández-Díaz, L., Putnis, A., 2010. The role of magnesium in the growth of calcite: An AFM study. Chem. Geol. 271, 52-58.

Atanassova, R.A., Cama, J., Soler, J..M., Offeddu, F.G., Queralt, I.G., 2013. Calcite interaction with acidic sulphate solutions: a vertical scanning interferometry and energy-dispersive XRF study. Eur. J. Min. 25, 331-351.

Bigham, J.M., Schwertmann, U., S.J., T., Winland, R.L., Wolf, M., 1996. Schwermannite and the chemical modelling of iron in acid sulphate waters. Geochim. Cosmochim. Acta 60, 2111-2121.

Blowes, D. W., Ptacek, C. J., 2003. The Geochemistry of Acid Mine Drainage. In: Lollar, .S. (Ed.), Environmental Geochemistry, Treatise of Geochemistry 9, 149-204 Elsevier, Toronto, Canada.

Booth, J., Hong, Q., Compton, R., Prout, K., Payne, R., 1997. Gypsum overgrowths passivate calcite to acid attack. J. Colloid Interf. Sci. 192, 207-214.

Brown, G.E., Calas G., 2011. Environmental mineralogy – Understanding element behavior in ecosystems, Comptes Rendus Geosci. 343, 90-112.

Busenberg, E., Plummer, L. N., 1986. A comparative study of the dissolution and precipitation kinetics of calcite and aragonite. In Studies in Diagenesis. (ed. F. A. Mumpton), pp. 139-168. U.S. Geological Survey Bulletin.

Caraballo, M. A., Macias, F., Nieto, J. M., Castillo, J., Quispe, D., Ayora, C., 2011. Hydrochemical performance and mineralogical evolution of a dispersed alkaline substrate (DAS) remediating the highly polluted acid mine drainage in the full-scale passive treatment of Mina Esperanza (SW Spain). Am. Min. 96, 1270-1277.

Caraballo, M. A., Rötting, T. S., Macías, F., Nieto, J.M. and Ayora C., 2009a. Field multi-step limestone and MgO passive system to treat acid mine drainage with high metal concentrations. Appl. Geochem. 24, 2301-2311.

Caraballo, M. A., Rotting, T. S., Nieto, J. M., and Ayora, C., 2009b. Sequential extraction and DXRD applicability to poorly crystalline Fe- and Al-phase characterization from an acid mine water passive remediation system. Am. Min. 94, 1029-1038.

Chou, L, Garrels R.M., Wollast R., 1989. Comparative study of the kinetics and mechanisms of dissolution of carbonate minerals. Chem. Geol. 78, 269-282.

Cravotta III, C.A., 2003. Size and performance of anoxic limestone drains to neutralize acidic mine drainage. J. Environ. Qual. 32, 1277-1289.

Cravotta III, C.A., 2008. Dissolved metals and associated constituents in abandoned coal-mine discharges, Pennsylvania, USA. Part 1: Constituent quantities and correlations. Appl. Geochem. 23, 166-202.

Cravotta III, C., Trahan, M. K., 1999. Limestone drains to increase pH and remove dissolved metals from acidic mine drainage. Appl. Geochem. 14, 581-606.

De Giudici, G., 2002. Surface control vs. diffusion control during calcite dissolution/: Dependence of step-edge velocity upon solution pH. Am. Min. 87, 1279-1285.

De Leeuw, N.H., Parker, S.C., Harding, J.H., 1999. Molecular dynamics simulation of crystal dissolution from calcite steps. Phys. Rev. 60, 13792-13799.

Dierick M, Masschaele B; Van Hoorebeke L., 2004. Octopus, a fast and user-friendly tomographic reconstruction package developed in LabView. Measurement Sci. Technol. 15, 1366-1370.

Dove, P. M., Platt, F. M., 1996. Compatible real-time reaction rates for in situ imaging of mineral-water interactions using scanning force microscopy. Chem. Geol. 127, 331-338.

Duckworth, O.W., Martin, S.T., 2004. Dissolution rates and pit morphologies of rhombohedral carbonate minerals. Am. Min. 89, 553-563.

Evangelou, V.P., Zhang, Y.L., 1995. A Review: Pyrite Oxidation Mechanisms and Acid Mine Drainage Prevention. Critical Reviews in Environ. Sci. Technol. 25, 141-199.

Gazea B., Adam K., Kontopoulos A., 1996. A review of passive systems for the treatment of acid mine drainage, Min. Eng. 9, 23-42.

Gill, J. S., Nancollas, G. H., 1979. The growth of gypsum crystals on barite and calcite. Desalination 29, 247-254.

Hammarstrom, J.M., Sibrell, P.L., Belkin, H.E., 2003. Characterization of limestone reacted with acid-mine drainage in a pulsed limestone bed treatment system at the Friendship Hill National Historical Site, Pennsylvania, USA. Appl. Geochem. 18, 1705-1721.

Harstad, A. O., Stipp, S.L.S., 2007. Calcite dissolution: Effects of trace cations naturally present in Iceland spar calcites. Geochim. Cosmochim. Acta 71, 56-70.

Hedin, R.S., Watzlaf, G.R., Nairn, R.W., 1994. Treatment of Acid Mine Drainage with Limestone. J. Environ. Manage. 23, 1338-1345.

Hillner, P.E., Manne, S., Gratz, A.J., Hansma, P.K., 1992. AFM images of dissolution and growth on a calcite crystal. Ultramicroscopy 42-44, 1387-1393.

Horcas, I., Fernández, R., Gómez-Rodríguez, J.M., Colchero, J., Gómez-Herrero, J., Baro, a M., 2007. WSXM: a software for scanning probe microscopy and a tool for nanotechnology. Rev. Sci. Instrum. 78, 013705-1-8.

Huminicki, D.M.C., Rimstidt, J.D., 2009. Iron oxyhydroxide coating of pyrite for acid mine drainage control. Appl. Geochem. 24, 1626-1634.

Kagawa, M., Sheehan, M. E., Nancollas, G. H., 1981. The crystal growth of gypsum in an ammoniacal environment. J. Inorg. Nucl. Chem. 43, 917-920.

Jordan, G., Rammensee, W., 1998. Dissolution rates of calcite (10- 14) obtained by scanning force microscopy: Microtopography-based dissolution kinetics on surfaces with anisotropic step velocities. Geochim. Cosmochim. Acta 62, 941-947.

Larsen, K., Bechgaard, K., Stipp, S.L.S., 2010. The effect of the Ca2+ to activity ratio on spiral growth at the calcite surface. Geochim. Cosmochim. Acta 74, 2099-2109.

MacInnis, I.N., Brantley, S.L., 1992. The role of dislocations and surface morphology in calcite dissolution. Geochim. Cosmochim. Acta 56, 1113-1126.

Morse, J.W., Arvidson, R.S., 2002. The dissolution kinetics of major sedimentary carbonate minerals. Earth-Sci. Rev., 58, 51–84.

Nordstrom, D.K., Alpers, C.N., Ptacek, C.J., Blowes, D.W., 2000. Negative pH and Extremely Acidic Mine Waters from Iron Mountain, California. Environ. Sci. Technol. 34, 254-258.

Palandri, J.L., Kharaka, Y.K., 2004. A Compilation of Rate Parameters of Water–Mineral Interaction Kinetics for Application to Geochemical Modeling: U.S. Geological Survey Water-Resources Investigations Report 04-1068.70.

Parkhurst, D.L., Appelo, C.A.J., 2013. Description of input and examples for PHREEQC version 3--A computer program for speciation, batch-reaction, one-dimensional transport, and inverse geochemical calculations: U.S. Geological Survey Techniques and Methods, book 6, chap. A43, 497 p.

Pearson, F. H., Mc Donnell, A.J., 1975. Use of crushed limestone to neutralize acid wastes. J. Env Eng. Div. 101, 139-158.

Pérez-Garrido, C., Fernández-Díaz, L., Pina, C.M., Prieto, M., 2007. In situ AFM observations of the interaction between calcite surfaces and Cd-bearing aqueous solutions. Surf. Sci. 601, 5499-5509.

Pina, C.M., Pimentel, C., García-Merino, M., 2010. High resolution imaging of the dolomite (104) cleavage surface by atomic force microscopy. Surf. Sci. 604, 1877-1881.

Plummer, L.N., Wigley, T.M.L., Parkhurst, D. L., 1978. The kinetics of calcite dissolution in CO_2-water systems at 5° and 60°C and 0.0 to 1.0 atm CO_2. Am. J. Sci. 278, 179-216.

Reznik, I.J., Gavrieli, I., Antler, G., Ganor, J., 2011. Kinetics of gypsum crystal growth from high ionic strength solutions: A case study of Dead Sea – seawater mixtures. Geochim. Cosmochim. Acta 75, 2187-2199.

Reznik, I.J., Gavrieli, I., Ganor, J., 2009. Kinetics of gypsum nucleation and crystal growth from Dead Sea brine. Geochim. Cosmochim. Acta 73, 6218-6230.

Rickard, D. T., Sjöberg, E. L., 1983. Mixed kinetic control of calcite dissolution rates. Am. J. Sci. 283, 815-830.

Rosenberg, Y.O., Reznik, I.J., Zmora-Nahum, S., Ganor, J., 2012. The effect of pH on the formation of a gypsum scale in the presence of a phosphonate antiscalant. Desalination 284, 207-220.

Rötting, T.S., Caraballo, M. a., Serrano, J. A., Ayora, C., Carrera, J., 2008. Field application of calcite Dispersed Alkaline Substrate (calcite-DAS) for passive treatment of acid mine drainage with high Al and metal concentrations. Appl. Geochem. 23, 1660-1674.

Rötting, T.S., Thomas, R.C., Ayora, C., Carrera, J., 2005. Passive treatment of acid mine drainage with high metal concentrations using dispersed alkaline substrate. J. Environ. Qual. 37, 1741-1751.

Ruiz-Agudo, E., Kowacz, M., Putnis, C.V., Putnis, A., 2010. The role of background electrolytes on the kinetics and mechanism of calcite dissolution. Geochim. Cosmochim. Acta 74, 1256–1267.

Ruiz-Agudo, E., Putnis, C. V., 2012. Direct observations of mineral fluid reactions using atomic force microscopy: the specific example of calcite. Min. Mag. 76, 227-253.

Ruiz-Agudo E., Putnis C.V., Hövelmannb J., Álvarez-Lloret P., Ibáñez-Velasco A., Putnis A., 2015. Experimental study of the replacement of calcite by calcium sulphates. Geochim. Cosmochim. Acta, 156, 75-93.

Santomartino, S., Webb, J., 2007. Estimating the longevity of limestone drains in treating acid mine drainage containing high concentrations of iron. Appl. Geochem. 22, 2344-2361.

Santoro, L., Valpolicelli, G., Caprio, V., 1987. Limestone neutralization of acid waters in the presence of surface precipitates. Water Res. 21, 641-647.

Schneider, C.A., Rasband, W.S., Eliceiri, K.W., 2012. NIH Image to ImageJ: 25 years of image analysis. Nature Methods 9, 671-675.

Schott, J., Brantley, S., Crerar, D., Guy, C., Borcsik, M., Williame, C., 1989. Dissolution kinetics of strained calcite. Geochim. Cosmochim. Acta 53, 373-382.

Shindo, H., Ohashi, M., 1998. In-situ AFM observation of crystal growth of NaCl in an aqueous solution. Appl. Phys. A 66, 487-490.

Shiraki, R., Rock, P., Casey, W. H., 2000. Dissolution kinetics of calcite in 0.1 M NaCl solution at room temperature: An atomic force microscopic (AFM) study. Aqua. Geochem. 6, 87-108.

Sjöberg, E. L., 1978. Kinetics and mechanism of calcite dissolution in aqueous solutions at low temperatures. Stockholm Contribution in Geology, ISSN 0585-3532; 32:1.

Sjöberg, E.L., Rickard, D.T., 1984. Temperature dependence of calcite dissolution kinetics between 1 and 62°C at pH 2.7 to 8.4 in aqueous solutions. Geochim. Cosmochim. Acta 48, 485-493.

Sohnel, O., Mullin, J. W., 1988. Interpretation of crystallization induction periods. J. Colloid Interf. Sci. 123, 43-50.

Soler, J.M., Boi, M., Mogollon, J., Cama, J., Ayora, C., Nico, P., Tamura, N., Kunz, M., 2008. The passivation of calcite by acid mine water. Column experiments with ferric sulphate and ferric chloride solutions at pH 2. Appl. Geochem. 23, 3579-3588.

Stack, A.G., Grantham, M.C., 2010. Growth rate of calcite steps as a function of aqueous calcium-to-carbonate ratio: independent attachment and detachment of calcium and carbonate ions. Crystal Growth and Design 10, 1409-1413.

Steefel, C.I., Appelo, C.A.J., Arora, B., Jacques, D., Kalbacher, T., Kolditz, O., Lagneau, V., Lichtner, P.C., Mayer, K.U., Meeussen, J.C.L., Molins, S., Moulton, D., Shao, H., Šimůnek, J., Spycher, N., Yabusaki, S.B., Yeh, G.T., 2015. Reactive transport codes for subsurface environmental simulation, Comput. Geosci. 19, 445-478.

Stipp, S.L.S., Eggleston, C.M., Genkve, C.I., 1994. Calcite surface structure observed at microtopographic and molecular scales with atomic force microscopy (AFM). Geochim. Cosmochim. Acta 58, 3023-3033.

Teng, H.H., 2004. Controls by saturation state on etch pit formation during calcite dissolution. Geochim. Cosmochim. Acta 68, 253–262.

Teng, H.H., Dove, P.M., De Yoreo, J.J., 1999. Reversed calcite morphologies induced by microscopic growth kinetics: insight into biomineralization. Geochim. Cosmochim. Acta 63, 2507-2512.

Turner, D.R., McCoy, D., 1990. Anoxic alkaline drain treatment system a low cost acid mine drainage treatment alternative. In: Proc. 1990 Nat. Symp. Surface Mining Hydrology Sedimentology and Reclamation, Lexington, KY, 73-75.

Urosevic, M., Rodriguez-Navarro, C., Putnis, C. V., Cardell, C., Putnis, A., Ruiz-Agudo, E., 2012. In situ nanoscale observations of the dissolution of dolomite cleavage surfaces. Geochim. Cosmochim. Acta 80, 1-13.

Volume Graphics, http://www.volumegraphics.com, Heidelberg, Germany.

Watten, B.J. Lee, P.C. Sibrell, P.L. Timmons, M.B., 2007. Effect of temperature, hydraulic residence time and elevated pCO_2 on acid neutralization within a pulsed limestone bed reactor. Water Res. 41, 1207-1214.

Watten, B.J., Sibrel, P.L.l, Schwartz, M.F., 2005. Acid neutralization within limestone sand reactors receiving coal mine drainage. Environ. Pollut. 137, 295-304.

Watzlaf, G. R., Schroeder, K. T., Kleinmann, R. L. P., Kairies, C. L., Nairn, R. W., and Street, W. B., 2004. The Passive Treatment of Coal Mine Drainage. DOE/NETL-2004/ 1202.. US Department of Energy, National Energy Technology Laboratory, Pittsburgh, PA, 1-72.

Wilkins, S.J., Compton, R.G., Taylor, M.A., Viles, H.A., 2001. Channel Flow Cell Studies of the Inhibiting Action of Gypsum on the Dissolution Kinetics of Calcite: A Laboratory Approach with Implications for Field Monitoring. J. Colloid Interf. Sci. 236, 354-361.

Wolery, T.J., Jackson, K.J., Bourcier, W.L., Bruton, C.J., Viani, B.E., Knauss, K.G., Delany, J.M., 1990. Current status of the EQ3/6 software package for geochemical modeling. In: Melchior, C., Bassett, R.L. (Eds.), Chemical Model of Aqueous Systems II. ACS Symposium Series 416, 104-116.

Xu, M., Sullivan, K., Vanness, G., Knauss, K.G., Higgins, S.R., 2013. Dissolution kinetics and mechanisms at dolomite-water interfaces: effects of electrolyte specific ionic strength. Environ. Sci. Technol. 47, 110-118.

Young, R.A., 1995. The Rietveld Method. Oxford University Press, International Union of Crystallography.

Younger, P., 1997. The longevity of minewater pollution: a basis for decision-making. Sci. Total Environ. 194-195, 457-466.

Zhang, J., Nancollas, G.H., 1992. Influence of calcium/sulfate molar ratio on the growth rate of calcium sulfate dihydrate at constant supersaturation. J. Cryst. Growth 118, 287-294.